Spin-to-charge current interconversion in highly resistive sputtered bismuth selenide

Dissertation

for the purpose for obtaining the degree of Doctor
at the University of the Basque Country
by

Isabel Cristina Arango Gutiérrez

performed under the supervision of
Prof. Dr. Fèlix Casanova & Prof. Dr. Luis. E. Hueso

Universidad del País Vasco
Euskal Herriko Unibertsitatea

"Nadie debe conocer su sentido
mientras no hayan cumplido cien años"

"No one should know its meaning
until they have reached one hundred years"

Gabriel García Márquez

Abstract

The breakthrough of modern technology touches every aspect of daily life. It is increasingly transforming every aspect of society, with incredible possibilities for change that seem endless. At the heart of it all is a half-century-old law known as Moore's Law. It applies the simple concept of transistors to integrated circuits, which are electrically controllable switches but miniaturized, so that the number of transistors per silicon chip doubles every two year. The semiconductor industry now produces billions of them on a small silicon chip. However, these technological advances and developments in materials science are reaching the physical limits of size reduction, especially in terms of power consumption, because smaller transistors no longer mean lower operating voltages, compromising the energy efficiency and performance of future chips. A change in the integrated circuit is urgently needed. In this regard, the electronics industry has opened new frontiers, such as beyond complementary metal-oxide-semiconductor (CMOS) technology, which does not rely on traditional carrier transport and has shown early promise as a way to further advance Moore's Law in the future. One that deserves further consideration is spintronic devices.

Spintronic devices exploit the spin degree of freedom of electrons in applications such as non-volatile memory and logic devices. Spintronics relies on strong spin-orbit coupling (SOC) materials that allow spin-charge interconversion (SCI) via the spin Hall effect (SHE) or the Edelstein effect (EE). A recent proposal from Intel introduced a new device concept known as magneto-electric spin-orbit (MESO) for logic operations based on a device with two different nodes cascading multiple devices. The input node is used to write a magnetic element with voltage using magnetoelectric effects, and the output node is used to read the magnetic state of the element using spin-to-charge conversion. One of the requirements for MESO device is that the readout voltage should be above the coercive voltage of the magnetoelectric material (~ 100 mV) to drive the next element in a logic operation, a

value that could be achieved by using materials with high SCI efficiencies and high resistances.

In this regard, a promising candidate for the output node of the MESO device is Bi_2Se_3, which has been reported to have both high SCI efficiency and high resistivity. Bi_2Se_3 is known as a topological insulator. This class of materials exhibits spin-momentum locking in the topologically protected surface states, a property that allows an efficient EE (denoted by the inverse Edelstein length, λ_{IEE}). Exploitation of these surface states typically requires an epitaxial structure and low temperature to minimize bulk conduction.

Recently, some works have reported large SCI even at room temperature in polycrystalline Bi_xSe_{1-x} (BiSe) grown by sputtering, a simple technique compatible with industrial processes. Although the Edelstein effect is the source of SCI in ideal topological insulators, many works use the spin Hall angle (θ_{SH}) to quantify the SCI efficiency in this class of materials. In this case, just as for materials exhibiting SHE, the spin diffusion length (λ_s) is an essential parameter for a proper quantification of the SCI efficiency. Indeed, for many applications, including MESO, the relevant figure of merit is the $\theta_{SH}\ \lambda_s$ product, which is equivalent to λ_{IEE}. Nevertheless, λ_s for sputtered BiSe is usually taken from a few reports describing epitaxially grown Bi_2Se_3, which has not only a different crystal structure but also a different composition. This dissimilarity inevitably leads to inaccuracies in the subsequent quantification of the SCI efficiency of BiSe. In addition, most SCI quantification techniques require the SCI material to be in direct contact with a ferromagnetic or transition metal, but recent studies on Bi_2Se_3 have reported interdiffusion by solid-state reaction when in contact with metals. This creates a new layer at the interface through which the spins are injected or pumped, making it difficult to accurately quantify the spin properties (λ_s and θ_{SH}) of this material.

In this thesis, we characterize sputtered BiSe by several SCI techniques. Our first approach is one of the best known techniques, spin pumping. Chapter 4 presents the SCI results in sputtered BiSe by the spin pumping technique using opposite stacking orders (BiSe/Py and Py/BiSe). By studying the results on both systems, we found a strong interdiffusion, so that the chemical composition of the magnetic layers and the interfaces were not homogeneous, and therefore the models used to characterize the properties of the system were no longer valid. Ignoring these inhomogeneities in the interfaces and films would lead to an incorrect estimation of the SCI efficiency.

In Chapter 5, we used a different configuration to perform SCI measurements, with an architecture similar to the readout node of the (MESO) device, using T-shaped devices for local spin injection. Taking into account the knowledge gained in Chapter 4 (regarding interdiffusion), we fabricated local T-shaped devices and we were able to observe SCI in sputtered BiSe devices at room temperature and proved that all parameters related to SCI efficiency, namely resistivity, λ_s and θ_{SH}, are affected by interdiffusion. In particular, the fact that a change in Se concentration by interdiffusion made a 6 times difference in resistivity. We have shown here how this can easily lead to an overestimation of the spin transport parameters.

Subsequently, in Chapter 6, we fabricated lateral spin valves (LSVs) for the spin absorption technique, this time to reduce interdiffusion by growing the metals in contact with the BiSe wire by e-beam evaporation, a gentler deposition technique than sputtering. In addition, LSVs allow us to perform two separate measurement configurations. It is then possible to independently quantify λ_s and θ_{SH} of BiSe. The use of a nonlocal measurement avoids spurious effects related to local currents, such as Oersted fields in spin-orbit torque techniques or fringe-field induced voltages in three-terminal potentiometric techniques. This information allows us to model our devices and perform 3D Finite Element Method (3D FEM) analysis to extract the spin transport parameters at different temperatures. Furthermore, to take advantage of the LSV configuration, we proposed the use of a graphene-based LSV in Chapter 7, which also allows us to suppress the interdiffusion with the BiSe wire. Surprisingly, in the BiSe/graphene LSV, we observe SCI components beyond the SHE in bulk BiSe we were looking for. These new components are an interesting way to explore new possibilities in the design of novel spintronic devices.

The results in this thesis highlight the importance of considering all the details of BiSe and its interfaces to properly quantify the spin transport properties of this material, something that is unfortunately neglected in many studies. Although the existing literature has reported a high SCI efficiency for BiSe and presented this material as a promising candidate for MESO logic devices, our work shows otherwise. A more accurate characterization, based on nonlocal devices that eliminate spurious effects, reveals that the SCI efficiency of sputtered BiSe is in fact too low to be used for MESO technology.

Resumen

El rápido progreso de las tecnologías afecta a todos las áreas y aspectos de la vida cotidiana. Esta, está transformando cada vez más todos los aspectos de la sociedad, con increíbles posibilidades de cambio que parecen no tener fin. En el centro de todo ello se encuentra una ley de hace medio siglo de antigüedad conocida como la Ley de Moore. Esta aplica el sencillo concepto de los transistores y los circuitos integrados, que son interruptores controlables eléctricamente, pero miniaturizados, de modo que el número de transistores por chip se duplica cada dos años. La industria de semiconductores hoy en día produce miles de millones de ellos en un pequeño chip de silicio. Sin embargo, estos avances tecnológicos y la evolución de la ciencia de los materiales están llegando a los límites físicos de la reducción de tamaño, especialmente en términos de consumo de energía. Fabricar transistores más pequeños no significa voltajes de funcionamiento más bajos, esto compromete la eficiencia energética y el rendimiento de los futuros chips, lo que hace surgir una gran necesidad de un cambio en el diseño y fabricación de los dispositivos integrados. En este sentido, la industria electrónica ha abierto nuevas fronteras más allá de la tecnología CMOS (del inglés *complementary metal-oxide-semiconductor*), las cuáles no depende del transporte tradicional de portadores de carga y que se han mostrado prometedoras como forma de seguir avanzando en la Ley de Moore en el futuro. Los dispositivos espintrónicos son uno de ellos.

Los dispositivos espintrónicos explotan el grado de libertad de espín de los electrones en aplicaciones como dispositivos de lógica y de memoria no volátil. La espintrónica se basa en materiales con un fuerte acoplamiento espín-órbita (SOC, del inglés *spin-orbit coupling*) que permiten la interconversión espín-carga (SCI, del inglés *spin-charge interconversion*) mediante el efecto Hall de espín (SHE, del inglés *spin Hall effect*) o el efecto Edelstein (EE). Una reciente propuesta de Intel introdujo un nuevo concepto de dispositivo conocido como MESO (del inglés *magneto-electric spin-orbit*) para operaciones lógicas basadas en un dispositivo con dos nodos diferentes conectados en cascada a múltiples dispositivos. El nodo

de entrada se utiliza para escribir un elemento ferromagnético con un voltaje utilizando efectos magnetoeléctricos. En cuanto al nodo de salida, se utiliza para leer el estado magnético del elemento ferromagnético, utilizando la conversión espín-carga. Un importante requisito para el funcionamiento de los dispositivos MESO es el voltaje de lectura que debe estar por encima del voltaje coercitivo del material magnetoeléctrico (~ 100 mV) y así poder conducir el siguiente elemento en una operación lógica. Un valor que podría conseguirse utilizando materiales con altas eficiencias SCI y altas resistividades.

Por lo que un candidato prometedor para el nodo de salida (lectura) del dispositivo MESO es el Bi_2Se_3, del que se ha reportado que tiene una alta eficiencia SCI y una alta resistividad. El Bi_2Se_3 se conoce como un material aislante topológico. Esta clase de materiales exhibe bloqueo de momento de espín en los estados superficiales topológicamente protegidos, una propiedad que permite un EE muy eficiente (denotado por la longitud Edelstein inversa, λ_{IEE}). Sin embargo la explotación de estos estados superficiales suele requerir una estructura epitaxial y bajas temperaturas para minimizar la conducción del bloque o interior del material.

No obstante, recientemente algunos estudios han reportado altas eficiencias de SCI incluso a temperatura ambiente en Bi_xSe_{1-x} (BiSe) policristalino y crecido por *sputtering*, una técnica que es sencilla y compatible con los procesos industriales. A pesar de que el EE es la fuente de SCI en aislantes topológicos ideales, muchos trabajos utilizan el ángulo Hall de espín (θ_{SH}) para cuantificar la eficiencia de SCI en esta clase de materiales. En este caso, al igual que para los materiales que presentan SHE, la longitud de difusión del espín (λ_s) es un parámetro esencial para una cuantificación adecuada de la eficiencia de SCI. De hecho, para muchas aplicaciones incluyendo el dispositivo MESO, la figura de mérito relevante es el producto $\theta_{SH}\ \lambda_s$, que es el equivalente a λ_{IEE}. Sin embargo, el valor λ_s para el BiSe depositado por *sputtering* suele tomarse de unos pocos estudios que reportan el Bi_2Se_3 crecido epitaxialmente, que no sólo tiene una estructura cristalina diferente sino también una composición química distinta. Esta diferencia conduce inevitablemente a imprecisiones para la posterior cuantificación de la eficacia del SCI del BiSe. Por otra parte, la mayoría de las técnicas de cuantificación del SCI requieren que el material donde ocurre la conversión de espín-carga esté en contacto directo con otro material ferromagnético o metal de transición. Aunque estudios recientes sobre Bi_2Se_3 han reportado que este sufre interdifusión por reacción en estado sólido al entrar en contacto con metales. Esto crea una nueva capa en la interfaz a través de la cual se inyectan o bombean los espines, lo que dificulta la

cuantificación precisa de las propiedades de transporte de espín (λ_s y θ_{SH}) de este material.

En esta tesis, caracterizamos el BiSe depositado por el proceso de *sputtering* mediante diferentes técnicas de SCI. Nuestro primer acercamiento lo realizamos con una de las técnicas más conocidas en este campo, que es el *spin pumping*. El Capítulo 4 presenta los resultados de SCI en BiSe depositado por *sputtering* mediante la técnica de *spin pumping* utilizando órdenes de apilamiento opuestos (BiSe/Py y Py/BiSe). Al estudiar los resultados en ambos sistemas encontramos una fuerte interdifusión, donde la composición química de las capas magnéticas y las interfaces no eran homogéneas, por tanto los modelos utilizados para caracterizar las propiedades del sistema dejaban de ser válidos. Ignorar estas inhomogeneidades en las interfaces y las películas conduciría a una estimación incorrecta de la eficiencia de la SCI.

En el Capítulo 5, utilizamos una configuración diferente para realizar medidas de SCI, con una arquitectura similar al nodo de lectura del dispositivo MESO, haciendo uso de dispositivos con formas en T para la inyección local de espín. Teniendo en cuenta los resultados del Capítulo 4 sobre la interdifusión, fabricamos los dispositivos locales en forma de T y pudimos observar SCI en dispositivos de BiSe depositados por *sputtering* a temperatura ambiente y demostramos que todos los parámetros relacionados con la eficiencia de SCI, como la resistividad, λ_s y θ_{SH}, se ven afectados por la interdifusión. En particular, el hecho de cambiar la concentración de Se por la interdifusión genera una diferencia de hasta 6 veces en el valor de la resistividad de este material. En este capítulo hemos demostrado cómo esto puede conducir fácilmente a una sobreestimación de los parámetros de transporte de espín.

Posteriormente, en el Capítulo 6, fabricamos válvulas laterales de espín (LSV, del inglés *lateral spin valves*) para usar la técnica de absorción de espín. Esta vez para reducir la interdifusión entre los metales en contacto con el electrodo de BiSe, los metales los hemos depositado por evaporación de haz de electrones, una técnica de deposición más suave que el *sputtering*. También, las LSV nos permiten realizar dos configuraciones de medida separadas, posibilitando cuantificar independientemente λ_s y θ_{SH} del BiSe. Por otro lado, el uso de una medición no local evita los efectos espurios o no deseados relacionados con las corrientes locales, como los campos de Oersted en las técnicas de *spin-orbit torque* o los voltajes inducidos por las líneas de campo en las técnicas potenciométricas de tres terminales. Con los resultados obtenidos en ambas configuraciones podemos modelar nuestros dispositivos en 3D y analizarlos por el método de los elementos finitos (3D FEM) para

extraer los parámetros de transporte de espín a diferentes temperaturas. Además, para aprovechar las ventajas de la configuración de las LSV, en el Capítulo 7 propusimos el uso de una LSV basada en grafeno como canal de difusión de espín, que además nos permite suprimir la interdifusión con el electrodo de BiSe. Sorprendentemente, en la LSV de BiSe/grafeno, observamos otros componentes de SCI más allá del SHE en el BiSe, el cual estábamos buscando. Estos nuevos componentes son una forma interesante de explorar nuevas posibilidades en el diseño de dispositivos espintrónicos novedosos.

Con base en los resultados obtenidos en esta tesis, destacamos la importancia de considerar todos los detalles del BiSe y sus interfaces para cuantificar adecuadamente las propiedades de transporte de espín de este material. Algo que lastimosamente se descuida en muchos estudios. Aunque la literatura existente ha reportado una alta eficiencia SCI para BiSe y ha presentado este material como un candidato prometedor para dispositivos lógicos MESO, nuestro trabajo demuestra lo contrario. Con una caracterización más precisa, basada en dispositivos no locales que eliminan los efectos espurios, revelamos que la eficiencia SCI del BiSe depositado por *sputtering* es de hecho baja para ser utilizada en la tecnología MESO.

Spin-to-charge current interconversion in highly resistive sputtered bismuth selenide

Chapter 1

Spintronics for a world beyond CMOS

1.1 Beyond-CMOS Devices

Moore's Law [1], which states that the number of components per integrated circuit doubles every two years (Fig. 1.1), has been the guiding principle of the semiconductor industry for decades. Its influence and impact on society as a whole has been astounding, resulting in a steady increase in the performance, affordability, and availability of integrated circuits.

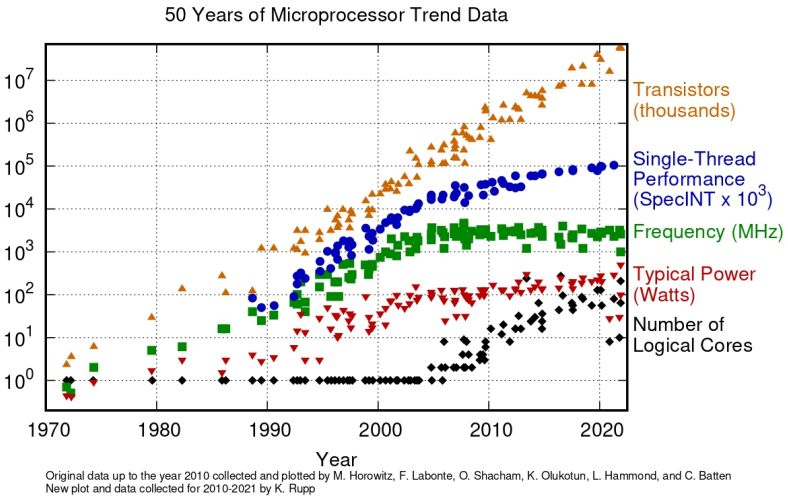

Figure 1.1: Moore's Law. Microprocessor trend data versus introduction dates. Transistors are nearly doubling every two years, following Moore's Law (orange triangle). However, operating frequency (green squares) and typical power (red triangle) reached their limits around 2005. To compensate, a larger number of cores were introduced (black rhombus) to have more parallel operations or logical operations per second, with processing performance increasing slightly after this year (blue circles). Figure taken from Ref. [2].

Increasing computing performance, improving energy efficiency, and shrinking the size of integrated circuits have allowed more industries to develop and new ones to emerge. Although there have been concerns about the future of Moore's Law since its inception, the challenges have changed over time. However, while Moore's Law is still supported by increasingly complex transistor designs and advances in lithography, the last decade has seen a clear breakdown of Dennard's scaling [3], where smaller transistors no longer mean smaller operating voltages, compromising the energy efficiency and performance of future chips (red triangles and blue circles in Fig. 1.1, respectively). To that end, the electronics industry

continues to drive progress on many fronts, such as new devices beyond complementary metal-oxide-semiconductor (CMOS) technology that do not rely on traditional carrier transport, which have shown early promise as a way to further advance Moore's Law in the future [4, 5]. One that deserves further consideration is spintronic devices.

In addition to continued advances in CMOS technology [6–8], new alternatives to iterative logic circuits beyond the CMOS transistor have emerged in recent years, such as the ones shown in Fig.1.2. These logic devices explore new physical effects through novel or unconventional materials using alternative state variables such as magnetization, polarization, and strain. Among these options, spin-based solutions have shown tremendous promise and applicability through the field of spintronics [9]. For example, devices with spin-transfer torque (STT) and spin-orbit torque (SOT) effects exploit the non-volatile nature of their magnetic elements [10] and have current-controlled magnetic switching by spin torque (which is the effect of spin-polarized electrons changing magnetization). Such devices brought some improvements in write speeds and are compatible with manufacturing processes when used as memories, but the energy required for logic operations is still too high to make them competitive, see Fig. 1.2a. [5, 11].

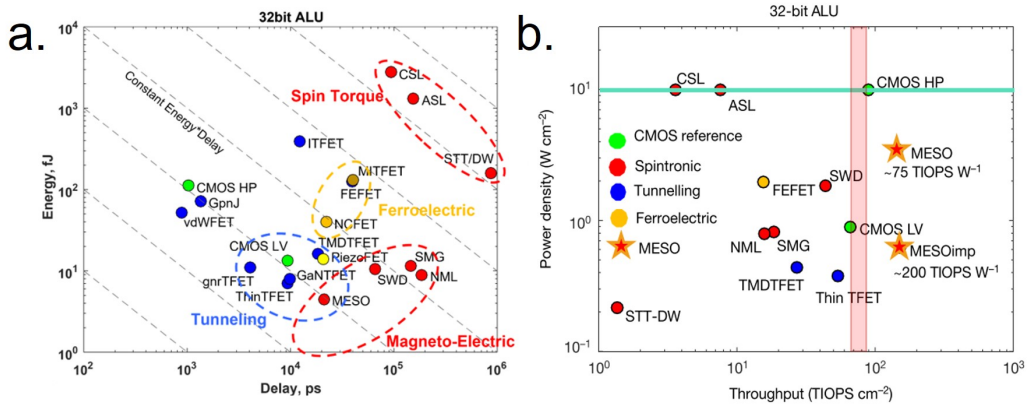

Figure 1.2: CMOS and beyond CMOS. a. The energy consumption versus the delay time (courtesy of Ian A. Young), and **b.** the power per unit area versus throughput (the number of 32-bit ALU operations per unit time and unit area, in units of tera-integer operations per second (TIOPS)) for CMOS and beyond-CMOS devices. Figure taken from Ref. [12]. STT-DW, spin-transfer-torque domain-wall device; ASL, all-spin-logic device; CSL, charge spin logic; NML, nanomagnetic logic; SMG, spin majority gate; SWD, spin wave device; CMOS HP, high-performance CMOS at 0.73 V supply; CMOS LV, low-power CMOS operating at 0.3 V supply; FEFET, ferroelectric FET; Thin TFET, 2D-material vertical tunnel FET; TMDTFET, transition-metal dichalcogenide tunnel FET; MESO, magneto-electric spin-orbit.

On the other hand, if the switching of the magnetic element is voltage-based using magneto-electric (ME) effects, the energy consumption is lower (Fig. 1.2). Voltage-based collective switching is thus one of the leading solutions for computational advances due to the potential for ultralow switching energy and switching voltage [12].

Compared to the leading beyond CMOS and highly advanced CMOS technologies, these spintronic devices show significant gains in areal logic density, operating energy, and computational throughput. Figure 1.2 shows a benchmark of the energy vs the delay diagram (Fig. 1.2a) and the power density (area per function) vs the throughput (Fig. 1.2b) of the new technologies beyond CMOS transistor and the advanced CMOS devices for a 32-bit arithmetic logic unit (ALU).

1.2 Spintronics from the very first application

Spintronics is a field that exploits not only the charge of the electrons, but also their spin degree of freedom [9]. Spin is the intrinsic angular momentum of electrons, a quantum property of elementary particles that has an associated magnetic moment. For an electron, the component of the angular momentum along a given axis can take two values; $\hbar/2$ or -$\hbar/2$, which are known as the "spin-up" and "spin-down" states, where $\hbar$ is the reduced Planck constant [13]. This intrinsic angular momentum can be used to carry information, much like the charge in electronics. In the late 1980s, the study of the injection, transport, manipulation, and detection of the spin degree of freedom of electrons emerged from the reports on giant magnetoresistance (GMR) [14, 15]. Magnetoresistance is defined as a change in the electrical resistance in the presence of an external magnetic field.

The GMR devices, also known as vertical spin valves, consist of a metallic multilayer system with two ferromagnetic (FM) layers separated by a non-magnetic (NM) layer with a thickness in the order of nanometers. Due to the exchange interaction in a FM material, a majority of the electrons have spin in a particular direction, giving rise to a net magnetization. The magnetization direction of the two FM layers can be either parallel to each other (configuration in Fig. 1.3a) or antiparallel (see Fig. 1.3b). According to the two-channel model (explained in Chapter 2), the resistance for an electron flowing through the multilayer device depends on the relative orientation of the electron spin and the magnetization of the FM (parallel or antiparallel), resulting in low or high resistance states [16].

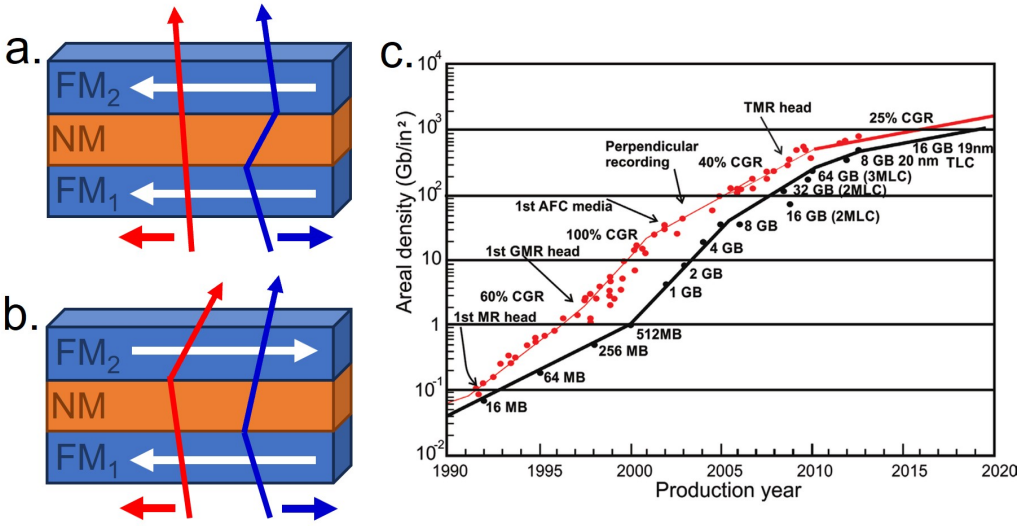

Figure 1.3: GMR: Vertical spin valve structures and the impact of their introduction in the market. Schematic illustration of a trilayer system with two FM layers (in the sketch in blue) on both sides separated by a NM layer (in orange). The two currents with opposite spin orientation are indicated by red and blue arrows. The spin-dependent scattering in the FMs gives rise to two different resistance states, **a.** a low resistance state (parallel configuration) and **b.** a high resistance state (antiparallel configuration), allowing for readout of the magnetic configuration. **c.** Trend of the increase in areal density of hard disk drives (black) and flash disks (red) over the production year. Figure adapted from Ref. [17].

GMR was rapidly and successfully transferred to applications such as magnetic field sensors and read heads for hard disk drives (see Fig. 1.3c) leading to the Nobel Prize in Physics for A. Fert and P. Grünberg in 2007 [16]. The development of spintronics started with GMR, allowing great continuous progress by increasing the areal density (number of bits per unit area) in hard drives and pushing the research for more spin-based device alternatives [18, 19].

An improved version of the spin valve is the magnetic tunnel junction (MTJ). In these junctions, the NM layer is replaced by a nanometer-thick oxide layer, resulting in a FM1/oxide/FM2 heterostructure [20–22]. This device demonstrates tunneling magnetoresistance (TMR) in which the bias applied must reach a certain energy for the electrons to tunnel from FM1 through the oxide and reach FM2. The MTJ relies on the relative orientation of the magnetization direction, like the spin valves based on GMR, but usually has a much higher magnetoresistance ratio, easily reaching more than 500% [23].

This discovery was also transferred to applications such as the magnetoresistive random access memory (MRAM). A MRAM is composed of MTJ arrays, where each MTJ represents a non-volatile memory bit, with the parallel and antiparallel states of a MTJ, i.e. the two possible resistance states, corresponding to binary values of 0 and 1. Each MTJ contains a free FM layer with switchable magnetization and another FM layer with pinned magnetization via exchange bias with an antiferromagnet.

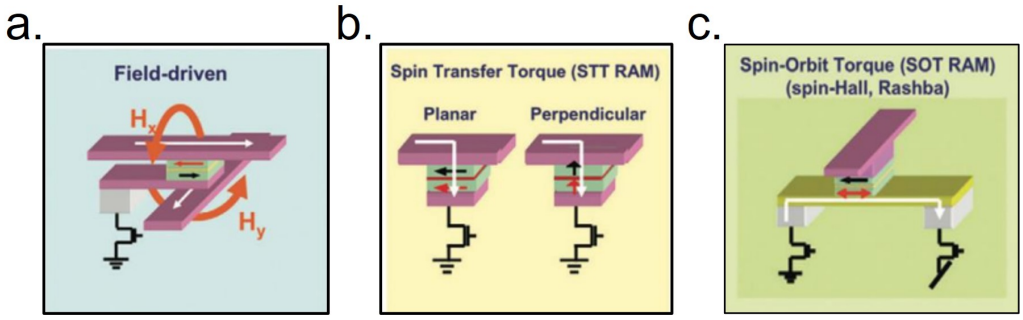

Figure 1.4: Different MRAM generations for writing magnetic states. The writing techniques based on MTJs can be achieved by the three following methods; **a.** Field-driven writing of magnetic states by inducing Oersted fields (H_y and H_x) with two bias currents (white arrows). **b.** STT relies on a torque on FM2 exerted by the spin-polarized high-density current created by a bias current across FM1; **c.** In the SOT writing device, a spin-orbit coupling material (SOM) electrode is connected to FM2 in the MTJ. A bias current through the SOM causes charge-to-spin conversion producing a transverse pure spin current that exerts a torque on FM2 (free layer, red arrow) switching its magnetization. In all methods, the magnetic state in FM2 can be switched by reversing the current direction. Figure adapted from Ref. [24].

Figure 1.4 shows several generations of MRAM based on MTJs. In all cases, the magnetic bits are read by measuring the resistance of the MTJ after a relatively small charge current is passed through the stack. However, the remaining challenge is how to write the magnetic bits, i.e. how to switch the magnetization of the free layer in an efficient way. The first approach was to use the Oersted field created by charge currents, see Fig. 1.4a. The main drawback of this technique is the barrier to downscaling, given the difficulty of localizing the magnetic field generated and the need for larger currents to switch the magnetization as the bit size is reduced [25]. STT is an alternative method of writing. This phenomenon, predicted by Slonczewski [26] and Berger [27] in 1996 results in a torque exerted on the magnetization of a FM element when a spin-polarized current is injected. If the torque is large enough, it can lead to magnetization switching. In the case of the MTJ in an MRAM, when a

charge current is applied through the MTJ, as shown in Fig. 1.4b, the first FM layer of the MTJ acts as a spin polarizer. This spin-polarized current will tunnel through the insulating layer, transferring the angular momentum to the second FM layer of the MTJ and generating a torque that will switch the magnetization. It is a local technique that offers better scalability with lower power consumption and is already used in commercial STT-MRAMs [28]. The main drawback is that the relatively large charge current in the small area of the junction is detrimental to the MTJ, because high temperatures can be reached, leading to the loss of the antiferromagnetic exchange bias [24] and limiting the durability of the tunnel barrier.

There is a novel approach, known as SOT, to electrically write magnetic memory elements by employing a material with strong spin-orbit coupling (SOM). In this case, a charge current flows through a SOM metal adjacent to the free layer of the MTJ, see Fig. 1.4c. This charge current generates a transverse spin current, which exerts a torque able to switch the magnetization of the free layer. Since, in SOT-based MRAM, charge currents for writing do not flow through the MTJ, the device shows major durability. However, current densities needed for switching are still higher than in STT-MRAM, and the search for materials that more efficiently convert charge currents into spin currents is one of the major objectives in this technology [29].

1.3 Magneto-electric spin-orbit logic

Logic operations are used to compute information in integrated circuits in CMOS and beyond CMOS devices. As mentioned above, several proposals have been developed to improve the efficiency and power consumption of CMOS by using spin-based devices as shown in Fig.1.2. However, they are not efficient enough because the magnetic state writing process is current-induced (STT or SOT). In this regard, Intel has recently proposed an alternative for logic operations called magneto-electric spin-orbit (magneto-electric spin-orbit (MESO)) device, which integrates memory elements and logic operations within the same circuit [12].

The MESO device has two main nodes. The input node is used to write a magnetic element with voltage using ME effects (Fig. 1.5a, back). The use of voltage-based switching overcomes the problems of current-based switching devices for logic operations, due to the potential for ultralow switching energy. The MESO device incorporates ferroic order parameters with collective switching of ferromag-

netism and ferroelectricity or ferroelasticity. Logic based on collective state switching devices are a leading option for computational advances beyond the modern CMOS era owing to their potential for lower energy per operation, higher computational logical density and efficiency owing to the use of majority gates, non-volatile memory-in-logic and logic-in-memory capability and amenability to traditional and emerging architectures (i.e, neuromorphic and stochastic computing)[12].

The polarization/magnetization reversal in ME/FM heterostructures is very energy efficient and should therefore enable the attojoule level switching energy desired for global energy saving. This will be possible for a given energy barrier set for the technology requirements. The energy barrier is related to the device retention time and determines the non-volatile nature of the switch, corresponding to the energy dissipated in switching and the required stability of the logic state.

The magnetization in FMs is an order parameter controlled by spin current or voltage. The ME material is the actuator for controlling this magnetization direction of the FM layer, which can be ferroelectric with polarization as the voltage-defined order parameter or ferroelastic with strain as the strain- or voltage-controlled order parameter [30]. A promising candidate for writing is the multiferroic $BiFeO_3$ combined with ferromagnetic CoFe [31]. In the MESO device, opposite input voltages produce a change in polarization or strain in the ME layer, which induces exchange bias and coupling, and subsequently a reversal of magnetization in the FM [32, 33].

The second node of the MESO device is the output node or spin-orbit (SO) node for reading the magnetic state (Fig. 1.5a, front). The magnetic state is read out by applying a bias current through the FM so that a spin-polarized current is injected into a SOM. The spin-charge interconversion (SCI) in the SOM layer will convert the spin current into a transverse charge current and create a potential difference between the two ends of the SOM layer [34]. The output current (and voltage) will be opposite depending on whether the magnetic state is "1" or "0" as shown in Figs. 1.5b and 1.5c.

The two possible in-plane ferromagnetic states along the easy axis of the FM can be associated with these logic bits "1" and "0". Several MESO devices must be connected by a NM electrode to create cascaded gates with inverter operations. In such a cascaded gate, the SO node is connected to the next ME node so that the output of the SO node is the input of the ME node, in accordance with the MESO proposal. In this sense, to achieve stability, energy efficiency, and fast switching of the next FM layer, the required SO node output signals for operating the MESO device is 100 mV [12]. The operation is spin-based, but the information transport is charge-

based, with this operation voltage, the switching energy could be as low as 1 aJ per bit [12].

In this thesis, we focus on studying a SOM with high SCI efficiency to be placed in the SO node. Figure 1.5d shows the projected improvement in the spin-orbit readout, suggesting the use of materials with very low conductivity and large spin-orbit effects, such as topological insulator (TI) materials [11, 35–38]. The spin Hall angle, θ_{SH}, of TI is considered to have an exceptionally large value in agreement with spin-orbit torque results [36, 39–42] and a long inverse Rashba-Edelstein length, λ_{IREE}[43], and has high resistivity as bulk conduction is limited [44, 45], which satisfies the required conditions for MESO. One promising candidate for the SO node is Bi_2Se_3.

Bi_2Se_3 has attracted much attention due to their unique properties. In particular, the spin-momentum locking in the topologically protected surface states makes it desirable for SCI in spintronic devices [46, 47]. Although these topological properties are thought to be related to epitaxial growth to keep a single crystal structure [48], some works report large SCI in sputtered polycrystalline Bi_xSe_{1-x} (BiSe) [49–53]. According to Mahendra DC *et al.* [49], the granular structure of the sputtered BiSe layers exhibits quantum confinement and thus high efficiency, although quantum phenomena are difficult to demonstrate at room temperature [54].

Since BiSe is a promising candidate, we worked in close collaboration with Intel on the study and characterization of magnetic state readout using this material as SOM for the SO node of the MESO device, during the time of this Ph.D. project.

The SCI efficiency of BiSe has been estimated using various techniques, such as spin pumping [50, 51], DC planar Hall [49], spin-torque ferromagnetic resonance [49], SOT current-induced magnetic switching [49, 52], and harmonic Hall measurements [49, 53]. However, all of these approaches require the BiSe to be in contact with a FM, and it is extremely difficult to obtain clean interfaces in a BiSe/FM stack. When a metallic layer is grown on top/bottom of BiSe, a large intermixing at the interface between these materials is a common phenomenon [55, 56]. In addition, although there are several techniques to quantify SCI, to date reported values for sputtered BiSe have often been overestimated due to spurious effects related to local currents combined with a lack of understanding of the effect of the interfaces and the use of approximations for unknown parameters, such as the spin diffusion length (λ_s). The value of λ_s for sputtered BiSe is usually taken from few reports describing epitaxially grown Bi_2Se_3 [57–59], which not only has a different crystal

structure, but also a different composition. This dissimilarity invariably leads to inaccuracies in the subsequent quantification of the SCI efficiency of BiSe.

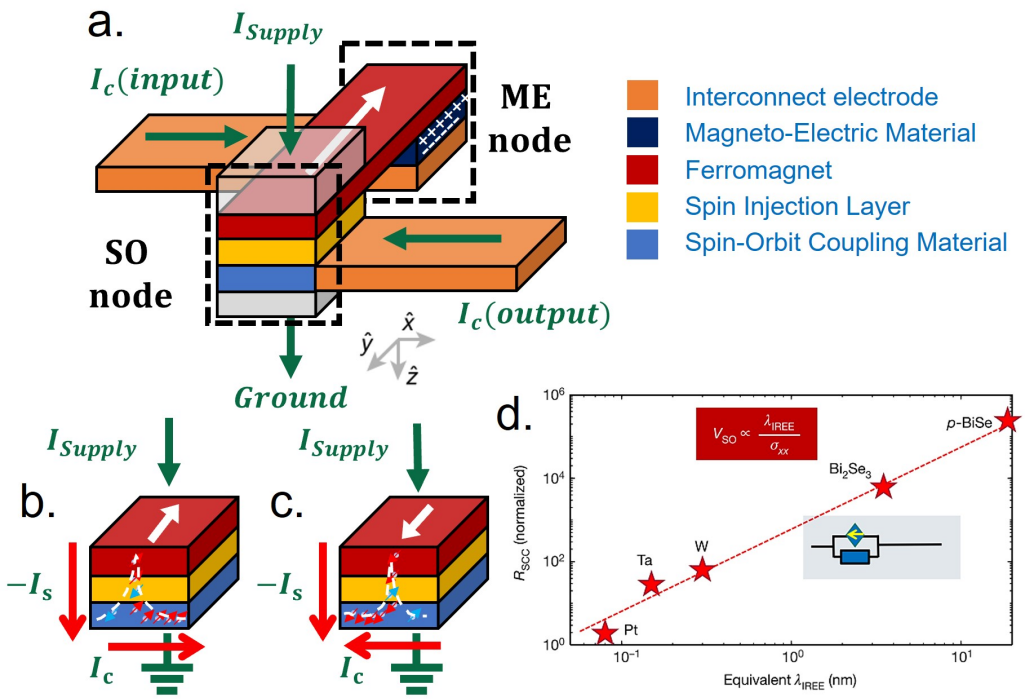

Figure 1.5: **MESO logic device operation. a.** Device formed with a FM element, a magnetoelectric (ME) node and a spin-orbit (SO) node. The ME node consists of an interconnect channel with a NM metal (orange), a ME capacitor (dark blue), and a FM layer on top (red). The SO node consists of a spin-injection layer (yellow) for spin injection from the FM (red) to the SOM (light blue), and contacts to the power supply and ground (grey layers). A current and voltage applied to the ME node will switch the FM magnetization (white arrow) exploiting the coupling between the ME and the FM layers. The magnetization can be read out by supplying a charge current (I_{supply}), that will inject a spin-polarized current (I_{s}) into the SOM layer. An output charge current I_{c} and a voltage potential difference V_{SO} is generated via the SCI. The green arrows show the directions of the input and output currents of the device. **b.** Operating mechanism for spin-to-charge conversion using a SOM. A spin injection layer is used if needed by the material interfaces. Spins injected from the FM in the $+z$ direction with spin polarization along the $-y$ (in-plane) direction cause a transverse charge current in the SOM layer. Small red and blue arrows indicate up and down spins, respectively, injected from the magnet. The large red arrows show the directions of the charge (I_c) and injected spin (I_s) currents. **c.** Operation mechanism in the SO node when reversing the magnetization direction, white arrow in the FM pointing in the $+y$ direction. **d.** SOM candidates to be placed in the SO node. V_{SO} and σ_{xx} are the generated voltage and conductivity. Figure adapted from Ref. [12].

1.4 This thesis

The aim of this thesis is to accurately quantify the spin transport properties of sputtered polycrystalline and highly resistive BiSe. Although there are some reports on the high SCI efficiency of BiSe, there are also some discrepancies related to spurious effects, approximations for unknown parameters, or lack of understanding of the key role of interfaces. Our goal is to study and unveil the BiSe properties with the motivation of placing it in the readout node of the MESO logic device.

This way, we present in **Chapter 1** (*Spintronic for a world beyond-CMOS*) an overview of CMOS technology and integrated circuits, as well as the developments made possible by advances in the field of spintronics. One of these developments is Intel's proposal for logic computing using MESO technology, which requires the use of a material exhibiting both high resistance and large spin-orbit effects.

Chapter 2 (*Theory of Spin*) provides the theoretical background of spin physics, such as spin injection, accumulation, transport, and detection, as well as some possibilities to create and control spin currents using SCI. We also present the devices used in this thesis to measure and quantify SCI.

Chapter 3 (*Experimental Techniques*) gives details about the techniques used for the fabrication, characterization, and analysis of the spintronic devices used in this thesis.

The following four chapters present different approaches to study and properly characterize sputtered polycrystalline BiSe. **Chapter 4** (*Spin-to-charge conversion by spin pumping in sputtered polycrystalline Bi_xSe_{1-x}*) presents SCI measurements by spin pumping experiments, while in **Chapter 5** (*All-electrical spin-to-charge conversion in sputtered Bi_xSe_{1-x}*) a local device using a similar readout configuration of the MESO device is shown. These two chapters demonstrate the challenges caused by the interdiffusion of BiSe in contact with metallic layers.

Chapter 6 (*Quantification of spin-charge interconversion in highly resistive sputtered Bi_xSe_{1-x} with nonlocal spin valves*) presents the results of SCI using metallic lateral spin valves with a cleaner interface between BiSe and the contact metal. **Chapter 7** (*Charge-to-spin conversion in sputtered Bi_xSe_{1-x}/graphene heterostructure by nonlocal spin injection*) gives an alternative approach to suppress the interdiffusion using lateral spin valves with graphene as spin transport channel. In-

terestingly, we observe an unconventional SCI component that could provide additional flexibility to the design of the next generation of spin-based devices.

Chapter 8 (*Conclusions and Outlook*) summarizes the work and highlights the importance of interfaces in spintronic devices. Furthermore, since one of the major obstacles in realizing spintronic devices such as MESO logic devices is the large signal needed for magnetization readout, we propose some materials with high SCI efficiency such as TI materials based on Bi that could improve such readout.

Chapter 2

Theory of spin

2 2.1 Spin transport

The spin degree of freedom of electrons is a convenient way to transport information from and into a magnetic element [60], i.e. to write and/or read a magnetic state which can be exploited in memories and logic devices as mentioned in Chapter 1. For this purpose, it is necessary to understand how we can generate, transport and detect spin currents. In this chapter, we describe the physics of spin currents in FM and NM materials, including the spin relaxation mechanisms that limit the transport of pure spin currents. Finally, we describe how we can use such spin currents for applications.

2.1.1 Charge and spin currents

An electron carries both charge and spin. The flow of an electron's charge in the presence of an electric field $\boldsymbol{E}$ is what we usually call a charge current (Fig. 2.1a), the well-known type of current used in the field of electronics. However, we can also create a spin current, which is a net flow of spin angular momentum and can be exploited, giving rise to the field of spintronics.

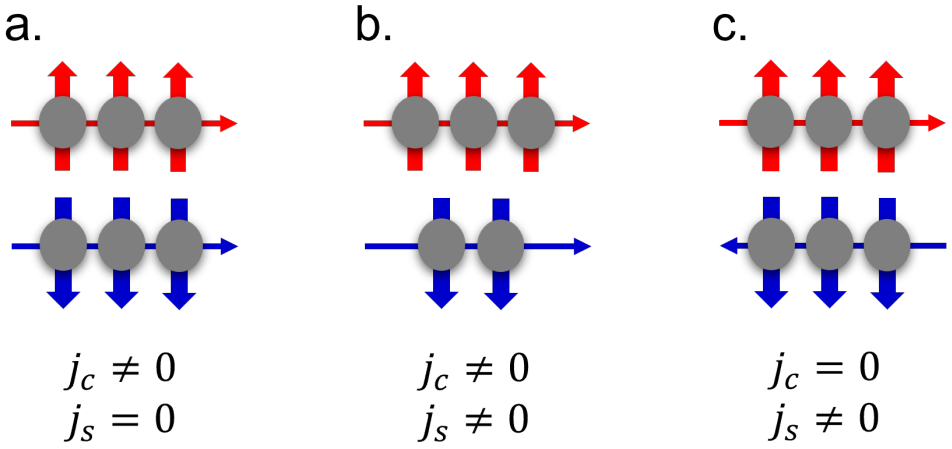

Figure 2.1: Schematic representation of currents. a. Charge current in which the same number of electrons with spins up (red arrows) and spins down (blue arrows) move in the same direction. **b.** Spin-polarized current has an imbalance of up and down spins moving in the same direction, creating a net flow of charge and also spin angular momentum. **c.** In a pure spin current, electrons with opposite spins move in opposite directions. As a result, the charge current is canceled while a net spin current remains.

For example, FM materials have non-zero magnetization even in the absence of a magnetic field. This is due to an intrinsic exchange interaction E_{ex}, which energetically favors the parallel alignment of one type of spin carrier and induces a shift in the 3d-subband energy. The 3d-subband in FMs is not completely filled, so that the shift E_{ex} creates an imbalance in the density of states (DOS) of the spin-up and spin-down 3d electrons at the Fermi level [$N_{\uparrow}(E_{\text{F}}) \neq N_{\downarrow}(E_{\text{F}})$], creating majority and minority spin carriers. This imbalance means that the spin-down s-electrons have a different scattering rate (with the associated 3d-electrons) and mobility than the spin-up s-electrons, resulting in a different conductivity for the two types of spin carriers [61].

This concept justifies the use of the two-channel model introduced by Mott [62], where the spin-up and spin-down electrons are considered to flow in two independent transport channels with no interaction between the different spin carriers. The validity of this model was experimentally verified by Fert and Campbell when studying the change of conductivity in FM metals such as Fe, Ni, Co and their alloys [63]. The electrical conductivities for spin-up and spin-down electrons as given by the two-channel model are:

$$\sigma_{\uparrow} = \frac{N_{\uparrow}(E_{\text{F}})e^2\tau_{\uparrow}}{3m_e} \quad \text{and} \quad \sigma_{\downarrow} = \frac{N_{\downarrow}(E_{\text{F}})e^2\tau_{\downarrow}}{3m_e}. \tag{2.1}$$

where e is the elementary charge, m_e is the electron mass, and $N_{\uparrow(\downarrow)}(E_{\text{F}})$ is the electron DOS at the Fermi level for each spin subband. The electron momentum scattering time for each spin type $\tau_{\uparrow(\downarrow)}$ is proportional to the electron mean free path, which is the average distance an electron travels between two scattering events, $l_{\uparrow(\downarrow)} = \tau_{\uparrow(\downarrow)}v_{\text{F}}$, where v_{F} is the Fermi velocity.

The two independent spin channels can be considered as two parallel resistors with a total electrical conductivity $\sigma = \sigma_{\uparrow} + \sigma_{\downarrow}$. Then, when applying a charge current in the FM material, it becomes spin-polarized due to the difference in conductivity for the two spin electrons, defined by the spin polarization of the ferromagnet:

$$P_{FM} = \frac{\sigma_{\uparrow} - \sigma_{\downarrow}}{\sigma_{\uparrow} + \sigma_{\downarrow}}, \tag{2.2}$$

2

such that $\sigma_\uparrow = \sigma(1 + P_{FM})/2$ and $\sigma_\downarrow = \sigma(1 - P_{FM})/2$. In the particular case of a NM, $P_{NM} = 0$ and $\sigma_\uparrow/2 = \sigma_\downarrow/2 = \sigma$.

The spin carrier flow per unit time and area through the two associated spin transport channels, given a constant $\boldsymbol{E}$, is given by the current density:

$$\boldsymbol{j}_\uparrow = \sigma_\uparrow \boldsymbol{E} \quad \text{and} \quad \boldsymbol{j}_\downarrow = \sigma_\downarrow \boldsymbol{E}. \tag{2.3}$$

The total charge current density ($\boldsymbol{j_c}$) and spin current density ($\boldsymbol{j_s}$) are, respectively, given by

$$\boldsymbol{j_c} = \boldsymbol{j}_\uparrow + \boldsymbol{j}_\downarrow, \tag{2.4}$$

$$\boldsymbol{j_s} = \boldsymbol{j}_\uparrow - \boldsymbol{j}_\downarrow. \tag{2.5}$$

Figure 2.1a shows that the electron transport of an equal spin-up and spin-down population ($\boldsymbol{j}_\uparrow = \boldsymbol{j}_\downarrow$), results in a net charge current ($\boldsymbol{j_c} \neq 0$) and no spin current ($\boldsymbol{j_s} = 0$). This is typically the case in a NM. Figure 2.1b displays a difference between spin-up and spin-down currents ($\boldsymbol{j}_\uparrow \neq \boldsymbol{j}_\downarrow$) that consequently leads to both a net charge current ($\boldsymbol{j_c} \neq 0$) and spin current ($\boldsymbol{j_s} \neq 0$). Such spin-polarized current is observed in FMs. Finally, it is possible to have a pure spin current, that is, opposite flow of spin-up and spin-down currents with no overall charge current ($\boldsymbol{j}_\uparrow = -\boldsymbol{j}_\downarrow$), as shown in Fig. 2.1c. The pure spin current is one of the most appreciated ingredients of spintronics, as it permits reduced heat dissipation.

2.1.2 Electrical spin injection, accumulation and diffusion

Figure 2.2 shows an electron flow through a simple transparent FM/NM interface to illustrate the concepts of electrical spin injection, spin accumulation, and spin diffusion. By applying a bias current (I_c) from the FM to the NM metal, an unbalanced spin population is created at the FM/NM interface due to the mismatch in the DOS at the Fermi level of the FM and the NM for spins up and spins down. As a consequence, the spin population of the s-subband in the NM material is shifted near the interface. This shift is explained in terms of the electrochemical potential.

The electrochemical potential, μ, is the combination of the chemical potential, μ_{ch}, and the electric potential energy. μ_{ch} is defined as the energy required to add one

electron to the system. If the system has an excess of electrons, with small deviations from equilibrium, μ_{ch} is equal to the excess electron density, n, divided by the DOS at the Fermi energy ($N(E_F)$). The electric potential energy is given by eV, where e is the charge of the electron and V is the electric potential felt by the electron. The two definitions lead to $\mu = n/N(E_F) - eV$. As μ changes in space, electrons tend to move to the region with the lowest value.

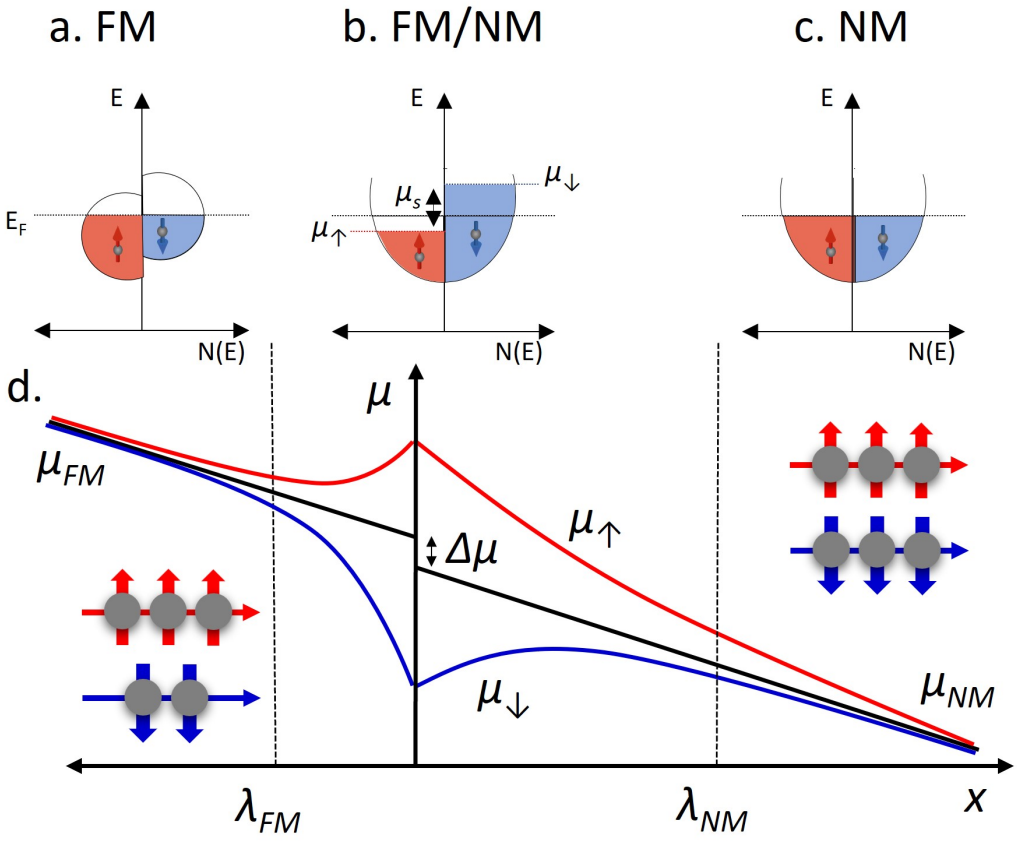

Figure 2.2: Schematic representation of the electrochemical potential (μ) for a FM/NM interface under an applied bias current (I_c). a. The d-bands of the FM represented by the spin-up (red) and spin-down (blue) subbands. **b.** The spin accumulation (μ_s), in the s-subband of the NM near the FM/NM interface due to an imbalance in the electrochemical potential for spin-up ($\mu_\uparrow$) and spin-down ($\mu_\downarrow$) electrons induced by spin injection of the FM with I_c. **c.** The s-subbands in the NM have the same amount of spin-up and spin-down electrons. The simplified Stoner model is used in panels a-c. **d.** Schematic representation of the spatial distribution of the electrochemical potential for spin-up (red line) and spin-down (blue line) electrons near the FM/NM interface, for I_c flowing along the $-x$ direction, generating a voltage $V = \Delta\mu/e$.

2

We can use the diffusive model ($\nabla n \neq 0$, $E = 0$) to describe the electron transport at the FM/NM interface. Away from the interface, $\mu_\uparrow$ and $\mu_\downarrow$ are the same. However, $\mu_\uparrow$ and $\mu_\downarrow$ split at the FM/NM interface, causing spin accumulation ($\mu_s = \mu_\uparrow - \mu_\downarrow$). The average of the spin-up and spin-down electrochemical potentials in the FM and the NM away from the interface is $\mu_{FM,NM} = (\mu_\uparrow + \mu_\downarrow)/2$, which is discontinuous when extrapolated at the interface. The discontinuity is given by $\Delta\mu$, which is related to the spin accumulation at the interface by [64]:

$$\Delta\mu = \frac{P}{2}\mu_s. \tag{2.6}$$

In the case of a transparent interface, $P = P_{FM}$ (see Eq. 2.2). In the case of a tunnel barrier present between the FM and the NM, the spin polarization P_{TB} is defined as:

$$P_{TB} = \frac{N_\uparrow(E_F) - N_\downarrow(E_F)}{N_\uparrow(E_F) + N_\downarrow(E_F)}, \tag{2.7}$$

where $N_{\uparrow,\downarrow}(E_F)$ corresponds to the FM layer. More generally, for any interface, the associated spin polarization P_I is given by:

$$P_I = \frac{R_I^\downarrow - R_I^\uparrow}{R_I^\downarrow + R_I^\uparrow}, \tag{2.8}$$

where $R_I^{\downarrow,\uparrow}$ are the spin-dependent interface resistances.

The statistical behavior for such an unbalanced system at the FM/NM interface can be described by the Boltzmann equation model. Valet and Fert showed that the Boltzmann equation model reduces to a macroscopic one when the mean free path is much smaller than the spin diffusion length ($l_e \ll \lambda_s$) such that the diffusion equations will become [65]:

$$j_{\uparrow(\downarrow)} = \frac{\sigma_{\uparrow(\downarrow)}}{e}\frac{\partial\mu_{\uparrow(\downarrow)}}{\partial x}, \tag{2.9}$$

where the current density flow is in the x direction, perpendicular to the FM/NM interface. If $\sigma_{\uparrow}$=$\sigma_{\downarrow}$ as in the case of a NM, then the spin current is defined as:

$$j_s = \frac{2\sigma}{e}\frac{\partial \mu_s}{\partial x}, \tag{2.10}$$

showing that a spin current is generated by a gradient in spin accumulation. By introducing the spin-flip process and particle conservation [64], one can find the one-dimensional (1D) spin diffusion equation developed by Valet and Fert [65]:

$$D\frac{\partial^2 \mu_s}{\partial^2 x} = \frac{\mu_s}{\tau_s}, \tag{2.11}$$

where D is the diffusion coefficient and τ_s the spin relaxation time of the material where the spins are diffusing, which are related to the spin diffusion length by $\lambda_s = \sqrt{D\tau_s}$. The general solution of the 1D spin diffusion equation for the spin accumulation is:

$$\mu_s = Ae^{-x/\lambda_s} + Be^{x/\lambda_s}, \tag{2.12}$$

where the integration constants A and B have to be determined in each material by taking into account the proper boundary conditions at the FM/NM interface (in terms of continuity of electrochemical potential and spin currents in space).

2.1.3 Spin transport and detection

A spin valve is a basic spintronic device used to study spin-dependent transport in metals and semiconductors, as in the case of the GMR introduced in the previous chapter. The spin-polarized currents that flow in this type of device are preferentially short-ranged, and there is no way to generate pure spin currents. Lateral spin valves (LSVs) are a second generation of spintronic devices in which pure spin currents can be generated, transported, manipulated, and detected. This is realized in a nonlocal configuration, where the bias current path and the voltage path are spatially separated. Since pure spin currents contain no net charge current, spurious effects such as anisotropic magnetoresistance (AMR) are avoided in this type of

2

device. A lateral spin valve (LSV) consists of two FM electrodes bridged by a perpendicular NM channel, see Fig. 2.3a.

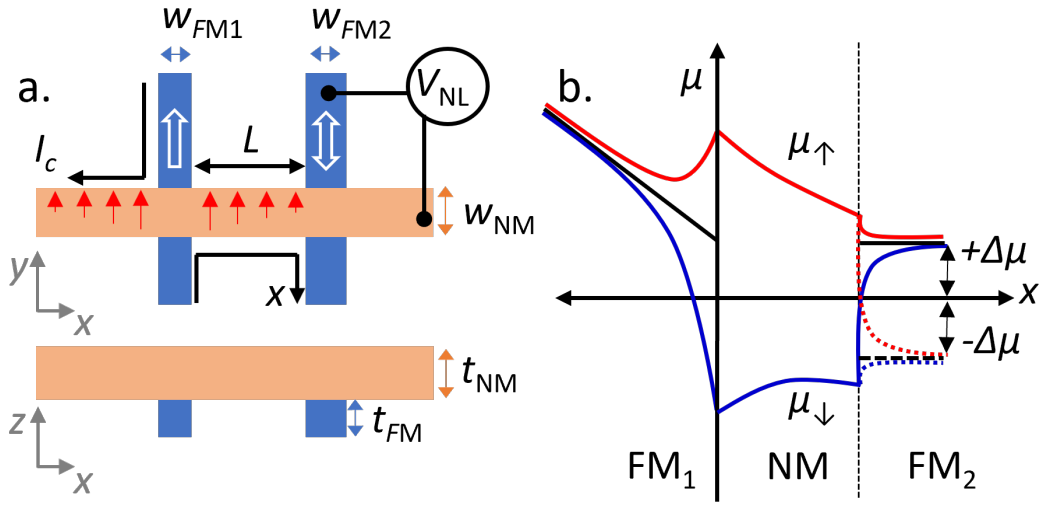

Figure 2.3: Schematic representation of a lateral spin valve. a. Sketch of a LSV. A LSV consists of two FM electrodes (FM_1 and FM_2) connected by a NM channel. The magnetization of FM_1 and FM_2 are represented by white arrows and can have a parallel or antiparallel configuration. Red arrows represent the spins diffusing along the NM channel. The nonlocal measurement configuration is also shown. **b.** Sketch of the spatial dependence of the electrochemical potential for spin-up (red) and spin-down (blue) electrons in a LSV along the x line shown in panel a, assuming a transparent FM/NM interface. Solid lines correspond to the parallel configuration, whereas dotted lines correspond to the FM_2 aligned antiparallel to the FM. Figure adapted from Ref. [66]

The first FM electrode (FM_1) acts as a spin injector by placing a bias current I_c between FM_1 and NM, creating a pure spin current that diffuses along the NM channel. A second FM electrode (FM_2) is placed at a certain distance from the FM injector (FM_1), close enough so that μ_s is still large enough to be detected and at the side where no I_c is flowing. At the FM_2/NM interface, the average μ_{NM} and μ_{FM2} are also discontinuous ($\Delta\mu$) due to the spin imbalance present at the interface. This $\Delta\mu$ generates a voltage, $V_s = \Delta\mu/e$, which could be measured with a voltmeter. The sign of $\Delta\mu$ depends on the relative orientation between the two FM electrodes (parallel and antiparallel), as shown in Fig. 2.3b.

The solution to Eq. 2.12, with the boundary conditions of continuity of $\mu_\uparrow$ and $\mu_\downarrow$ at the interface and conservation of spin-up and spin-down currents ($j_\uparrow$, $j_\downarrow$) across the interface, yields the following V_s [67], which is measured as a nonlocal voltage,

V_{NL}:

$$V_{NL} = 2I_c R_s^{NM} \frac{\hat{P}_1 \hat{P}_2}{r_1 r_2 - e^{-2L/\lambda_s^{NM}}} e^{-L/\lambda_s^{NM}} \tag{2.13}$$

where

$$r_i = 2Q_{Ii} + 2Q_i + 1, \tag{2.14}$$

and

$$\hat{P}_i = P_{Ii} Q_{Ii} + P_i Q_i, \tag{2.15}$$

with $Q_{Ii} = \frac{1}{1-P_{Ii}^2} \frac{R_{Ii}}{R_s^{NM}}$ and $Q_i = \frac{1}{1-P_i^2} \frac{R_s^i}{R_s^{NM}}$, $i = 1$ and 2 refer to the FM_1 (injector), and FM_2 (detector), respectively. L is the distance from FM_1 to FM_2 as shown in Fig. 2.3a. P_i is the spin polarization of the FM at the injector ($i = 1$) and the detector ($i = 2$), λ_s^{NM} is the spin diffusion length of the NM channel. R_{Ii} is the resistance at the interface i. R_s^{NM} and R_s^i are the spin resistances for the NM channel and the FM_i electrode, respectively. P_{Ii} is the spin polarization at the i interface.

An important parameter that appears in Eq. 2.13 is the spin resistance, R_s. This is related to the resistance of the material to allow the spin current to flow. Therefore, the spin current will not tend to pass through materials with high spin resistances. The most general definition of spin resistance, regardless of whether the material is a FM or a NM, is $R_s = \rho\lambda_s^2/V$, where ρ is the electrical resistivity of the material, λ_s is the spin diffusion length, and V is the volume of the material through which the spin current diffuses.

In the case of a FM, since they usually have a very short spin diffusion length, the spin current decays very close to the FM/NM interface, then $V = w_{FM} w_{NM} \lambda_s^{FM}$, where w_{FM} and w_{NM} are the widths of the FM and NM, respectively (see Fig. 2.3a). In this order, the spin resistance in the FM is defined as:

$$R_s^{i=1,2} = R_s^{FM} = \frac{\rho_{FM} \lambda_s^{FM}}{w_{FM} w_{NM}}. \tag{2.16}$$

For the case of a NM material used for spin transport in LSV devices, the spin diffusion length is much longer than the channel dimensions ($\lambda_s^{NM} >> w_{NM}, t_{NM}$,

where t_{NM} is the thickness of the NM). Therefore, the spin resistance in the NM is defined as:

$$R_s^{NM} = \frac{\rho_{NM}\lambda_s^{NM}}{w_{NM}t_{NM}}. \tag{2.17}$$

The nonlocal resistance, R_{NL}, is defined as the measured voltage normalized by the injected current, I_c:

$$R_{NL} = \frac{V_{NL}}{I_c}. \tag{2.18}$$

R_{NL} is not a real resistance, since the charge current injection path is spatially separated from the voltage detection. The value of this resistance can be positive or negative depending on the relative magnetization of the injector and the detector electrodes. When both FM electrodes are in a parallel configuration ($\uparrow\uparrow$, $\downarrow\downarrow$), the FM acting as a detector will be sensitive to the injected excess spin population, and the measured voltage will be positive. If the FM electrodes are in the antiparallel configuration ($\uparrow\downarrow$, $\downarrow\uparrow$) the detector will be sensitive to the opposite spin orientation, and therefore a negative voltage with the same magnitude will be measured (see Figs. 2.3b and 2.4b). The magnetization configuration of the FM electrodes can be controlled by sweeping an external magnetic field (H_y), in the easy axis of the FM. Figure 2.4b shows the characteristic shape of R_{NL} as a function of H_y in a LSV. The difference in R_{NL} between the parallel and antiparallel magnetic configuration is called the nonlocal spin signal ($\Delta R_{NL} = R_{NL}^P - R_{NL}^{AP}$) and is given by [68]:

$$\Delta R_{NL} = 4R_s^{NM}\frac{\hat{P}_1\hat{P}_2}{r_1r_2 - e^{-2L/\lambda_s^{NM}}}e^{-L/\lambda_s^{NM}} \tag{2.19}$$

Equation 2.19 can be used to extract λ_s^{NM}, and P_I or P_{FM} by measuring different distances between FM electrodes, L. This can be done in a series of LSVs with the same parameters, such as the sample shown in Fig. 2.4a. This method works when L is of the order of λ_s^{NM}, because if L is much longer the spin accumulation, and therefore ΔR_{NL} vanishes as shown in Fig. 2.4c. Considering that the lateral resolution of the standard nanofabrication techniques is of the order of tens of nanometers, this technique is useful to extract λ_s^{NM} of light NM metals such as Al [64, 69],

Cu [64, 70] or Ag [71], which are characterized by λ_s^{NM} of hundreds of nm. On the other hand, materials with λ_s^{NM} of a few nanometers, such as SOM or some FM metals, cannot be used as spin channels in standard LSVs. For these cases, there is an alternative approach to extract the short λ_s^{NM}: the **spin absorption** technique.

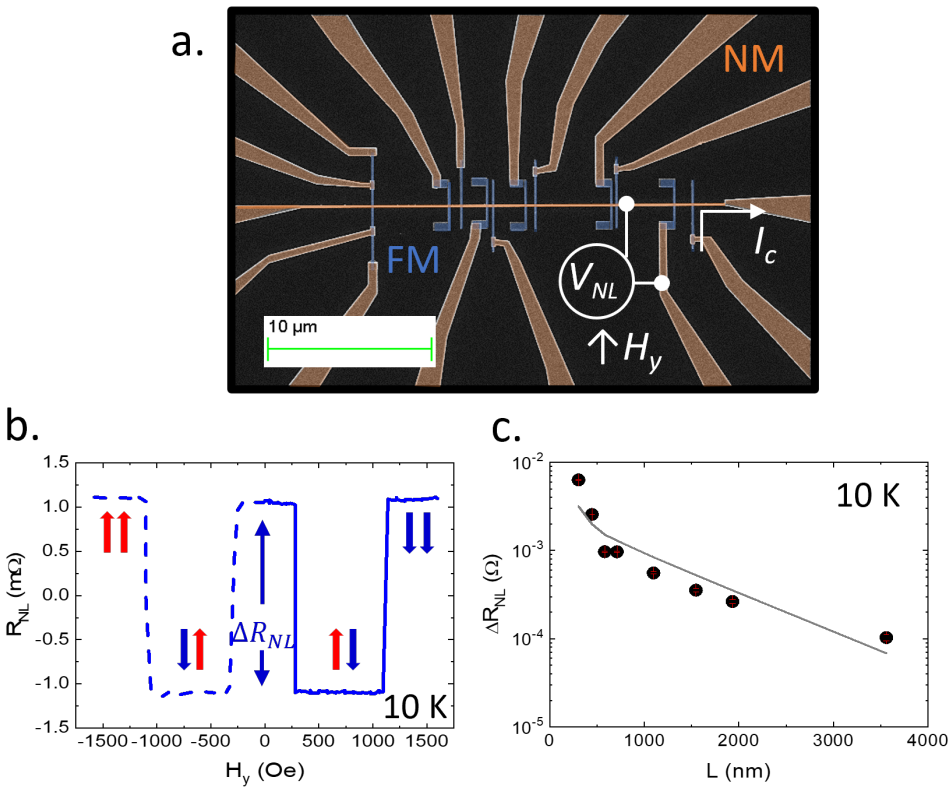

Figure 2.4: Nonlocal measurements for spin accumulation in a LSV. a. Scanning electron microscopy (SEM) image for LSVs with different distances (L) between injector and detector electrodes. The FM and NM electrodes are false-colored in blue and orange, respectively. The nonlocal measurement configuration is indicated by the white lines. **b.** The magnetic field dependence of the nonlocal resistance $R_{NL} = V_{NL}/I_c$ of a Py/Cu LSV at 10 K. At large external magnetic fields (H_y), FM_1 and FM_2 are parallel to each other. By sweeping H_y, one FM electrode switches (antiparallel configuration) and, as a consequence, R_{NL} changes sign until the other FM switches and both FM are parallel again. The nonlocal spin signal ΔR_{NL} is the difference in resistance between the parallel and antiparallel states. **c.** ΔR_{NL} as a function of L for Py/Cu LSVs at 10 K. The gray solid line is the fit of the data using Eq. 2.19.

2

2.1.4 Spin absorption

The spin absorption technique is based on the LSV devices, but with an additional wire of the material to be studied, *i.e.* a SOM [72–75] or a FM metal [70], for which the spin diffusion length is to be known. This wire is added between the two FM electrodes (injector and detector) as shown in Fig. 2.5a. Similarly to what we explained before, when the pure spin current flows along the NM channel, part of the spin current is absorbed by the middle wire [76], *e.g.* the SOM, resulting in a smaller detected spin signal in the FM detector, as shown in the example of Fig. 2.5b. The amount of spin current absorbed depends on the spin resistance of the middle electrode and the interface between the NM channel and the middle electrode. The detected nonlocal spin signal, ΔR_{NL}^{abs} is given by:

$$\Delta R_{\mathrm{NL}}^{abs} = 4R_s^{NM}\hat{P}_1\hat{P}_2\frac{(r_3-1)e^{-L/\lambda_s^{NM}}}{r_1r_2(r_3-Q_{I3})-r_1(1+Q_{I3})e^{-2(L-l)/\lambda_s^{NM}}-r_2(1+Q_{I3})e^{-2l/\lambda_s^{NM}}-(r_3-Q_{I3})e^{-2L/\lambda_s^{NM}}+2e^{-2L/\lambda_s^{NM}}}, \tag{2.20}$$

Where $i=3$ refers to the middle wire (SOM or FM metal). l is the distance from the injector (FM_1) to the SOM. In our case, the SOM is at the middle of both FM electrodes as shown in Fig. 2.5a, then $L=2l$. The remaining parameters are defined in Eqs. 2.13-2.15. Note that this equation is valid for the most general case, which means that the middle wire could also be a ferromagnet. Usually, the middle wire is a SOM with strong spin-orbit coupling (SOC) and, in this case, the spin polarization is $P_3=P_{I3}=0$. Additionally, we note that when Eq. 2.20 considers a $r_3\to\infty$, there is no effect of the middle wire on the LSV and the equation tends back to Eq. 2.19.

The spin resistance of the middle wire, when is a SOM with short λ_s (a few nanometers), is defined by the following equation [77]:

$$R_s^{i=3}=R_{\mathrm{s}}^{SOM}=\frac{\rho_{SOM}\lambda_s^{SOM}}{w_{NM}w_{SOM}\tanh\frac{t_{SOM}}{\lambda_s^{SOM}}}, \tag{2.21}$$

where ρ_{SOM}, w_{SOM} and t_{SOM} are the resistivity, width and thickness of the middle wire. The nonlocal spin absorption signal allows to extract the spin diffusion length of the SOM, λ_s^{SOM}, if the spin properties of the NM channel and the FM electrodes are known. The 1D spin diffusion model employed in this section is valid as long as w_{SOM} is smaller than λ_s^{NM}.

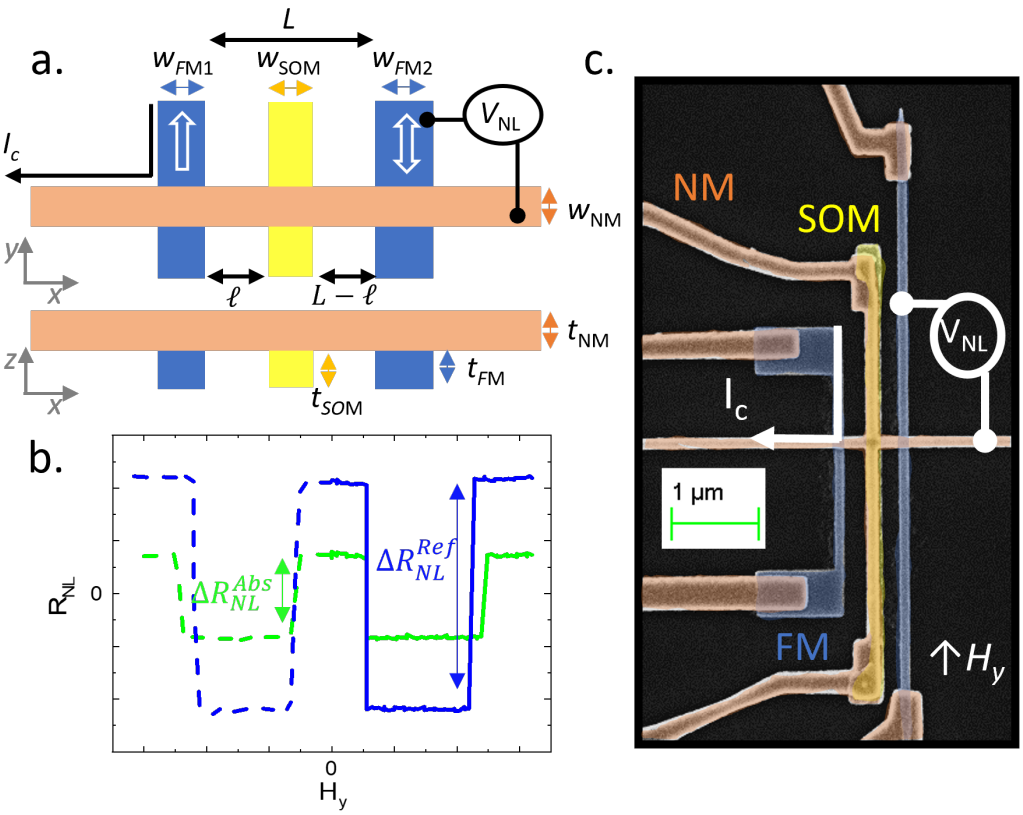

Figure 2.5: Nonlocal measurements for spin absorption in a LSV. a. Schematic representation of a LSV for spin absorption measurements in a top and lateral view, **b.** The magnetic field dependence of the nonlocal resistance R_{NL} for the reference and the absorption device. The corresponding spin signals, ΔR_{NL}^{Ref} and ΔR_{NL}^{Abs} are labeled. **c.** SEM image for a LSV for absorption measurements. The SOM wire is false-colored in yellow. The nonlocal measurement configuration is shown by the white lines.

2.2 Spin-charge interconversion

Spin-charge interconversion (SCI) is a crucial way to generate and detect spin currents without the use of a FM material by exploiting the SOC of materials. The discovery of the spin Hall effect (SHE) [78] and the Rashba-Edelstein effect (REE)[79] led to the birth of the field of spin-orbitronics. Devices based on spin-orbitronics are being optimized for the next generation of MRAM and are considered promising for more energy-efficient logic circuits such as MESO logic, as explained in Chapter 1. In this section, we introduce SOC, SCI, and the mechanisms behind SCI, which are essential to understand the advances made in this thesis.

2.2.1 Spin-orbit coupling in solids

The interaction between the spin angular momentum, S, and the orbital angular momentum, L, of an electron in an atom is known as spin-orbit coupling (SOC). The relativistic effect of SOC is that S interacts with an effective magnetic field (induced by L) that the electrons feel in the absence of an external magnetic field. This leads to a splitting of the atomic energy levels, similar to the Zeeman splitting [80]. SOC splits degenerate spin subbands, modifying the electronic band structure, and induces novel spin-dependent transport phenomena. In a solid, the potential acting on the electron is composed of a periodic component associated with the band structure and a non-periodic component associated with impurities, boundaries, and the external applied field. Moreover, SOC can also occur in systems with broken inversion symmetry, such as metallic surfaces and interfaces, giving rise to the so-called Rashba SOC [81]. All these components give rise to a variety of spin-dependent transport phenomena, among which SHE and the REE.

2.2.2 Spin Hall effect

In 1971, a theoretical work by D'ayokonov and Perel [82, 83] realized that, due to the SOC in NM materials, electrons should deflect in transverse directions according to their spin carriers when scattering in the presence of impurities. This scattering generates a spin imbalance with an associated spin current, as shown in Fig. 2.6a. In 1999, Hirsch, unaware of the research of D'ayokonov and Perel, rediscovered the effect and gave the name SHE to this phenomenon [78]. Reciprocally, a spin current (which can be a spin-polarized current or a pure spin current) can induce a transverse charge current, which is known as the ISHE, as shown in Fig. 2.6b. Note that its origin is very closely related to the anomalous Hall effect (AHE) in ferromagnets discovered in 1881 [84].

The relationship between the charge current density (j_c) and the spin current density (j_s) for the SHE and the ISHE are:

$$\boldsymbol{j_s} = \left[\frac{\hbar}{e}\right] \theta_{SH} (\boldsymbol{j_c} \times \boldsymbol{s}) \tag{2.22}$$

and

$$\boldsymbol{j_c} = \left[\frac{e}{\hbar}\right] \theta_{ISH} (\boldsymbol{j_s} \times \boldsymbol{s}), \tag{2.23}$$

respectively, where s is the spin orientation, θ_{SH} is the spin Hall angle that is the charge-to-spin conversion efficiency, and θ_{ISH} the spin-to-charge conversion efficiency. $\theta_{SH} = \theta_{ISH}$ following the Onsager reciprocity [85].

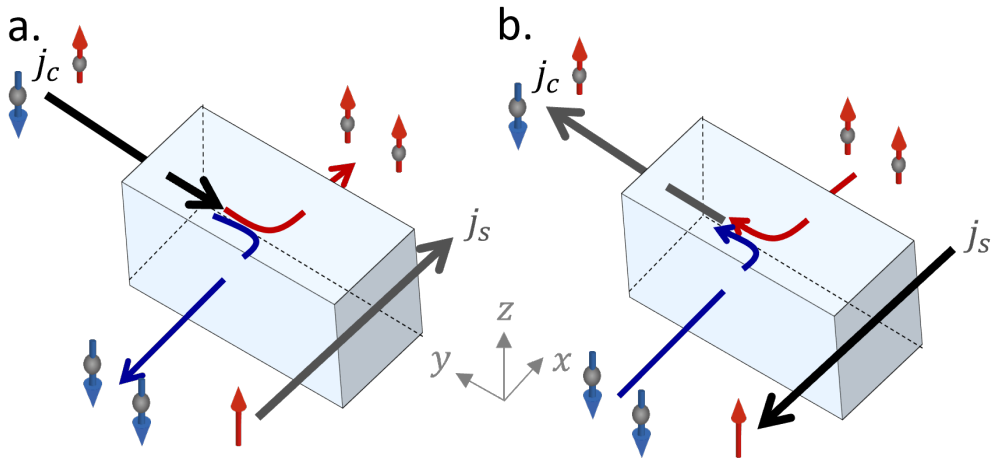

Figure 2.6: Spin Hall effect and its inverse. a. The direct SHE occurs when applying a charge current (j_c) into a bulk SOM, in which electrons with opposite spins (spin-up and spin-down are represented by red and blue arrows, respectively) deflect in opposite direction, inducing a transverse spin current (j_s). **b.** The inverse effect (ISHE) occurs when j_s is injected into a SOM, the spins-up and spins-down deflect in the same direction, generating a transverse j_c.

The spin Hall angle is defined as the ratio between the transverse spin Hall resistivity, ρ_{xy} (or transverse spin Hall conductivity σ_{xy}) and the longitudinal resistivity, ρ_{xx} (conductivity σ_{xx}) as follows:

$$\theta_{SH} = \frac{\sigma_{xy}}{\sigma_{xx}} = -\frac{\rho_{xy}}{\rho_{xx}}, \tag{2.24}$$

It is important to note that θ_{SH} can be estimated by different methods, as we will explain in section 2.3. Each technique has different ways of measuring and analyzing, and this leads to a large dispersion of θ_{SH} values reported for the same materials [86]. An important reason is the role of the interface, since the majority of techniques require the use of FM/SOM heterostructures. Ignoring the interface in the quantification can easily lead to an incorrect estimation of θ_{SH}.

2

2.2.3 Mechanisms of the spin Hall effect

The SOC can act as an effective magnetic field that deflects the spin-up and spin-down electrons in opposite directions. This effect is known to have different origins in the AHE [87] and is accepted to apply also to the SHE [72, 73, 86, 88]. In particular, the SHE can arise from an intrinsic mechanism related to the band structure and two extrinsic contributions related to impurities [86]. The total spin Hall resistivity can be described as [73]:

$$-\rho_{xy} = \rho_{xy}^{int} + \rho_{xy}^{ss} + \rho_{xy}^{sj}, \tag{2.25}$$

where ρ_{xy}^{int} is the component induced by the intrinsic effect and the extrinsic components are the skew-scattering (ρ_{xy}^{ss}) and the side-jump scattering (ρ_{xy}^{sj}). A brief description of each mechanism is given below:

1. The intrinsic contribution was proposed by Karplus and Luttinger to explain the AHE [89]. It is related to the spin-dependent electronic band structure for a perfect crystal [90]. The intrinsic mechanism in the presence of an electric field (E) is shown in Fig. 2.7a. This contribution, as in the AHE, scales quadratically with the resistivity of the material, $\rho_{xy}^{int} = \sigma_{xy}^{int}\rho_{xx}^{2}$, where the intrinsic transverse conductivity σ_{xy}^{int} is a constant parameter that depends on the Berry curvature at the Fermi level [91].

2. One of the extrinsic contributions is due to the oblique scattering mechanism. This mechanism was proposed by Smit in 1958 [92]. It is related to the spin-dependent chiral features that appear for scattering events producing a disorder potential in the presence of a SOC. Figure 2.7b shows the skew scattering mechanism; when an electron with a given spin scatters with an impurity or defect, it is deflected with an angle α_{ss}. The contribution of the skew scattering mechanism to the spin Hall resistivity is given by $\rho_{xy}^{ss} = \alpha_{ss}\rho_{xx,0}$, where $\rho_{xx,0}$ is the residual resistivity [93].

3. Another extrinsic contribution is the side-jump scattering mechanism, introduced by Berger [94]. In this case, during scattering, electrons with opposite spins feel opposite electric fields when approaching a scattering center, generating a lateral displacement of the electrons opposite for spin-up and spin-down as shown in Fig. 2.7c. The contribution of the side-jump mechanism to the spin Hall resistivity scales with the square of the residual resistiv-

ity: $\rho_{xy}^{sj} = \sigma_{xy}^{sj}\rho_{xx,0}^{2}$, where σ_{xy}^{sj} is the transverse conductivity associated with the side-jump mechanism.

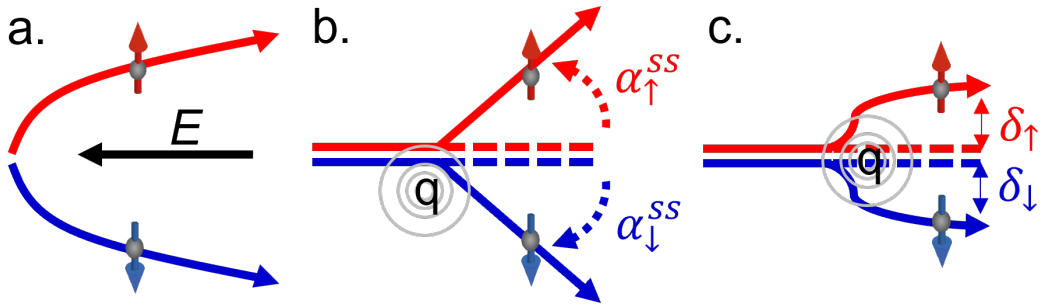

Figure 2.7: Mechanisms of the Spin Hall effect. Schematic representation of the different mechanisms that originate the SHE: **a.** Intrinsic mechanism, **b.** skew-scattering, **c.** side-jump scattering.

A careful study of ρ_{xy} as a function of ρ_{xx} and $\rho_{xx,0}$ allows one to obtain the different contributions, as has been recently done in Pt [72] and Ta [73].

2.2.4 Rashba–Edelstein effect

Similar to the previous section for the SHE, it is possible to have SCI through the REE in two-dimensional (2D) systems with SOC materials and asymmetry in the crystal potential (broken space inversion symmetry) [79, 95, 96]. The breaking of inversion symmetry splits the spin subbands which are otherwise degenerated, as despicted in Fig. 2.8a. Such spin splitting is know as Rashba or Bychkov–Rashba effect [97]. Edelstein proposed that the combination of this momentum-dependent spin polarization together with an electric current induces spin accumulation [79]. The resulting spin accumulation has a perpendicular, in-plane polarization and can diffuse as a spin current. From an experimental point of view, therefore a system with REE converts a 2D charge current into a three-dimensional (3D) spin current with in-plane spin polarization [98].

The structural inversion asymmetry at the surface or interface creates an electric potential normal to it. The Rashba Hamiltonian ($\hat{H}_R$) describes the interaction between the momentum ($\hbar k$) and the spin as follows:

$$\hat{H}_R = \alpha_R(\hat{z} \times \boldsymbol{k})\boldsymbol{s}, \tag{2.26}$$

where $\hat{z}$ is the direction normal to the 2D plane and α_R is the Rashba coefficient proportional to the strength of the SOC and electric potential. $\boldsymbol{k}$ is the wave vector and, for each k, the energy of the band splitting for the spin-up and spin-down is given by:

$$E_{\uparrow(\downarrow)}(k) = \frac{\hbar^2 k^2}{2m_e} \pm \alpha_R k. \tag{2.27}$$

In the Rashba effect, the spin polarization is locked to its momentum, which generates the spin-subband splitting of the surface or interface states (Fig. 2.8a). Figure 2.8b shows the shift of the Fermi contours when a 2D current density (J_c^{2D}) is applied along the x-axis. In k-space, there is a shift of the Fermi contours, Δk_x, such that the spin population of spin-up and spin-down is not balanced, and the system now presents a spin accumulation (μ_s), which is proportional to Δk_x. The spin accumulation can diffuse as a 3D spin current density (J_s^{3D}). In the REE, the charge-to-spin conversion efficiency is given by [99, 100]:

$$q_{REE} = \frac{j_s^{3D}}{j_c^{2D}} \, [\mathrm{m}^{-1}]. \tag{2.28}$$

Reciprocally, the inverse Rashba-Edelstein effect (IREE) converts a spin accumulation with an in-plane polarization injected at a 2D system into a perpendicular charge current. The injection of an imbalanced spin density into a Rashba system from a J_s^{3D} along the z-axis shifts the Fermi contours in the opposite direction and an effective Δk_x^{in} and Δk_x^{out} is generated, giving rise to a net j_c^{2D} along the x-axis, see Fig. 2.8c. The efficiency of IREE is given by the IREE length [99, 101]:

$$\lambda_{IREE} = \frac{j_c^{2D}}{j_s^{3D}} \, [\mathrm{m}]. \tag{2.29}$$

Note that λ_{IREE} has a dimension of length (m). A careful discussion about the comparison between the SHE and IREE efficiencies is reported in Ref. [102].

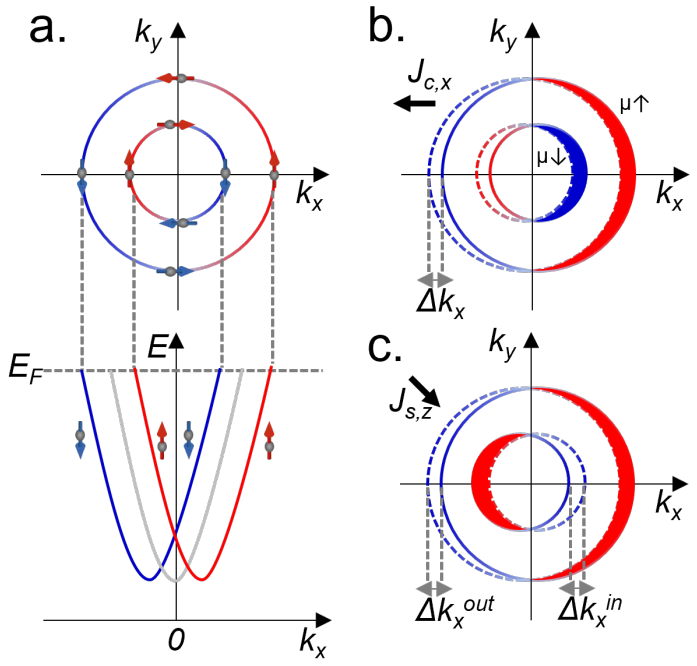

Figure 2.8: Band structure of a Rashba system and Rashba-Edelstein effect. a. Rashba effect: spin-split energy dispersion curves of a two-dimensional electron gas (2DEG) with inversion symmetry breaking. The lower panel presents the reference band in grey and the shifted curves for spin-up in red and spin-down in blue. The upper panel is the cut at the Fermi level. **b.** Schematic representation of the REE where a spin accumulation (μ_s) is generated when a charge current along x-direction ($J_{c,x}$) is injected and creates a shift of the Fermi contours Δk_x. **c.** Schematic representation of the IREE where a charge current is created when injecting a spin current along z-direction ($J_{s,z}$). Fermi contours move in opposite direction (Δk_x^{in} and Δk_x^{out}).

The REE/IREE, was first experimentally demonstrated at the interface between Bi and Ag metals [98], and later reported at other all-metallic interfaces [103, 104], metal/oxide interfaces [99, 101, 105, 106], 2DEG systems [107, 108], surface states of topological insulators [100, 109] and van der Waals heterostructures [110–115]. The Onsager reciprocity between the direct and inverse REE has been observed electrically using LSVs [99, 101, 103].

In high-symmetry bulk SOMs, a charge current density (j_c) is transformed into a spin current density perpendicular to j_c and s by the SHE according to Eqs. 2.22 and 2.23 (where j_s, j_c and s are mutually orthogonal). In 2D systems without structural inversion symmetry (explained in this section), an in-plane j_c leads to a perpendicularly polarized spin accumulation by the REE. This condition of orthogonality is imposed by the mirror symmetry present in these systems.

Breaking mirror symmetry in the system will allow SCI of spins polarized also along non-orthogonal directions, a feature that is not achievable in highly symmetric materials [116–119]. Additional SCI components emerge in layered materials with reduced symmetry, such as van der Waals heterostructures, where the symmetries that govern the permitted SCI processes via the REE depend on the alignment between graphene and a transition metal dichalcogenide flake [120, 121]. In twisted heterostructures, besides the conventional REE, where the charge current induces a perpendicular spin polarization, the broken mirror symmetry leads to an unconventional REE with parallel spin polarization. Experimentally, such an unconventional REE has been recently observed in graphene/$MoTe_2$ [113, 114], graphene/WTe_2 [115], and graphene/$NbSe_2$ [112] heterostructures.

2.3 Spin-charge interconversion measurement techniques

2.3.1 Nonlocal devices for the spin Hall effect

Previously, in section 2.1.4, we demonstrated how a middle wire added to a LSV can absorb part of the pure spin current flowing in the NM channel if its spin resistance is low enough. Usually the middle wire is made of a material with strong SOC. This means that the pure spin current absorbed by the SOM wire can be converted into a measurable charge current due to the ISHE, making the SCI experimentally measurable in the same device.

The injection of the spin current is the same as the spin injection in the LSVs explained in section 2.1.3, in which a bias current (I_c) is applied from the FM injector to the NM channel. To measure the ISHE, the spin detector is now the SOM wire, in which the voltage probe is connected to, as shown in Fig. 2.9a, and the external magnetic field is now applied in plane but in the hard axis ($\pm x$ direction) of the FM injector. Figure 2.9b illustrates the flow of spin current, charge current and spin polarization. The pure spin current flowing in the NM channel is partially absorbed by the SOM ($-z$ direction) and converted into a charge current ($\pm I_{ISHE}$) via the ISHE in the $+y$ or $-y$ direction depending on the spin polarization direction, which is reversed by changing the FM magnetization with the external magnetic field. The generated I_{ISHE} can be picked up as an open-circuit voltage, V_{ISHE}. The difference in the ISHE resistance ($R_{ISHE} = V_{ISHE}/I_c$) for both saturated magnetizations is twice the ISHE signal: $2\Delta R_{ISHE} = R^{\rightarrow}_{ISHE} - R^{\leftarrow}_{ISHE}$.

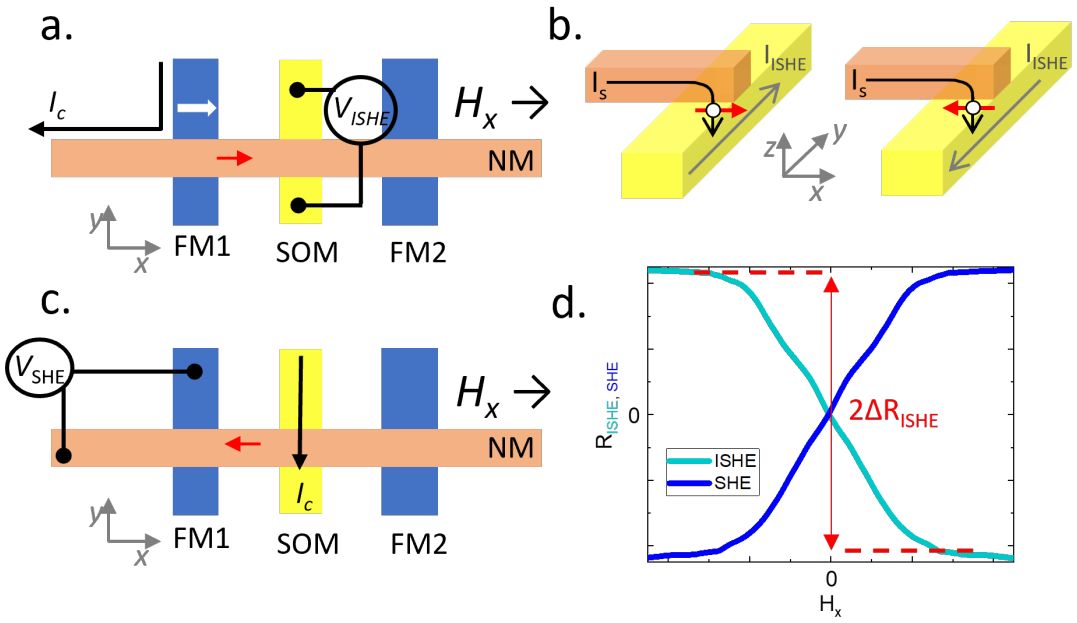

Figure 2.9: Nonlocal devices to measure the spin Hall effect. a. Schematic representation of the nonlocal ISHE device. The black lines represent the measurement configuration. **b.** In the ISHE, a spin current (I_s) is injected (black arrow) into the SOC material, and this deflects the spin carriers in the same direction creating a charge current (I_{ISHE}) that reverts sign accordingly with the spin polarization direction. **c.** Schematic representation of the nonlocal SHE device. **d.** The R_{ISHE} and R_{SHE} as a function of the external magnetic field (H_x). The change in the resistance from positive to negative magnetic fields gives the spin-to-charge conversion signal, $2\Delta R_{(I)SHE}$ which is proportional to the spin Hall angle.

The SHE can be measured by inverting the injector and detector electrical probes as shown in Fig. 2.9c. In this case, the injection is done by applying the charge current (I_c) directly into the SOM, where it is converted into a transverse spin current via the SHE. This spin current will diffuse into the NM channel until it reaches the FM, which will act as a detector according to the same process explained in section 2.1.3, and the output will be measured as a voltage, V_{SHE}. The spin Hall resistance is defined as $R_{SHE} = V_{SHE}/I_c$. Figure 2.9d shows the characteristic plot for R_{SHE} and R_{ISHE} as a function of H_x. Both curves have the same amplitude, but the sign is reversed due to the swapping of injector and detector. According to Onsager's reciprocity [85] $R_{ISHE}(H) = R_{SHE}(-H)$ and, therefore, the spin Hall signal has the same amplitude and opposite sign to its inverse, $\Delta R_{ISHE} = -\Delta R_{SHE}$.

The relation between the experimentally measured ΔR_{ISHE} and the spin Hall resistivity $\rho_{xy} = \rho_{SH}$ is given by [77, 122]:

$$\rho_{SH} = -\frac{w_{SOM}}{x_{SOM,NM}} \left(\frac{I_c}{\bar{I}_s}\right) \Delta R_{ISHE}, \tag{2.30}$$

where $x_{SOM,NM}$ is the shunting factor that accounts for the current in the SOM being shunted through the NM channel. Depending on the sheet resistance value of the NM channel compared to the one of the SOM wire, the charge current generated along the SOM wire partially flows back into the NM channel, effectively lowering the output voltage. $x_{SOM,NM}$ is sensitive to the geometry of the device and relevant for the proper quantification of ρ_{SH} and θ_{SH}.

The effective spin current ($\bar{I}_s$) injected into the SOM along the $-z$ direction is the one that contributes to the ISHE because the spin current at the SOM/NM interface ($z = 0$) is diffused into the SOM thickness. $\bar{I}_s$ is given by the following equation [77, 122]:

$$\frac{\bar{I}_s}{I_c} = \frac{\int_0^{t_{SOM}} I_s(z)dz}{t_{SOM} I_c} = \frac{\lambda_s^{SOM}\left(1 - e^{-\frac{t_{SOM}}{\lambda_s^{SOM}}}\right)^2}{t_{SOM}\left(1 - e^{-\frac{2t_{SOM}}{\lambda_s^{SOM}}}\right)} \frac{I_s(z=0)}{I_c}. \tag{2.31}$$

The prefactor, $I_s(z = 0)/I_c$, is given by the following equation:

$$\frac{I_s(z=0)}{I_c} = \frac{2\hat{P}_1\left[r_2(1-Q_{I3})e^{-l/\lambda_s^{NM}} - (1+Q_{I3})e^{-(2L-l)/\lambda_s^{NM}}\right]}{r_1 r_2(r_3 - Q_{I3}) - r_1(1+Q_{I3})e^{-2(L-l)/\lambda_s^{NM}} - r_2(1-Q_{I3})e^{-2l/\lambda_s^{NM}} - (r_3 - Q_{I3})e^{-2L/\lambda_s^{NM}} + 2e^{-2L/\lambda_s^{NM}}}, \tag{2.32}$$

Note that the spin diffusion length of the SOM, λ_s^{SOM}, is an indispensable parameter to determine the spin Hall angle (θ_{SH}).

Importantly, the spin absorption technique allows us to independently extract in the same LSV device λ_s^{SOM} and θ_{SH} of the SOM wire, simply by changing the measurement configuration (Figs. 2.5 and 2.9).

2.3.2 Local devices for the spin Hall effect

The local spin Hall configuration is the equivalent of the readout node in the proposed MESO logic device discussed in Chapter 1. Local devices can be used to mea-

sure ISHE in a SOM by locally injecting a spin-polarized current at the SOM/FM interface, as shown in Fig. 2.10. Due to the direct contact between the SOM and the FM, larger output signals are obtained in contrast to nonlocal spin Hall devices.

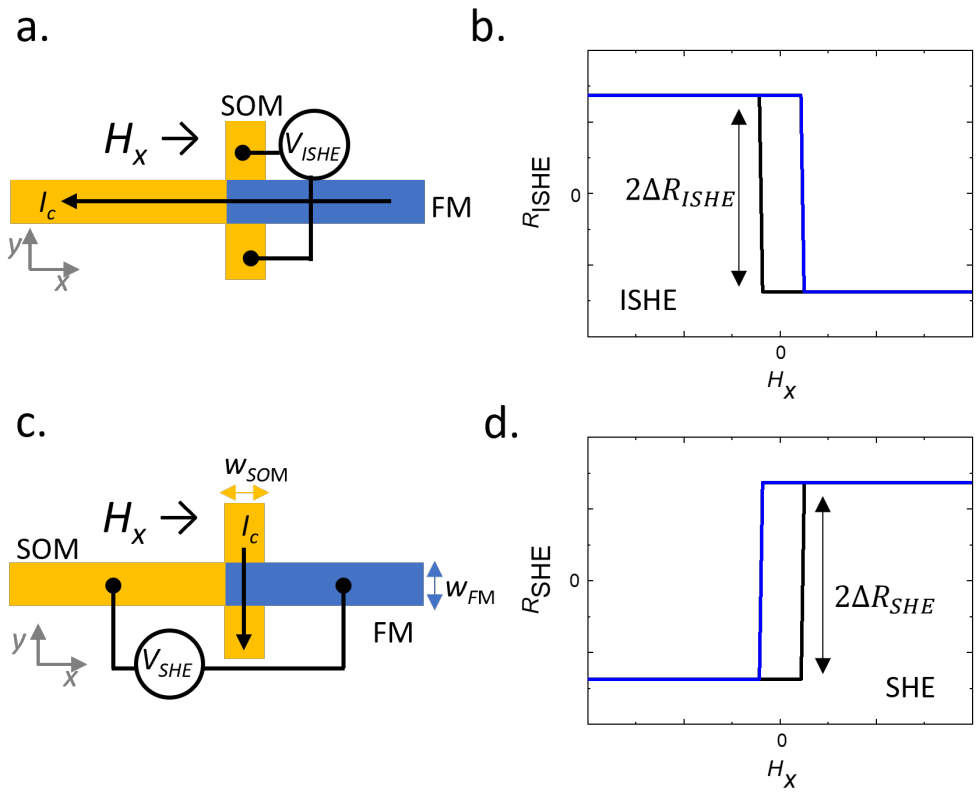

Figure 2.10: Local devices for Spin Hall effect. a. Schematic representation of the local spin Hall device, which consists of a T-shaped SOM electrode and a FM electrode, with the ISHE measurement configuration. **b.** The ISHE resistance as a function of the external magnetic field. **c.** Schematic representation of the SHE measurement configuration. **d.** ISHE resistance as a function of the external magnetic field. In both b and d panels, the trace is in blue and the retrace is in black, and the difference in resistance between positive and negative magnetic fields is $2\Delta R_{(I)SHE}$.

Local spin Hall devices consist of a T-shaped nanostructure made of SOM and a FM electrode placed in such a way that the tip of the FM overlaps the intersection of the T-shaped nanostructure. In the same device, it is possible to measure the ISHE and the SHE as shown in Figs. 2.10a and 2.10c, respectively. The external magnetic field is applied along the easy axis of the FM.

In the case of the ISHE, a charge current I_c is applied from the FM to the SOM, leading to a x-spin-polarized current into the SOM in the $-z$-direction. The SOM

produces a transverse charge current (I_{ISHE}), which is detected as an open-circuit voltage, V_{ISHE}, in the arms of the T-shaped electrode. Reversing the magnetization direction of the FM causes a change in the sign of I_{ISHE} and thus a change in V_{ISHE}. We can normalize this voltage to the applied current as $R_{ISHE} = V_{ISHE}/I_c$.

In Fig. 2.10b, the R_{ISHE} in the local device is shown as a function of the external magnetic field applied in x-direction. The sharp reversal of the magnetization from $-x$-direction to $+x$-direction gives a change in the sign of the resistance R_{ISHE}. The same behavior is obtained by reversing the magnetization, with a hysteresis associated with the shape anisotropy of the FM electrode. The difference between the two resistances is the inverse spin Hall signal $2\Delta R_{ISHE}$. Note that, since the change in resistance is associated with the magnetic state of the FM, the way to read out the magnetic state is as in the proposed MESO device introduced in Chapter 1.

Similar to the ISHE, but only by changing the configuration of the electrical contacts (Fig. 2.10c), we could measure the SHE signal (Fig. 2.10d), in this case by applying I_c to the transverse arms of the T-shaped SOM electrode. In this way, a spin current polarized in the x-direction and flowing along the z-direction is generated by the SHE. The tip of the FM at the top of the T-shaped can sense the spin accumulation at the interface and is measured as an output voltage, V_{SHE}. Following the Onsager reciprocity [85], the ISHE and SHE signals are equal, but with opposite sign ($2\Delta R_{ISHE} = -2\Delta R_{SHE}$).

Using the 1D spin diffusion model, it is possible to analyze and quantitatively explain the output signals coming from the ISHE. Based on the two-channel model (section 2.1.1) and Refs. [34, 123, 124], the spin Hall signal coming from the local T-shaped device can be written as:

$$\Delta R_{\text{(I)SHE}} = \frac{P_{FM}\theta_{SH}\lambda_s^{SOM}}{\left(\frac{t_{FM}}{\rho_{FM}} + \frac{t_{SOM}}{\rho_{SOM}}\right) w_{SOM}} \times \frac{1 - \frac{1}{cosh(t_{SOM}/\lambda_s^{SOM})}}{tanh(t_{SOM}/\lambda_s^{SOM}) + \frac{\lambda_s^{SOM}\rho_{SOM}}{\lambda_s^{FM}\rho_{FM}^*} tanh(t_{FM}/\lambda_s^{FM})}, \tag{2.33}$$

where $\rho_{FM}^* = \rho_{FM}/(1 - P_{FM}^2)$. P_{FM}, $\lambda_s^{SOM,FM}$, and $\rho_{SOM,FM}$ are the spin polarization of the FM, the spin diffusion length and the resistivity, respectively. The subscripts denote the materials.

For systems with dimension materials (thickness) much shorter than the spin diffusion length, as the devices in this thesis where $\lambda_s^{SOM} << t_{SOM}$ and $\lambda_s^{FM} << t_{FM}$, a simplified expression for Eq. 2.33 is given by:

$$\Delta R_{\text{(I)SHE}} = G \times \lambda_{eff}, \tag{2.34}$$

where

$$G = \frac{1}{\left(\frac{t_{FM}}{\rho_{FM}} + \frac{t_{SOM}}{\rho_{SOM}}\right) w_{SOM}} \tag{2.35}$$

and

$$\lambda_{eff} = \frac{P_{FM}\theta_{SH}\lambda_s^{SOM}}{1 + \frac{\lambda_s^{SOM}\rho_{SOM}}{\lambda_s^{FM}\rho_{FM}^*}}. \tag{2.36}$$

G is a geometric factor related to the device's transversal resistance and can be measured directly in the devices. λ_{eff} is an efficiency factor given by the material properties. When the spin resistance of the SOM ($\lambda_s^{SOM}\rho_{SOM}$) is much larger than that of the FM ($\lambda_s^{FM}\rho_{FM}^*$), the spin current injected into the SOM is reduced, an effect known as "conductivity mismatch" [125], greatly reducing the effective factor (see Eq. 2.36). The addition of a tunnel barrier between the FM and the SOM can be used to overcome the conductivity mismatch by reducing the spin backflow and, thus inject effectively more spin current into the SOM [126]. The quantification performed on the local spin Hall devices can be directly compared to the nonlocal spin Hall devices. Both techniques extract the spin Hall properties due to the SCI. Whereas $2\Delta R_{(I)SHE}$ is easier to measure in the local spin Hall devices because the spin injection is local and the output voltage is higher compared to the nonlocal spin Hall devices, the local device can contain spurious effects in the spin Hall signal, coming from the AHE or the planar Hall effect (PHE) of the FM, or from the combination of the ordinary Hall effect (OHE) of the SOM with the fringe fields of the FM at saturation as discussed in Refs. [34, 127].

2.3.3 Spin pumping

Exploring the physics of SCI involves both the creation of spin currents and the detection of charge currents. For instance, in the nonlocal transport schemes shown

in section 2.3.1, this is achieved by spin diffusion into the SOM. An alternative to generating spin currents is to exploit the spin-pumping (SP) effect in a FM/SOM bilayer system. This phenomenon was observed experimentally in the early 2000s [128–130].

The SP technique uses the magnetization dynamics of a FM material [131, 132] in order to study and quantify the SCI of an adjacent SOM layer. The schematic representation of this effect is shown in Fig. 2.11a. A radio frequency (RF) current with a fixed frequency (f) of the order of GHz is injected into a coplanar waveguide (CPW) generating an RF magnetic field on the sample (h_{RF}) that produces the precession of the magnetization (M) in the FM layer. The direct current (DC) magnetic field (H_{DC}) is applied along y-direction (in-plane). At certain combinations of H_{DC} and f, a ferromagnetic resonance (FMR) occurs in the FM and, by the spin-pumping effect, this precession induces an injection of DC spin current (I_s) into the adjacent SOM (along the $-z$ direction). In the SOM layer, due to the ISHE (or the IREE), a charge current, I_{SP}, perpendicular to the spin current, leads to charge accumulation and thus to a measurable voltage (V_{SP}) along the x-direction [98, 132, 133]. V_{SP} can be measured by modulating the RF power injected in the CPW and using a lock-in voltmeter that is matched to this modulation while sweeping the external H_{DC}. When the system reaches the resonant condition, the measured voltage exhibits a characteristic Lorentzian curve symmetric around the resonance field (H_r) as shown in Fig. 2.11b. V_{SP} should also be perfectly reversed with inversion of field direction (*i.e.* rotating it by 180°). Since $j_c \perp s$ in both ISHE and IREE, flipping the spin polarization s of the spin current that is pumped into the SOM leads to a generation of a current in the opposite direction. The voltage produced by the ISHE or IREE is always symmetric with H_r. An antisymmetric part is usually dominant in FM films, as observed for example in CoFeB [134] and NiFe [107], whereas it is negligible in the measurements in this thesis, and we consider only the symmetric part in the fit.

When H_{DC} and h_{RF} are applied in the film's plane (and $H_{DC} \times h_{RF} = 0$), the dispersion relation of H_r with angular frequency $\omega = 2\pi f$ follows Kittel's relation [134]:

$$f = \frac{\gamma}{2\pi}\sqrt{(H_r + H_{uni})(H_r + H_{uni} + M_{eff})}, \tag{2.37}$$

where $\gamma = g\mu_B/\hbar > 0$ is the gyromagnetic ratio, which determines the direction and rate of precession of the magnetization around the effective field, g is the Landé factor, which quantifies the ratio between orbital and spin angular momenta and is approximately 2 for free electrons, and μ_B is the Bohr magneton.

M_{eff} is the effective magnetization and H_{uni} is a small in-plane uniaxial magnetic anisotropy. V_{SP} is given by the sum of symmetric and antisymmetric Lorentzian functions:

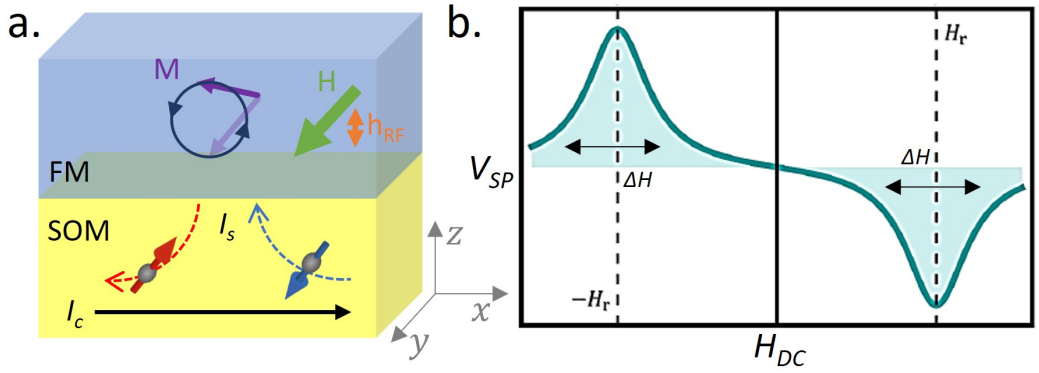

Figure 2.11: Spin pumping devices. Schematic representation of a spin-pumping device. **a.** In this case, a DC field (H_{DC}) is applied in-plane perpendicular to the sample while a RF electric current is injected in the CPW, producing an RF magnetic field (h_{RF}) that generated the precession of the magnetization, M, in the FM layer. This creates a spin current, I_s, in the out-of-plane direction ($-z$), and is injected in the SOM and converted into a voltage, $V_{SP} = V^+ - V^-$ due to the ISHE or IREE, **b.** Schematic spectra of a typical spin-pumping voltage, V_{SP} as function of the applied field H.

$$V_{SP} = V_{offset} + V_{sym}\frac{\Delta H^2}{\Delta H^2 + (H_{DC} - H_r)^2} + V_{antisym}\frac{\Delta H(H_{DC} - H_r)}{\Delta H^2 + (H_{DC} - H_r)^2}. \tag{2.38}$$

where ΔH is the width of the peak at the center of H_r. The most common description of magnetization dynamics including relaxation is based on the Landau-Lifshitz-Gilbert equation [135], which includes the Gilbert damping (α), the dimensionless parameter that describes how fast the magnetization become aligned with the effective magnetic field. α can be obtained by considering the linear dependence of ΔH on frequency as:

$$\Delta H = \Delta H_0 + \alpha\frac{2\pi f}{\gamma}, \tag{2.39}$$

where ΔH_0 is the frequency-independent inhomogeneous contribution. The spin transparency of the interface between the FM and SOM layers is given by the real

part of the effective spin-mixing conductance, $g_{\uparrow\downarrow}$, which can be obtained by the following equation:

$$g_{\uparrow\downarrow} = \frac{4\pi M_s t_{FM}}{g\mu_B}(\alpha_{FM/SOM} - \alpha_{FM}), \tag{2.40}$$

where M_s is the saturation magnetization and t_{FM} is the thickness of the FM layer. $\alpha_{FM/SOM}$ and α_{FM} correspond to the Gilbert damping of the FM/SOM bilayer and a reference FM layer, respectively.

The detection of the spin current flowing into the SOM can be done electrically via the ISHE, as was demonstrated by Saitoh *et al.* [136]. The ISHE converts the pure spin current into a detectable charge current (see Eq. 2.22), allowing us to infer the spin Hall angle of the material.

For the detection of a DC voltage along the y-direction (V_{SP}), one has to consider the charge current density [137]:

$$j_{\mathrm{SP}} = \theta_{SH}\frac{2e}{\hbar}j_{s,0}\frac{\lambda_s^{SOM}}{t_{SOM}}tanh\left(\frac{t_{SOM}}{2\lambda_s^{SOM}}\right), \tag{2.41}$$

where $j_{s,0}$ is the spin current crossing the interface. To convert this charge current density into the actual measured voltage, the details of the measurement geometry (t_{SOM} is the SOM thickness) and the resistivity of the bilayer need to be taken into account. Besides that, the spin current generated at the interface which propagates into the SOM decays on a length scale connected to λ_s^{SOM} [137]. Note that, in systems with strong SOC, this length scale can be difficult to define since it can be as short as several atomic layers. Also, proximity effects as well as roughness at the interface with the SOM can blur the sharpness of such an interface [86].

The spin pumping technique has several advantages that make it a very interesting technique. The most attractive is the geometry of the device, as only a FM/SOM bilayer is required for the detection of SCI and no complex fabrication is required. In addition, this technique allows the generation of spin currents over large areas and therefore large voltages can be detected. Also, since the spin injection is achieved by the magnetization dynamics, the conductivity mismatch problem discused in section 2.3.2 can be avoided. Another big advantage of this technique is that FM insulators can be used to pump spin currents [51, 138, 139], with the plus that the

detected charge current can only have its origin in the SCI of the SOM layer, since electrical conduction along the FM insulator is prevented. On the other hand, a major drawback is the magnetic proximity effect that could occur due to the proximity of the non-magnetic SOM layer to the FM layer. This magnetic proximity could generate additional damping to the magnetization dynamics [140, 141].

2.3.4 Other techniques to measure the SCI

Several methods have been developed over the years to measure the spin currents originating from the SHE or the REE, and each one has its own complexity. Other commonly used measurement techniques are briefly mentioned in this section.

Magneto-optical Kerr effect (MOKE): The experimental discovery of the SHE initially was focused on semiconductors and was suggested to utilize the optical activity of these materials for detecting the SHE [142]. Murakami, Nagaosa, and Zhang in 2003 proposed a circularly polarized electroluminescence or a spatially resolved magneto-optical Faraday and Kerr effects. These methods were indeed used in the first measurements of this phenomenon. The first experimental observation of the SHE was in semiconducting GaAs by MOKE to scan the spin accumulation across the channel, directly on a thin film of the SOM [143]. However, the magnetization associated with this spin accumulation is very small, making MOKE a very challenging technique for metals [144]. Nevertheless, spin transport parameters of a Pt thin film were recently determined by MOKE [145].

Spin-torque ferromagnetic resonance (ST-FMR): In this technique, a spin current created commonly in a SOM is used to transfer spin angular momentum and thus to exert a torque on the magnetization of a FM. In these experiments, an RF current sent along the SOM/FM bilayer can produce an oscillation of the magnetization of the FM via the perpendicular spin current generated by the SHE, the REE or the Oersted fields. Under certain conditions, the FM goes into resonance (FMR), which leads to an oscillation resistance (due to magnetoresistance effects such as AMR, GMR or TMR) resulting in a mixing of an in-phase current ($I = I_0 cos(\omega t)$) and resistance ($R = R_0 + \delta R cos(\omega t)$), which in turn results in detectable DC voltage. The ST-FMR was introduced by Tulapurkar *et al.* in 2005 [146] and the first experimental report of SOT was realized in permalloy (Py: $Fe_{20}Ni_{80}$)/Pt heterostructures in 2011 [147]. Since distinguishing between SHE and REE as the origin of the torque in these experiments is not straightforward, after some controversy the generic name "spin-orbit torque" started to be used.

Harmonic Hall measurements: The harmonic Hall voltage measurement method is a useful approach for quantifying the effective fields induced by the SOT [148] which generate a damping-like torque (T_{DL}) and a field-like torque (T_{FL}) [149]. For this method, SOM/FM bilayers are patterned into Hall-bar structures and alternating current (AC) currents $I(t) = I_0 \sin(\omega t)$ are driven through the main channel. The current-induced effective fields lead to a modulation of the magnetization orientation in phase with the driving current which can be picked up via the PHE and the AHE. As a consequence of the frequency mixing, the resulting Hall voltage has first ($V_H^{1\omega}$) and second ($V_H^{2\omega}$) harmonic components which can be measured by Fourier transformation of a time series or, more commonly, by a lock-in amplifier. The $V_H^{1\omega}$ contains the AHE and PHE properties of the SOM/FM heterostructure, whereas the SOT information is included in the $V_H^{2\omega}$ component, because of the frequency mixing of the in-phase modulation magnetization induced by SOT and the AC current. This method is particularly suitable for identifying the angular dependence of the SOT that acts on the FM layer with perpendicular magnetization. Several corrections are required for an accurate analysis of the measured results with this technique, including the measured results for the PHE, the out-of-plane component of the external magnetic field, and the AHE [150]. In the harmonic Hall voltage measurement, $V_H^{2\omega}$ consists of the anomalous Hall voltage (V_{AHE}), and the planar Hall voltage (V_{PHE}), that couples with the effective fields of T_{DL} and T_{FL} [151]. The product of the magnetization of the FM layer and the effective field of SOT is equivalent to the spin current converted from the charge current, thus this technique is widely used as one of the methods for estimating SCI efficiency [39, 152, 153].

Chapter 3

Experimental techniques

3.1 Fabrication processes for nanodevices

3

In this chapter, we describe and give a general overview of the techniques used to fabricate and characterize our devices. As described in Chapter 2, we have different types of devices throughout this thesis: nonlocal spin Hall devices, local spin Hall devices, and SOM/FM bilayers for spin pumping. Although they share a common fabrication process, the details for each device are different. Therefore, the fabrication and characterization features for each type of device are provided in their respective chapters, and the general steps are explained here.

In general, the nanodevices used in this thesis are basically several electrodes of different materials (NM, FM or SOM) connected in a specific geometry for electrical measurements. Each electrode structure is fabricated by a polymer mask (sensitive to e-beam or UV light) that defines the areas of the electrodes prior to the deposition of the desired material.

The fabrication consists of several steps that are carefully performed to have a successful device. The first step is the cleaning of the substrate, which is usually Si/SiO_2 with a SiO_2 thermally oxidized with a thickness of 150 nm or 300 nm (Fig. 3.1a). This is an important step for the following processes to work.

Next, a lithography process is performed, starting with the spin coating of a polymeric positive resist, single or double layer (see Fig. 3.1b), followed by e-beam exposure of the desired pattern (Fig. 3.1c) and development to remove the e-beam exposed resist (Fig. 3.1d). This is followed by an ion milling process with Ar^+ ions to remove any residual resist and to clean the interfaces (Fig. 3.1e). Immediately after the milling process, the material is deposited by sputtering, e-beam evaporation or thermal evaporation (Fig. 3.1f).

Finally, the remaining resist is removed during the lift-off process (Fig. 3.1g). In spite of using a double layer for the resist, it is possible that some material is still stuck on the walls. In order to remove these side walls, we performed an ion milling process with a lower angle of incidence (10° with respect to the sample plane) (see Fig. 3.1h).

Figure 3.1i shows the nanostructure with the desired shape. This process is repeated as many times as necessary to fabricate the final nanodevices according to the device design. In the following, each step of the fabrication process is explained in detail.

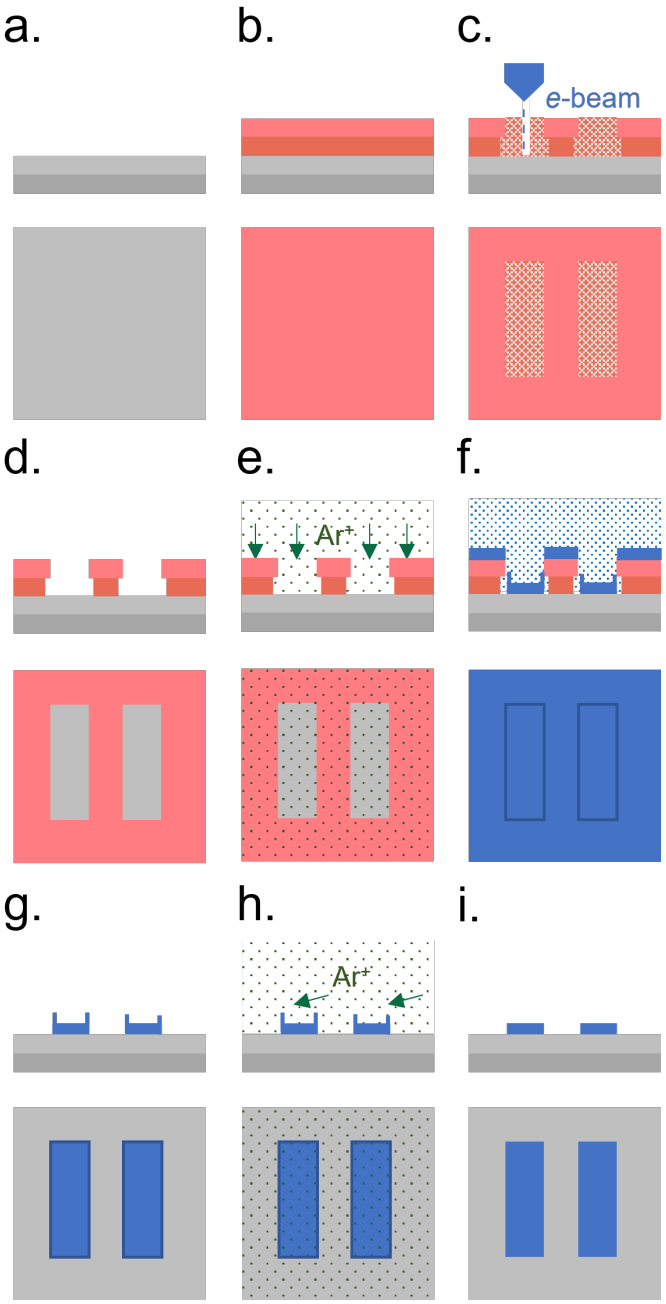

Figure 3.1: Main steps for the fabrication process of nanostructures using a positive resist. Schematic representation for the fabrication process of nanostructures, each sketch shows the top and side view of each step. **a.** The first step in the fabrication of nanodevices is the cleaning of the Si/SiO_2 substrates (represented in grey). **b.** Spin coating of e-beam positive resists. The sketch presents the double layer spin coating, in dark pink the resist with lower molecular weight. **c.** e-beam exposure of the desired pattern. **d.** Development of the exposed area. **e.** Ar-ion milling for removing resist left-overs and/or cleaning interfaces. **f.** Material deposition (in blue). **g.** Lift-off. **h.** Ar-ion milling with low angle of incidence for side-walls removal. **i.** Final nanostructure with the desired shape.

3.1.1 Cleaning of the substrates

The first step of the fabrication process is the cleaning of the substrate, see Fig. 3.1a. In this thesis, we used Si/SiO_2 wafers with a SiO_2 thickness of 150 nm or 300 nm with Si substrate doped with boron (p-type). The wafers were cut into small pieces of 10 mm $\times 10$ mm or 5 mm $\times 5$ mm area. The chips were then sonicated for 5 minutes in acetone, followed by another 5 minutes of immersion and sonication in isopropanol. Finally, we sonicated the substrate for another 5 minutes in deionized water, dried it with N_2 gas, and placed it in a hot plate at temperatures above $100°$ C to evaporate any remaining water.

3.1.2 E-beam lithography

Spin coating

The first step of the electron-beam lithography (eBL) process is spin coating. An electron-sensitive polymeric resist is placed on top of the cleaned substrate and is spinned with controlled acceleration and velocity [154]. In this work, we used positive e-beam resists. With the polymeric positive resist, the chemical bonds of the polymer are broken in the areas exposed to the e-beam. This way, the exposed area could be more easily dissolved in the presence of a specific solvent, leaving a hole in that area that will act as a temporary mask for our process.

We select the resist to be used in accordance with the material deposition method and the final thickness of the deposited material. In this thesis, we used a double layer of positive resists Polymethyl Methacrylate (PMMA), with different molecular weights. Both PMMA A4 495 and PMMA A2 950 resists were spin-coated at 4000 rpm for 60 s and baked to evaporate the anisole solvent at $180°$C for 90 s, each layer (Fig. 3.1b). The A4 and A2 represent the molecular concentration (4% and 2%, respectively) dissolved in anisole. The numbers 495 and 950 represent the molecular weight (in k g/mol units).

In double-layer spin coating, the polymer resist with the lower molecular weight is used at the bottom. During the e-beam exposure, more polymer chains are broken than those in the top layer (higher molecular weight). As a result, an undercut is created (see Fig. 3.1c), which allows us to lift off the resist more efficiently. The higher the molecular weight, the less sensitive to the e-beam. The higher the molecular concentration, the thicker the resist (layer thickness is $\sim$ 50 nm for PMMA A4 495 and ~ 150 nm for PMMA A2 950).

In addition, in this thesis, we used another e-sensitive polymeric resist, a copolymer of α-chloromethacrylate and α-methylstyrene (ZEP). The spin coating for ZEP resist is performed at 4000 rpm for 60 s and baked to evaporate the anisole solvent at 180°C for 300 s. This resist is more sensitive and with higher etch durability than PMMA and, due to its thickness (~ 2 μm), it is also useful for processes with significant heating during material deposition.

e-beam exposure

After spin coating, the e-sensitive polymeric resist film is exposed to a highly focused e-beam to create a pattern. The eBL systems available at CIC nanoGUNE BRTA facilities are the *Raith* 150^{two} and the *Raith* e-line^{+}, both used in the fabrication processes of this thesis. The design of the pattern is previously created in the software provided by the same company. The main parameters to consider with this technique are the acceleration voltage, which determines the energy of the electrons reaching the stage where the sample is placed, and the aperture of the beam, which with the acceleration voltage determines the current of the e-beam. The write field, another important parameter, is the area that is exposed just by deflecting the e-beam (when the stage is fixed). The smaller the write field, the better the resolution (about 10 nm). The write field also allows us to perform alignment procedures if the device requires multiple lithography steps. Finally, the dose determines the amount of charge per unit area that reaches the sample. These parameters depend on the polymeric resist used and the resolution we want to achieve.

Developing

After the e-beam exposure, the sample is immersed in a special solvent to dissolve the areas of broken polymer bonds in the resist exposed by the e-beam. The pattern now appears as a hole in the resist film, which acts as a temporary mask. We used a mixture of methyl isobutyl ketone and isopropyl alcohol [MIBK:IPA (1:3)] as the developer for PMMA, immersing and shaking the sample for 60 s. For ZEP resist, the developer is N-methyl-2-pyrrolidone (NMP). The development is performed by immersing the sample in this solvent and at the same time shaking it for 30 s, and then rinsing it with isopropanol and drying it with N_2. If possible, it can be checked under a light microscope to confirm the correct pattern and development process.

3.1.3 Ar-ion milling

Ar-ion milling is a physical process for surface cleaning or etching a material on a substrate. Ions of an inert gas such as Ar are accelerated from an ion-beam source perpendicular to the sample (Fig. 3.1e). The Ar^+ ions collide with high energy, etching the material from the sample surface. Ar-ion milling is used in our case to clean the surface before material deposition and also, in the devices, to improve the electrical contact between the electrodes by removing possible oxide layers or residues from the polymeric resist in the lithography process. The relevant parameters are the acceleration voltage (in this work we use 50 V), the beam current (50 mA), and the beam voltage (300 V). The Ar gas flux we used was 15 s.c.c.m. and the rotation of the sample to ensure uniform milling was set to 15 rpm.

It is important to previously calibrate the milling rate (process time) for the materials of interest to obtain an accurate and reproducible result between samples. In this work, we use a 4-*wave* ion-beam miller with high vacuum and an *in-situ* endpoint detector spectrometer from *Hiden Analytical* together with the *MASsoft professional* software using the multiple ion detection (MID) mode of the desired elements (individual masses). Figure 3.2 shows the mass detection of Bi and Se from a BiSe thin film after removal of the capping layer of SiO_2.

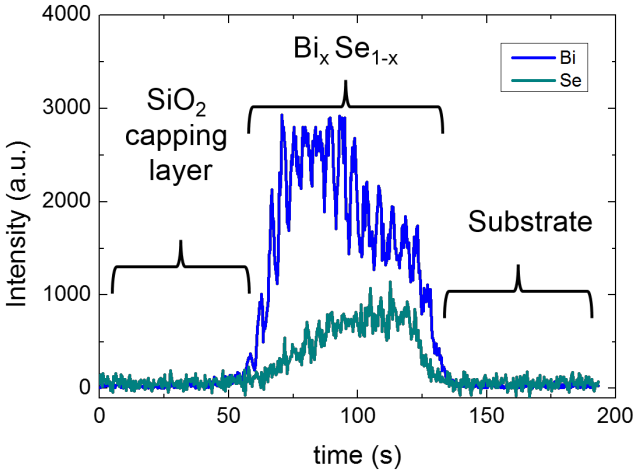

Figure 3.2: Endpoint detection spectra. Intensity as a function of milling time for Bi (blue curve) and Se (dark cyan curve) in a BiSe/SiO_2 bilayer. SiO_2 acts as a capping layer. When this layer is completely milled, the 30-nm-thick BiSe layer is detected, until the substrate is reached.

3.1.4 Material deposition and lift-off

In this thesis, the material deposition was performed by physical vapor deposition (PVD) techniques. PVD includes a variety of vacuum deposition methods to grow thin films characterized by a material that goes from condensed phase to vapor phase and then is deposited on the substrate in condensed phase as a thin film. The PVD methods used in this work are shown in Fig. 3.3 and will be explained below.

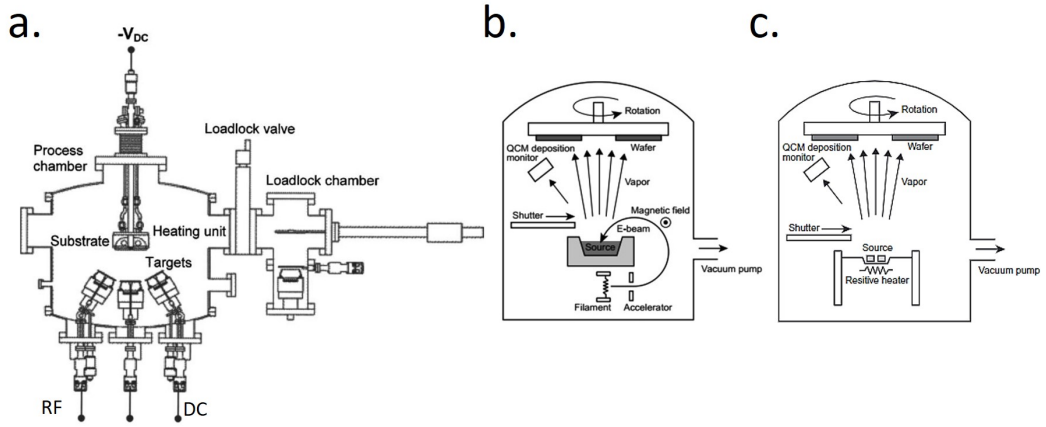

Figure 3.3: Physical Vapor Deposition techniques. Schematic representation of **a.** magnetron sputtering, **b.** e-beam evaporation, and **c.** thermal evaporation. Figures adapted from Refs. [155, 156].

Magnetron sputtering

This technique consists of bombarding a target (bulk material to be sputtered) with energetic particles such as Ar^+ ions [157]. To do this, the chamber, which is at ultra high vacuum (UHV) pressure ($\sim 10^{-8}$ mbar), is first saturated with Ar gas. This inert Ar gas is ionized with a high-energy discharge, generating a plasma. The plasma contains inert Ar and argon ions (Ar^+). The Ar^+ are then accelerated to bombard the target with an energy higher than the binding energy of the target atoms. The sputtered atoms are extracted as a vapor source with neutral particles (single atoms or clusters of atoms) that will travel until they reach some surfaces for thin film deposition, such as the substrate surface. This technique is used for the deposition of both metals and insulating materials. In this work, we used a UHV magnetron sputtering system from AJA International containing seven targets.

The configuration of the target guns of the sputtering system used in this thesis is similar to the sketch in Fig. 3.3a, where the targets are not unidirectional to the

substrate. As a consequence, for narrow structures, the spin-coated polymeric resist used for the lithography process creates a shadow effect. This means that the nominal thickness we have calibrated for a thin film will be reduced as a function of the width of the pattern electrode, as shown in Fig. 3.4. This is important to keep in mind in order to achieve the desired thickness in our devices.

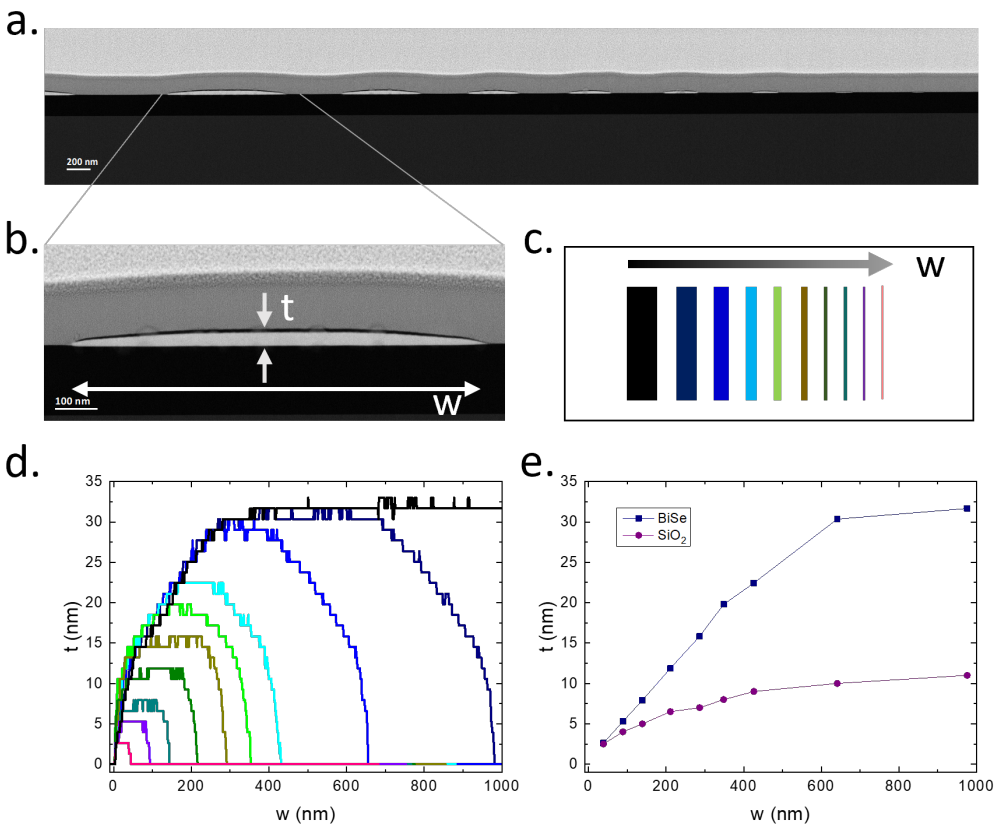

Figure 3.4: Thickness dependance of the width of the electrodes in sputter deposition. The nominal thickness of the nanostructured electrodes decreases with the width of the patterned electrodes due to the shadow effect of sputter deposition. **a.** Transmission electron microscopy (TEM) image presenting the lateral view of nine sputtered BiSe/SiO_2 electrodes with different widths ($50 - 1000$ nm). The electrodes were fabricated using a double layer PMMA resist. **b.** Zoom of one sputtered BiSe/SiO_2 bilayer electrode showing the thickness, t, and width, w. **c.** Schematic representation for the nanostructured electrodes. The black arrow represents the reduction of the width. **d.** Final profile of the thickness as a function of the width of the electrodes. The black curve represents the wider electrode that has the same thickness as the thin film. The pink curve represents the narrowest electrode (45 nm wide) with a significant thickness reduction. Each of the colored curves correspond to the colors shown in c. **e.** Thickness of the individual layers (on the same bilayer), BiSe and SiO_2, as a function of the width.

e-beam evaporation

Evaporation by e-beam [158] consists of a crucible filled with pellets of the desired material, then electrons are emitted thermionically by applying a current to a W filament and accelerated into the crucible by electric and magnetic fields under high vacuum, see Fig. 3.3b. The e-beam that reaches the pellets of the material has high energy to vaporize it and create a gaseous phase. These atoms will precipitate into a solid phase that coats the substrate. In this thesis, we used two e-beam systems, a HV system from the Kurt J. Lesker Company (base pressure of $\sim 10^{-7}$ mbar) and a UHV evaporation system from CreaTec (base pressure of $\sim 10^{-9}$ mbar). This technique is used for the deposition of metallic materials (including FM materials).

Thermal evaporation

Thermal evaporation, also known as Joule heating evaporation, consists of heating the crucible or source of the desired material with electrical currents based on the Joule effect (Fig. 3.3c). By applying high-density currents to the thermal crucible in vacuum, the material on the crucible is heated by heat transfer, and the atoms of the material are vaporized and finally deposited on the substrate [159]. In this thesis, we used the HV system from the Kurt J. Lesker Company for Au deposition and the UHV evaporation system from CreaTec for Cu deposition.

Lift off

The lift-off process depends on several aspects such as the e-sensitive polymeric resist used and the material deposition. After material deposition, the chips patterned with single or double layer PMMA are immersed in acetone. The sample is removed from the acetone when all the resist has lifted off. If necessary (in case of metal deposition), it is also possible to sonicate at low power for 30 s. In the case of the ZEP resist, the sample is immersed in NMP for 10 min and sonicated for 30 s. Finally, for both resists, the sample is examined by optical microscopy and, if the resist has lifted off, rinsed with isopropanol and dried with N_2 gas.

3.1.5 Mechanical exfoliation of graphene

An alternative for the fabrication of LSVs is to use graphene as a spin transport channel [114, 160–162], which we will explain in Chapter 7. For the spin transport channel, we need a narrow and long graphene flake, which is obtained by mechanical exfoliation of a highly-oriented pyrolytic graphite (HOPG).

The graphite structure has weak van der Waals bonds between the layers of the material, compared to the covalent bonds between the carbon atoms within a layer, which allows us to separate the layers using only a tape (Nitto SPV 224P [163]). We peel off HOPG several times until we get the desired amount of material to transfer the flakes onto a $Si/SiO_2(300\ nm)$ substrate by pressing the tape against the substrate. The substrate was previously heated to 120°C. After transfer, we scanned the substrate with the flakes with an optical microscope, and by optical contrast we could select the flake with the desired thickness and shape for the LSV. This method is also known as the Scotch tape technique [164, 165].

3.2 Characterization techniques

Material characterization was performed on the thin films, as well as on the different nanostructured devices. In this section, we explain the electrical characterization using different temperatures and applying external magnetic fields in a specific setup. Magnetotransport measurements are one of the most important parts for the purpose of this thesis, in order to extract the spin transport properties of BiSe. In addition, we have used different microscopy techniques and X-ray characterization to calibrate the deposition rates, extract the dimension of the electrodes in the nanodevices, and know the structural and compositional quality of the nanostructures and interfaces.

3.2.1 Electrical characterization

The electrical characterization related to Chapters 5, 6 and 7 is performed at the physical property measurement system (PPMS) by Quantum Design Inc. Electrical, thermal, and magnetic properties measurements could be performed in PPMS systems operating at temperatures down to 1.8 K with a superconducting magnet immersed in liquid helium at the bottom of the system, which allows us to perform magnetotransport measurements in the range of ± 9 T.

The system includes an all-metal cryostat with vacuum insulation and intermediate temperature radiation shielding in the form of cryogenic fluids such as nitrogen and helium. The equipment available at CIC nanoGUNE BRTA includes a helium recovery system so that the helium gas lost from the boiling helium liquid can be reliquefied and reused.

We introduce the sample inside the cryostat with a stick, in a vacuum space inserted in the helium-cooled superconductive magnet. In this work, we used a stick with a rotating stage that allows us to change the angular position of the sample to study the magnetotransport properties at different magnetic field directions. For the measurement, we mounted the sample in a chip carrier (puck) with eight electrical contacts that fit into the rotating stick. The electrical connection between the sample and the puck is made by Al wires using a *West Bond* wire bonder. The bonds with the wire bonder can be made on pads as small as $100\ \mu$m $\times$ $100\ \mu$m, allowing multiple devices to be fabricated on the same substrate.

For the transport measurements, we used a *Keithley 2182A* nanovoltmeter, a *Keithley 6221* current source, and a switchboard. The switchboard allows us to select the contacts or channels in which we want to apply current (using the *Keithley 6221*) or to probe the voltage (with the *Keithley 2182A* nanovoltmeter [166]). We use a "delta mode" technique for measurement (also known as the DC reversal technique). In a delta mode, positive and negative currents are applied alternately, and the voltage is measured each time the polarity of the current changes. The voltage read by the delta configuration is given by:

$$V = \frac{V(+I) - V(-I)}{2}, \tag{3.1}$$

where $V(+I)$ and $V(-I)$ are the voltages for the positive and negative charge currents, respectively. This mode keeps the voltage which has a linear response with the applied current, while removing the thermoelectric effect and baseline drift, which reduces the noise [167]. Therefore, it is adequate for low-resistance measurements. The delta mode is equivalent to the 1st harmonic signal of an AC lock-in measurement.

3.2.2 Microscopy techniques

To better understand the devices in terms of dimensions, surfaces, and interfaces, we used various microscopy techniques such as optical, electron, and atomic force microscopies. Electron microscopy allows us to obtain high-resolution images by "illuminating" the sample, but instead of using a light beam, we used a focused electron beam. These electrons are accelerated and have high energy that interacts with the sample. The electrons could be reflected, deflected, or transmitted

across the sample, giving us valuable information. In this thesis, we use the following microscopes:

Optical microscopy

Optical microscopy, also known as light microscopy, is the "classical" microscopy that uses visible light and a system of multiple lenses to produce magnified images of small objects. In this thesis, we used microscopes from *Nikon Instruments Inc.* to control the process during the different fabrication steps (lithography pattern, development, and lift-off) and also to scan the exfoliated HOPG on a Si/SiO_2 substrate to find the desired flake for further device fabrication.

Scanning electron microscopy (SEM)

SEM can detect the reflected emission of low energy secondary electrons and high energy backscattered electrons, probing the topography and composition of the sample surface, respectively [168]. In this thesis, SEM is used to take images of the devices with a resolution of several nanometers. These images are used for the alignment of the nanostructured devices during the lithography process and to measure the dimensions (width and length) of the devices. The SEM images presented in this thesis have been obtained with the eBL systems *Raith 150^{two}* and *Raith e-line^{+}*.

Transmission electron microscopy (TEM)

TEM is a high-resolution imaging technique that can detect electrons that have passed through a sample (i.e. electrons transmitted). TEM gives us information about the crystal structure, possible defects, impurities, and composition when combined with the energy-dispersive X-ray (EDX) spectroscopy. An important requirement for this technique is the small size of the samples. Samples must be $\sim$ 100 nm thick, flat, and the preparation technique should not alter the crystallographic structure or introduce any artifacts on it [169]. In this thesis, TEM was used in scanning mode, also known as scanning transmission electron microscopy (STEM) mode.

In STEM, an electron gun produces a beam of electrons that is focused by a series of lenses to form an image of the electron source of a sample (also called lamella). The electron spot can be scanned across the sample in a raster pattern by exciting scanning deflection coils, and the scattered electrons are detected and their intensity plotted as a function of probe position to form an image [170]. The scanning of the beam over the sample makes STEM suitable for analytical techniques such as

EDX spectroscopy. These signals can be acquired simultaneously, allowing a direct correlation of images and spectroscopic data. Unlike SEM, which typically uses a bulk sample, STEM requires a thinned and electron-transparent sample.

The preparation of (S)TEM samples is specific to the material to be analyzed and the type of information to be obtained from the sample. In this thesis, the preparation of the lamella is carried out through a cross-section of the tested devices by a standard focused ion beam (FIB). A FIB combined with a TEM provides the ability to reveal and image the internal structure of materials [171, 172]. During the process, the lamella needs to be protected, and this is done by ion-beam-induced Pt deposition. Then, the lamella is cut and lifted on a specific grid.

The STEM images were obtained by Prof. Andrey Chuvilin at CIC nanoGUNE BRTA using a *Titan 60-300* electron microscope (*FEI Co.*) equipped with EDX detector (*Ametek Inc.*). The EDX spectral images were obtained using an EDAX RTEM spectrometer. Element distribution maps were obtained by multiple linear deconvolutions of spectral images using simulated spectral components. This analysis plays an important contribution to the better understanding of the interfaces in our devices.

Atomic force microscopy (AFM)

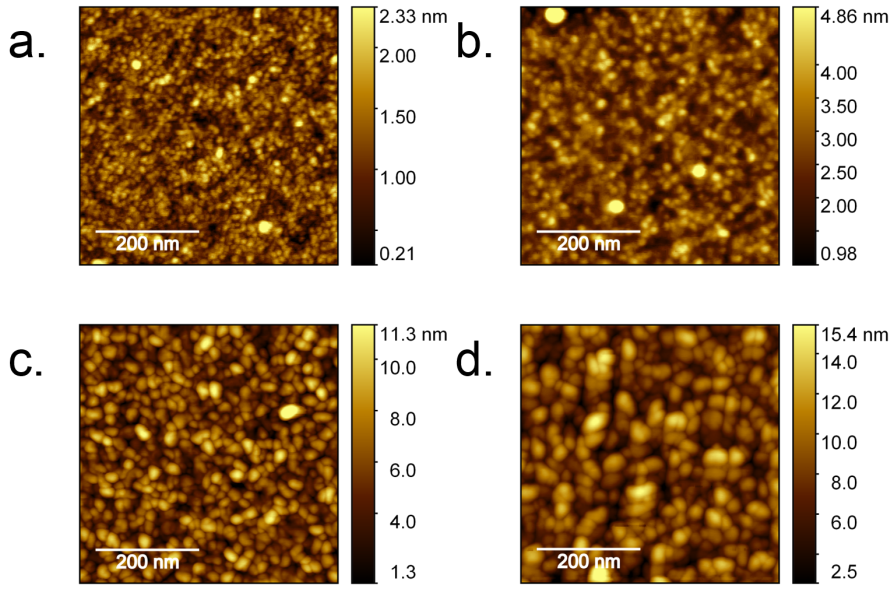

Figure 3.5: Atomic force microscopy images. AFM surface images of 500 nm × 500 nm for BiSe thin films with **a.** 10 nm [$RMS = (0.34 \pm 0.05)$nm], **b.** 30 nm [$RMS = (0.50 \pm 0.05)$nm], **c.** 60 nm [$RMS = (1.4 \pm 0.1)$nm], and **d.** 120 nm [$RMS = (2.2 \pm 0.2)$nm] thickness.

AFM is a type of scanning probe microscopy that consists of a sharp tip attached to a cantilever that deflects due to the atomic interaction between the surface of the sample and the tip. An incident laser on the cantilever changes the reflection accordingly and is detected by a photodetector [173]. In this thesis, we used a AFM instrument from *Agilent Technologies* to first characterize the surface quality of the samples, such as the roughness [Root Mean Square (RMS)] and grain size of our BiSe thin films, as shown in Fig. 3.5.

3.2.3 X-ray characterization

X-ray characterization is the use of high-energy electromagnetic radiation to study the atomic and molecular structure of a crystal. In these techniques, X-rays are directed at a sample to extract various information such as crystallographic structure or thin film thickness. The X-rays that penetrate the crystal interact with its periodic atomic structure and reflect a portion of the radiation. Figure 3.6a. shows the diffraction process on a crystal lattice. Constructive and destructive interference produces a diffraction pattern that contains information about the crystal structure. The angles for coherent scattering, i.e. constructive interference, of incoming waves from a crystal lattice are given by Bragg's law [174]: $n\lambda_{\mathrm{x-ray}} = 2d\sin(\theta)$, where n is the diffraction order, $\lambda_{\mathrm{x-ray}}$ is the wavelength of the incident wave, d is the distance between the atomic planes, and θ is the scattering angle with respect to the surface plane.

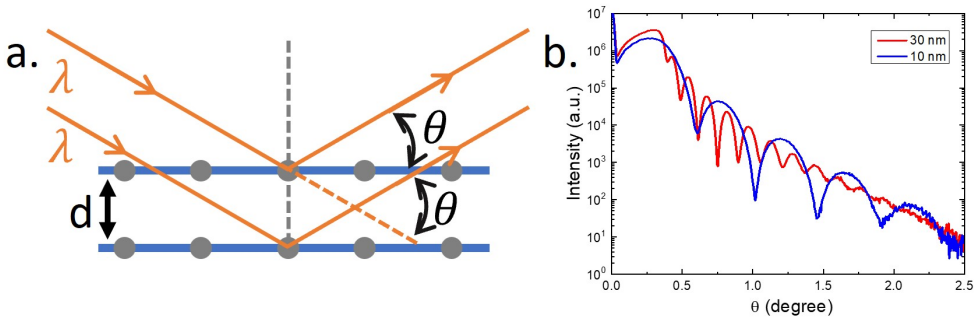

Figure 3.6: X-ray diffraction and reflectivity. a. Schematic representation of Bragg law, **b.** XRR for 30 nm (red curve) and 10 nm (blue curve) BiSe thin films.

The X-ray instrument used in this work is a $X'Pert^3$ from *Malvern PANalytical*, which was mainly used in the X-ray reflectivity (XRR) [175] configuration to quantify the thickness of the thin films, where the X-ray incident angle and the detection angle have the same grazing incidence value during the scan. The interference is

generated from the reflected X-rays at the top and bottom surface of the thin film, giving rise to the Kiessig fringes in the measured intensity, as shown in Fig. 3.6b. The periodicity of the fringes is used to determine the thickness of the thin film. The thinner the film, the wider the fringes.

3.3 Finite Element Method

Numerical simulation methods are performed after Finite element method (FEM) analysis to solve partial differential equations in 2D or 3D structures. FEM simulation analysis consists in dividing a large element into small parts, making it simpler finite elements connected by nodes. By doing the simulation it is possible to solve the physical problems for each small element and the solution of the large element can be obtained by introducing some parameters or boundary conditions between the small elements.

In this thesis, several 3D FEM simulations were performed. Following the nonlocal devices explained in section 2.3.2, we extracted the interface resistances between the FM electrode and the NM channel by 3D FEM, based on the electrical measurements at the FM/NM junction. This simulation was performed with *COMSOL Multiphysics*, a commercial software. The interface resistance is the electrical contact resistance at the junction of two electrodes and is an important parameter to extract carefully due to its influence on the spin current flows in our devices, subsequently in the quantification of the spin diffusion length and the SCI efficiency of the SOM.

Additionally, 3D FEM simulations on spin transport were performed following the drift-diffusion model in section 2.1.3 by constructing the most similar geometry possible (volume and surfaces such as thickness and width) and doing the 3D mesh using a free software *GMSH* [176], then we set the known physical properties for the physical volume and surface, such as resistivities, spin diffusion lengths, spin polarizations of the FMs. The script that we used in this thesis to set the physical properties was written by Dr. V.T. Pham using Python language.

Afterward, we used the corresponding solver *GETDP* [177–181], which allows us to perform calculations, post-processing, and data flow control of the simulations. This solver uses a script that defines the physical interaction in terms of spin and charge. It first associates the previously indexed physical volume and surfaces, and then defines the current source and spin transport properties in the function sec-

tion. The final process describes the output result, which gives us the charge or spin chemical potential in the post-operation area.

Chapter 4

Spin-to-charge conversion by spin pumping in sputtered polycrystalline BiSe

4.1 Introduction

The search for systems with more SCI efficiency is crucial for different technologies, from the new generation of MRAMs that use the direct SHE and/or REE to switch the magnetic element [182, 183] to the spin-based logic that uses the inverse effects (ISHE or IREE) to readout the magnetic element [34] as in the MESO device. In this regard, BiSe is reported as a promising candidate to be placed in the readout node of MESO. Nevertheless, this material presents problems of interdiffusion when is in contact with a FM, as discussed in section 1.3.

Such intermixing at the interface affects the material characterization because the spin currents are pumped/injected through an additional layer, leading to a poor estimation of the relevant spin transport parameters. This is the case not only for sputtered films but also when growing BiSe by techniques such as molecular beam epitaxy in ultra-high vacuum. For instance, in the growth of BiSe onto insulating ferrimagnets such as yttrium iron garnet (YIG), even though an atomically ordered BiSe layer is obtained with a thickness of a few monolayers, an amorphous layer of about 1 nm at the interface between them has been observed by several groups [57, 184]. This low-quality interface in YIG/BiSe leads to a low conversion efficiency with a λ_{IEE} of 0.1 nm, one order of magnitude smaller than for other TIs such as α-Sn [133]. Besides, theoretical predictions suggest that, if this TI is in direct contact with a metallic ferromagnet, a hybridization is produced destroying the helical spin texture or spin-momentum locking [185].

In this chapter, we made the first approach in this thesis to study the spin-to-charge current conversion in sputtered polycrystalline BiSe by using spin pumping, technique introduced in section 2.3.3. We sputtered BiSe/Py bilayers and the opposite stacking order (Py/BiSe). Our results show that θ_{SH} of BiSe has the same sign as that of Pt, in contrast with a recent study by Mendes *et al.* [186]. However, the charge current arising from the spin-to-charge conversion is lower than Pt by more than one order of magnitude. Structural characterization of the samples by TEM performed at the interfaces of the bilayers helps us to understand why sputtered thin films show this low spin conversion and how the interface and the different stoichiometries of the films could contribute to a drastic overestimation of theSCI efficiency.

4.2 Experimental details

All samples were grown on $Si/SiO_2(300\ nm)$ substrates by sputter deposition at room temperature, a technique explained in section 3.1.4. Targets of Bi_2Se_3 (99.999% pure) and Py (99.95% pure) were used in an UHV seven-target AJA sputtering system with a base pressure of 3×10^{-8} Torr. Bi_2Se_3 was RF sputtered at a 35 W power and a 3 mTorr Ar pressure to yield a deposition rate of 0.09 Å/s. The Py layers were DC sputtered at 100 W power and a 3 mTorr Ar pressure to yield a deposition rate of 0.08 Å/s. The bilayers were capped with 5 nm of Al_2O_3 (200 W RF at 3 mTorr Ar). The bilayers, including the capping, were grown *in situ*. Sample stacks are always written in this thesis from left to right corresponding from bottom to top; i.e. BiSe/Py corresponds to the BiSe being grown on top of the substrate and Py on top of BiSe, see Figs. 4.1a and 4.1b.

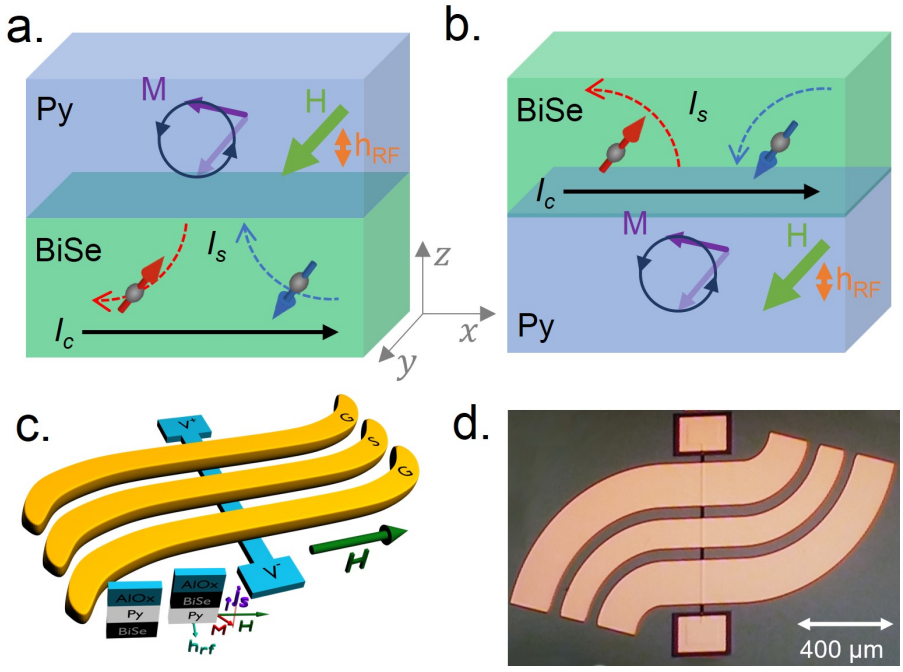

Figure 4.1: Spin pumping device. Both sketches of devices: **a.** BiSe/Py and **b.** Py/BiSe, showing the DC magnetic field (H_{DC}) that is applied in-plane perpendicular to the sample while an RF electric current is injected in the coplanar waveguide (yellow) producing an RF magnetic field (h_{RF}) that induces the precession of the magnetization (M) in the ferromagnetic layer of the sample (Py). This creates a spin current in the out-of-plane direction of the sample (j_s) that is injected in the SOM (BiSe) and converted into a voltage (V_{SP}=$V^+ - V^-$) by ISHE or IREE. **c.** Sketch of a device similar to the ones used in this chapter and **d.** its optical image.

The device fabrication and subsequent measurements were performed at Institut Jean Lamour, Université de Lorraine CNRS in France in collaboration with Dr. Juan Carlos Rojas Sánchez and Dr. Alberto Anadón. For that, the spin-pumping devices were prepared using conventional UV lithography. The full stack was first patterned and subsequently ion milled controlling the milled thickness by an ion mass spectrometer using a 4-wave IBE14L01-FA system. After that, in a second step, an insulating SiO_2 layer with a thickness of 200 nm was grown by RF sputtering using a Si target and Ar^+ and O^{2-} plasma in a Kenositec KS400HR PVD. In a third lithography step, the patterning and Au deposition for contacts and CPW were performed using a PLASSYS MEB400S evaporator. The dimensions of the active bar (see the blue part in Fig. 4.1c) are 10×600 μm. Due to the small width of the bar, we do not expect significant artifacts from rectification effects in the spin pumping signal [98, 133, 187]. The geometry of the devices, including the thickness of the insulating SiO_2, the dimensions of the CPW and the lateral dimensions of the milled samples are similar in all the devices shown in this study to reliably compare the spin pumping signal.

The spin pumping measurements were performed using a probe station with in-plane DC magnetic field (H_{DC}) up to 0.6 T provided by an electromagnet. A sketch of the SP-FMR device is shown in Fig. 4.1c. In this system, an RF current with a fixed frequency (f) of the order of GHz is injected into the CPW generating an RF magnetic field on the sample (h_{RF}).

Certain combinations of H_{DC} and the frequency of h_{RF} drive the FMR in the Py and, by the spin-pumping effect [188, 189], the precession of the magnetization produces a transverse spin current that is injected from the Py into the SOM layer (i.e. BiSe or Pt). This spin current is then converted in the SOM into a charge accumulation by means of the ISHE or the IREE. We can measure this voltage (V_{SP}) by modulating the RF power injected in the CPW and using a lock-in voltmeter that is matched to this modulation while sweeping the external H_{DC}. We use a power modulation with a sine function, where the depth was 100% and the modulation frequency was 433 Hz.

When the system reaches the resonance condition, the measured voltage exhibits a characteristic Lorentzian curve symmetric around the resonance field (H_r) (see Fig. 4.2). V_{SP} always shows in the real part of the lock-in. We always monitor both the real and imaginary parts of the voltage and never change the phase of the measurement. Any transport effects are fast enough to appear without delay in the measurement, while any other thermal effects that might be slower would show in the imaginary part (see section 4.6.1 for details on the lock-in measurements).

To obtain the effective magnetization (M_{eff}) and the Gilbert damping (α) of the ferromagnetic layer, we analyze the position of the SP-FMR resonance by observing the peak in V_{SP}. We analyze the center (H_r) and width (ΔH) of this peak as a function of frequency using the conventional method of fitting the voltage to a sum of a symmetric and an antisymmetric Lorentzian functions using Eq. 2.38. The antisymmetric part of the signal is negligible in our measurements and we consider only the symmetric part in the fit. Then, we consider the Kittel formula (Eq. 2.37).

The structural characterization by TEM was performed in CIC nanoGUNE BRTA by Prof. Andrey Chuvilin. Cross-sectional samples for the (S)TEM-EDX analysis were prepared by a standard FIB lamella preparation method: the surface of the deposited samples was protected first by e-beam followed by ion-beam-induced Pt deposition, the lamella was cut and lifted out onto a Mo 3-post half-grids. Mo grids were selected to avoid an overlap of Ni K_β line (Ni is one of the elements of interest) with Cu K_α line, which is a typical artifact in EDX spectra, if a sample is held on a Cu grid. The cross-sections were studied on a Titan 60-300 TEM (FEI, Netherlands) at 300 kV in STEM mode. EDX spectral images were acquired using EDAX RTEM spectrometer. Element distribution maps were obtained by multiple linear least-squares (MLLS) deconvolution of spectral images utilizing simulated spectral components.

4.3 Results

4.3.1 Spin pumping results

We performed SP measurements in the BiSe/Py and Py/BiSe samples and in a reference Py/Pt sample, shown in Fig. 4.2. In these measurements, thermal and other artifacts can be relevant and need to be accounted for [190]. In Fig. 4.2a we observe a voltage change of $2\Delta V_{therm}$ at $H_{DC} = 0$, which corresponds to the contribution from the anomalous Nernst effect and the spin Seebeck effect from the bilayer. In the case of Py/Pt, this jump is slightly smaller than the V_{SP} peak, while in the BiSe stack, it is much smaller.

Considering that the precession angle in Py is typically a few degrees [191], we can safely assume that the thermovoltages are not significant in resonance conditions. Asymmetries in the placement of the CPW structure with respect to the bar in which the sample stack is patterned could give rise to other thermal contributions to the voltage. However, since we observe a clear Lorentzian line shape in V_{SP}

and a clear sign change with the same amplitude for negative and positive applied magnetic fields, only Nernst, anomalous Nernst, or spin Seebeck induced thermovoltages caused by a change in the temperature gradient profile due to absorption of the RF power by the Py could arise [190]. Any changes in the temperature profile due to thermal transport by spin waves can be neglected due to the thin Py layer [190].

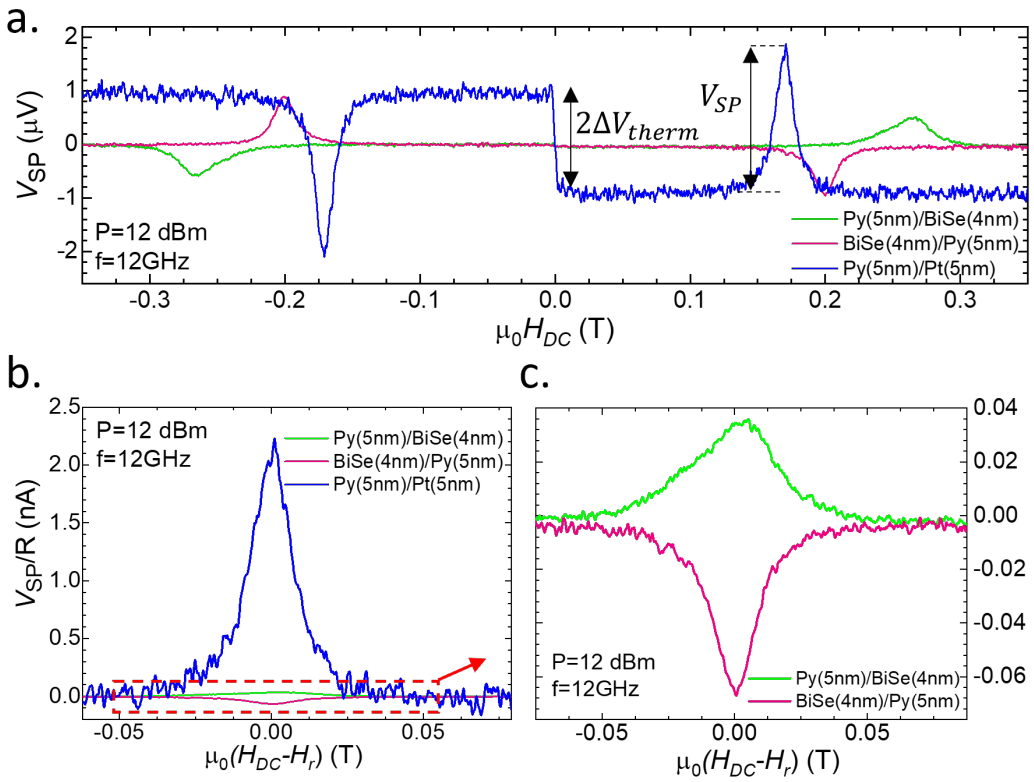

Figure 4.2: Spin pumping voltages in Py/BiSe, BiSe/Py and Py/Pt. a. Spin pumping voltage as a function of the applied DC magnetic field for the Py/BiSe, BiSe/Py and a reference Py/Pt stacks at 12 GHz and power of 12 dBm. In addition to the spin pumping voltage (V_{SP}) at the FMR condition, we can also see a jump around $H_{DC} = 0$ T due to thermovoltage (V_{therm}). This thermal voltage is much smaller in the case of the BiSe layers compared to the Py/Pt sample. **b.** Comparison of the V_{SP} of the three bilayers normalized by the sample resistance. The sign of the spin Hall angle in the Py/BiSe system is the same as the one in Py/Pt. **c.** Detail of the Py/BiSe and BiSe/Py V_{SP} from the red box in panel b.

Figure 4.2b shows V_{SP} divided by the sample two-probe resistance, i.e. the current coming from the spin-to-charge conversion in BiSe. The sign of the voltage is in agreement with a previous study [50, 51], and opposite of another report [186]. These discrepancies in reproducibility can have an interfacial origin and, thus, a careful structural analysis of the samples is needed. The magnitude of V_{SP}/R is one order of magnitud smaller than that of the reference Py/Pt layer, as shown in Fig. 4.2b. In contrast, previous results reported a very highly efficient spin-to-charge conversion, with a θ_{SH} about 200 times larger than the one of Pt [49]. Figure 4.2c shows that the sign of the SP current changes when the stack is inverted, as expected in SP measurements. Remarkably, the height and width of the peak are significantly different for both stacks, which cannot be explained if we consider the interface and sample quality similar for both samples. More specifically, the charge current produced under the same conditions, *i.e.* 12 dBm (15.85 mW) and 12 GHz, is 2.228 ± 0.003 nA for the Py/Pt stack, while only 0.040 ± 0.001 and -0.062 ± 0.001 nA for the Py/BiSe and BiSe/Py, respectively, as shown in table 4.1.

Table 4.1: Effective magnetization (M_{eff}), uniaxial in-plane magnetic anisotropy (H_{uni}), frequency-independent inhomogeneous contribution (ΔH_0), Gilbert damping (α), effective spin-mixing conductance ($g_{\uparrow\downarrow}$) and charge current generated by spin-to-charge conversion (V_{SP}/R) for Py (5 nm)/BiSe(4 nm), BiSe (4 nm)/Py (5 nm), Py (5 nm)/Pt (5 nm), and a Py (6 nm)/Au(5 nm) reference sample. For the estimation of $g_{\uparrow\downarrow}$, we are considering that all damping enhancement comes from the spin pumping effect, which is not accurate, as discussed in the main text.

Sample	M_{eff} (emu/cm^3)	H_{uni} (G)	ΔH_0 (G)	α	$g_{\uparrow\downarrow}$ (m$^{-2}\cdot 10^{19}$)	V_{SP}/R (nA)
Py/BiSe	316(3)	$-60(10)$	12(3)	0.0453(1)	3.88(1)	0.040(1)
BiSe/Py	514(1)	$-13(2)$	6(1)	0.0220(3)	2.44(1)	$-0.062(1)$
Py/Pt	701(2)	$-8(2)$	3.8(0.1)	0.0269(2)	4.43(1)	2.228(3)
Py/Au	628(1)	$-8(1)$	5.6(0.4)	0.0073(2)	-	-

In Figs. 4.3a and 4.3d, we show the frequency dependence of V_{SP} for a fixed RF power of 12 dBm. The equivalent measurements for the reference sample Py (5 nm)/Pt (5 nm) are shown in section 4.6.2. By fitting the frequency as a function of the resonance fields for both stacking orders (Figs. 4.3b and 4.3e) to Eq. 2.37, we obtain M_{eff} and H_{uni} values. α and ΔH_0 values are extracted by fitting ΔH as a function of the frequency to Eq. 2.39 (Figs. 4.3c and 4.3f). $g_{\uparrow\downarrow}$ is obtained by using Eq. 2.40. For all these fits, the Landé factor of Py (g_{Py}) has been fixed to 2.1, a value obtained independently from the reference sample (see section 4.6.2). All

the extracted values are given in table 4.1. We can observe that both the magnetic properties of the sample (M_{eff}, α) and the interfacial spin transport ones ($g_{\uparrow\downarrow}$) are significantly different between the two BiSe stacks.

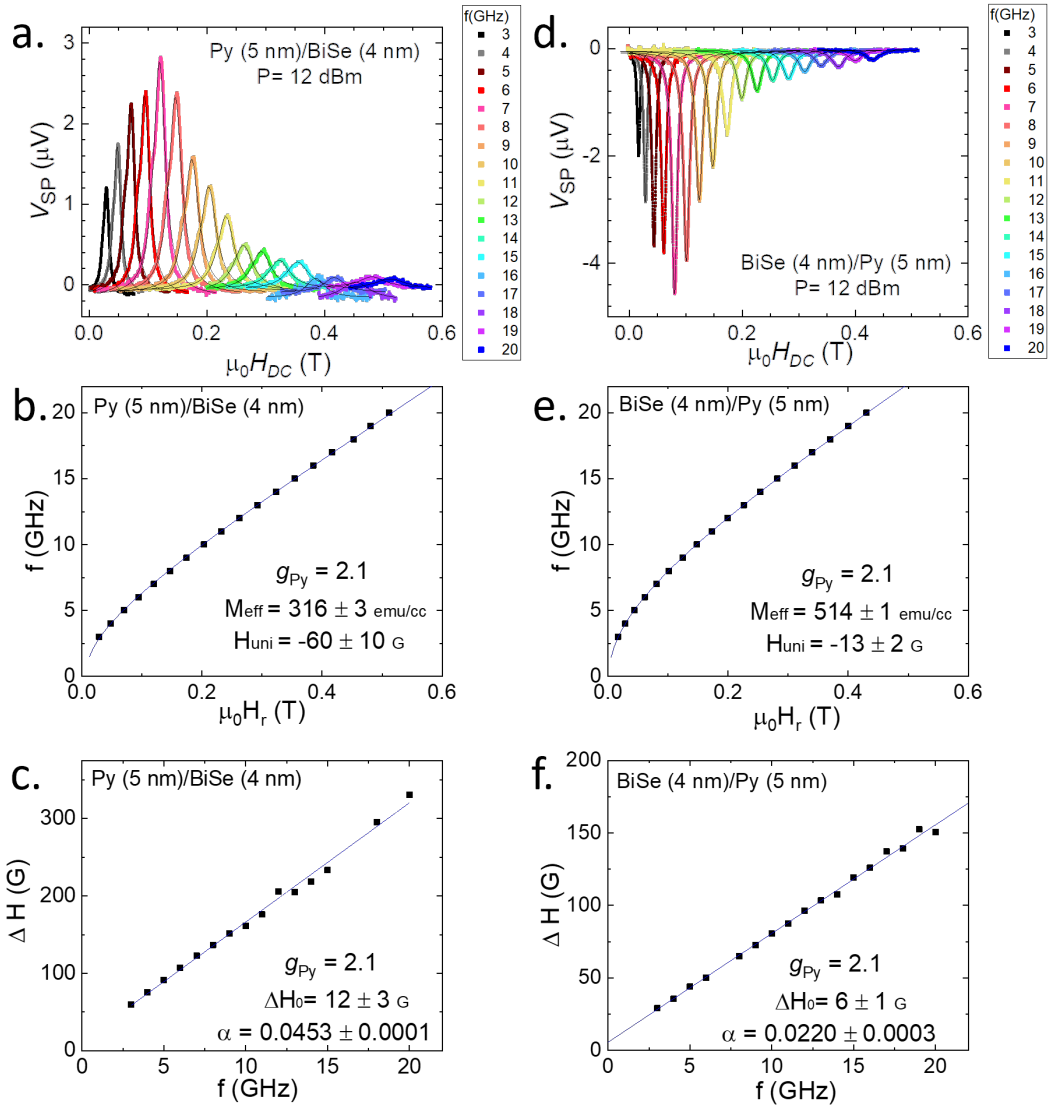

Figure 4.3: Evolution of the spin pumping measurements as a function of frequency. a. Evolution of the spin pumping voltage with the frequency of the RF excitation as a function of the DC magnetic field, and **b.** the extracted resonance field and **c.** the extracted line width as a function of the frequency for the Py/BiSe bilayers. **d**, **e**, **f**. The same results for the other stacking order, BiSe/Py samples, respectively.

We can also observe that M_{eff} is lower in both BiSe stacks than in the Pt stack, which presents a value closer to the one of bulk Py [192]. The obtained values of H_{uni} are small in all cases, suggesting that the Py layers do not have a significant anisotropy in the film plane. Even though this is true, we observe a larger value for the case of the Py/BiSe sample (-60 ± 10 G) compared to the BiSe/Py (-13 ± 2 G).

4.3.2 Structural characterization by TEM

It has been widely acknowledged that the interface plays a crucial role in the injection of spin currents between different materials [15, 55, 80, 132, 193–195]. In order to further explore the origin of these differences, we study the structural properties of our samples by comparing how the interface changes with the stacking order in a cross-section of the sample observed by TEM. We show the two opposite stacking orders Py/BiSe and BiSe/Py in Figs. 4.4a and 4.4b, respectively.

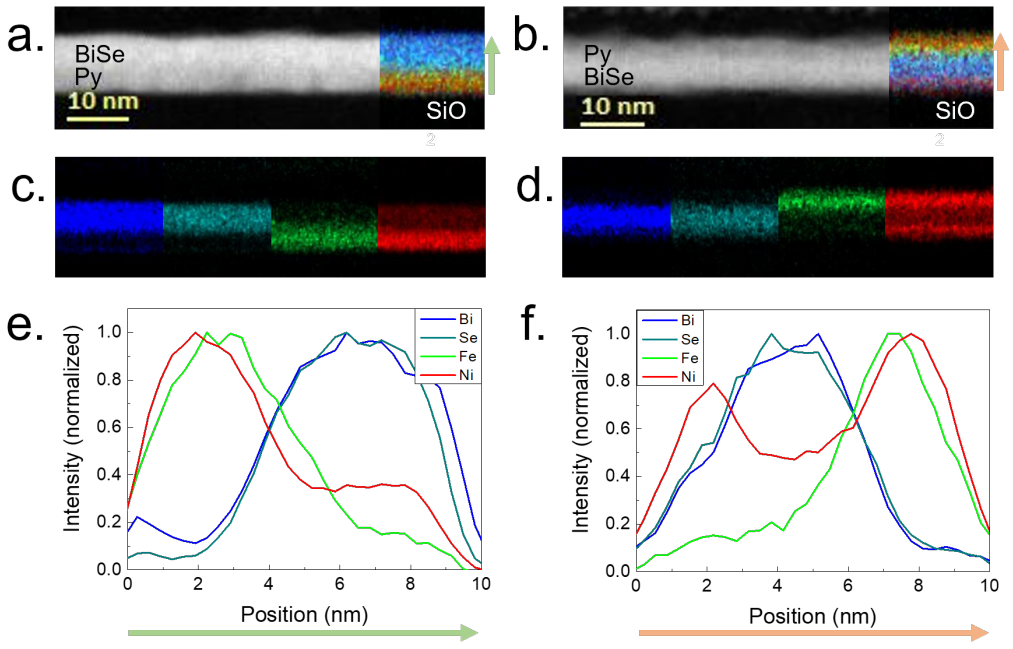

Figure 4.4: Interfacial structure and chemical characterization of thin film bilayers. a. Py(5 nm)/BiSe(4 nm) and **b.** BiSe(4 nm)/Py(5 nm) by TEM. Elemental EDX maps of **c.** Py/BiSe and **d.** BiSe/Py with the essential elements: Bi (blue), Se (dark cyan), Fe (green), and Ni (red), with the SiO_2 substrate at the bottom and the capping layer at the top. Elemental normalized profiles of **e.** Py/BiSe and **f.** BiSe/Py, starting from the substrate (left) to the top (right). The green (a, e) and orange (b, f) arrows indicate the direction of the scan.

In both cases, a uniform and continuous material deposition is observed. Additionally, the chemical distribution has been characterized by EDX. Figures 4.4c and 4.4d show the different elemental maps obtained by EDX. Figures 4.4e and 4.4f display the normalized elemental profiles for each stack.

A strong diffusion of Ni through the BiSe layer is observed in both cases, in agreement with previous studies [56]. A clear shift of the Ni (red line) curve is observed in the elemental profiles, being larger when BiSe is at the bottom of Py (Fig. 4.4f), with Ni penetrating through all the BiSe layer and accumulating at the bottom. As a consequence, Fe is shifted in both stacking orders (green line) creating a Fe-rich interface with the BiSe.

The interface between BiSe and Py is completely modified in both stacking orders, and this also alters the spin injection efficiency for spin transport measurements. By comparing our spin pumping and EDX-STEM results, we can observe that the bilayer with the highest interdiffusion, BiSe/Py, also has the highest charge current produced since we have a more complex structure with a large intermixing of chemical elements at the interface. Quantification of the spin-charge interconversion efficiency by assuming a single bilayer would thus be meaningless.

4.4 Discussion

The migration of Ni in the Py/BiSe sample can also explain the origin of the reduced effective magnetization as well as the change in α. The Gilbert damping increases twofold for the Py/BiSe and fivefold in the BiSe/Py samples in comparison to Py/Pt. This could be due to a combination of the interdiffused interface and the different SOC in the BiSe.

The different compositions of the Py close to the interface could also have a relevant impact on the spin pumping voltage since it is very sensitive to the transparency of the interface. The migration of the elements in both samples could lead to a gradient of magnetic composition, since the moment per atom of Ni (bulk saturation magnetization M_s=485 emu/cm^3) and Fe (bulk M_s=1707 emu/cm^3) [196] are very different (see section 4.6.3 for magnetometry measurements).

In fact, while α doubles for the Py/BiSe sample compared to the BiSe/Py one, ΔH_0 is also two times larger, indicating that the origin of this increase is not due to an interfacial effect but is related to a change of properties of the magnetic layer. M_{eff} is usually different to M_s and changes in the sample anisotropy typically lead to

a reduction in M_{eff}, but not in M_s. In the thin film limit and when the magnetic anisotropy is negligible, M_{eff} and M_s are similar. In this sense, a gradient of composition in Ni and Fe could also be the origin of an out-of-plane anisotropy that causes a reduction in M_{eff} similar to what we observe in both stacks.

In contrast, regarding the change in composition, one could expect that a reduction of the Ni percentage in the Py layer would produce an increase in M_{eff}. Regarding the reduced charge current generated by spin pumping, it is relevant to consider the role of the Ni migration and how this could induce spin currents coming from the Ni and Fe inside the BiSe and even an opposing voltage coming from the migrated Ni layer in the case of the BiSe/Py stack.

These deviations from the conditions considered for the determination of the parameters shown in table 4.1 directly affect the reliability of the obtained values. For example, the model to obtain $g_{\uparrow\downarrow}$ implies that both materials at the interface have the same composition as the magnetic layer and we observe a mixed interface. Additionally, the extraction of M_{eff} from Eq. 2.37 implies that the magnetic layer is homogeneous or the voltage measured comes from the spin conversion in BiSe, while in reality, we do not have a homogenous magnetic layer or a pure BiSe film. Furthermore, given that the magnetic properties of the magnetic layer are different for the different stacks, the spin current generated can also vary significantly even though the h_{RF} is similar.

4.5 Summary and conclusions

In this chapter, we show that the charge current generated by spin pumping in sputtered BiSe has the same sign as the one of Pt and is significantly lower than a Py/Pt reference sample. By measuring the frequency dependence of the spin pumping voltage, we compare the different magnetic and interfacial properties of a Py/BiSe and a BiSe/Py bilayers and observe that the effective magnetization and Gilbert damping are very different between the two stacks and that a small unidirectional anisotropy in the Py develop in both cases.

In order to understand this behavior, we study the structure and composition of both systems by transmission electron microscopy and energy dispersive X-ray spectroscopy, finding a strong interdiffusion characteristic of BiSe thin films. The chemical composition of the magnetic layers and the interfaces are not homogeneous and, therefore, the models used to characterize the properties of the sys-

tem are not valid anymore. These inhomogeneities in the interfaces and the films enhance the Gilbert damping constant and reduce the effective magnetization, which would lead to an incorrect estimation of the spin conversion parameters. Additionally, the compositional gradient in the Py layer might induce anisotropies that reduce the effective magnetization in both stacks.

The results presented in this chapter highlight the importance to study the interfacial and compositional properties of BiSe systems for spin-to-charge conversion since they tend to produce systems with very high interdiffusion and thus the performance is highly dependent on the quality of the layers and interfaces as well as their stoichiometric composition.

4.6 Appendices

In this section, complementary data to support our results in previous sections are added.

4.6.1 Appendix A: Details on the lock-in measurements

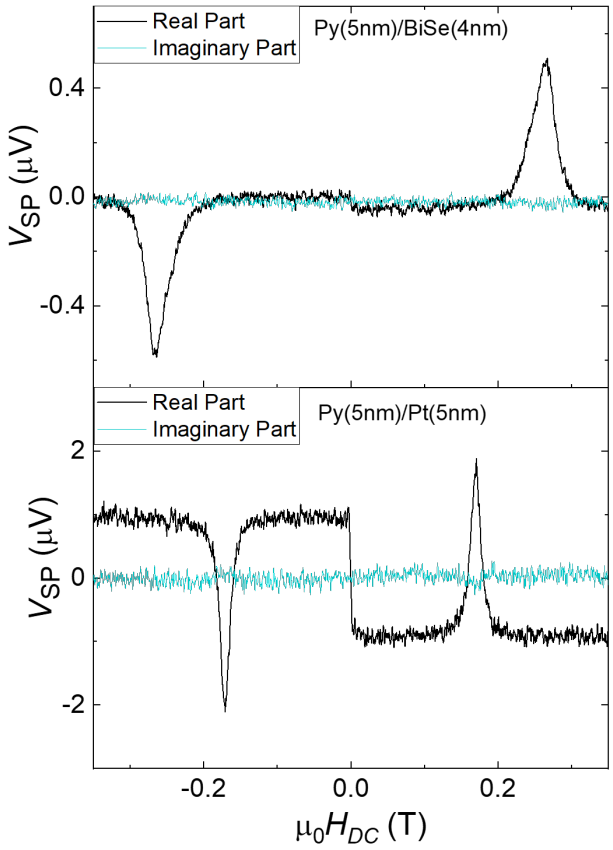

Figure 4.5: Real and imaginary parts of the lock-in. Lock-in voltage of the real and imaginary parts detected in the SP experiments for the bilayers: Py/BiSe and Py/Pt at 12 GHz and 12 dBm.

In our SP experiments, we modulated the amplitude of the RF signal rather than the magnetic field. We always fix the phase so that no extra phase was added by the modulation signal. Transport effects are fast enough to appear without delay in the measurement while thermal effects that might be slower would appear in the imaginary part of the signal. To further ensure this, we always recorded both the real and the imaginary parts of the voltage simultaneously.

As an example, we show in Fig. 4.5 the real and imaginary parts of the lock-in voltage detected in SP experiments for both Py/BiSe and Py/Pt samples. The voltage signal always appears in the real part of the lock-in measurement. Repeated measurements with nominally the same layer structure on multiple devices lead to deviations in V_{SP} below 5%.

4.6.2 Appendix B: Spin pumping measurements in the reference sample

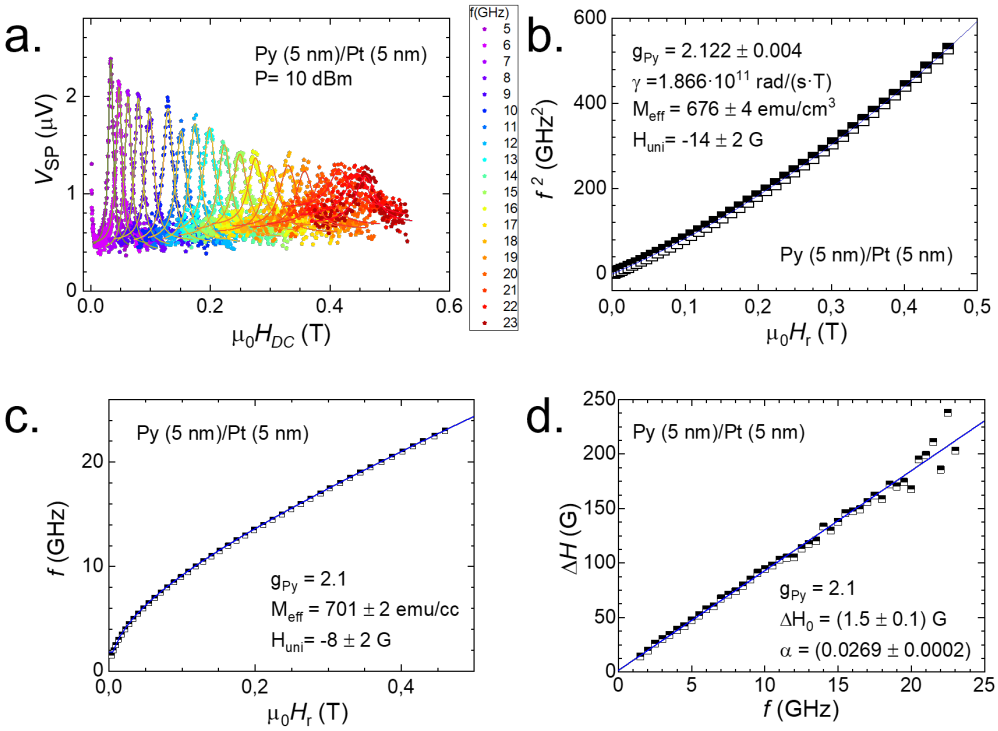

Figure 4.6: Evolution of the spin pumping measurements as a function of frequency for the reference sample a. Evolution of V_{SP} with frequency of the RF excitation as a function of the DC magnetic field. **b.** Frequency square as a function of H_r. **c.** The extracted resonance field and **d.** the extracted line width as a function of the frequency for the Py $(5$ nm$)$/Pt $(5$ nm$)$ sample.

Figure 4.6a shows the evolution of V_{SP} with the frequency for the reference sample: Py $(5$ nm$)$/ Pt $(5$ nm$)$. To extract the Landé factor of Py (g_{Py}), we plot f^2 as a function of H_r (see Fig. 4.6b), and fitted the data using Eq. 2.37. The g_{Py} value obtained, 2.122 ± 0.004, is similar to previous reported values for Py [197], and we thus fix it to 2.1 for the analysis of the SP results in this thesis. Figures 4.6c and 4.6d show

the equivalent plots as in Fig. 4.3 for the reference sample. The extracted values are given in Table 4.1.

4.6.3 Appendix C: Magnetometry

Here we add magnetometry data performed in a new set of samples grown under the same conditions and measured by vibrating sample magnetometry (VSM).

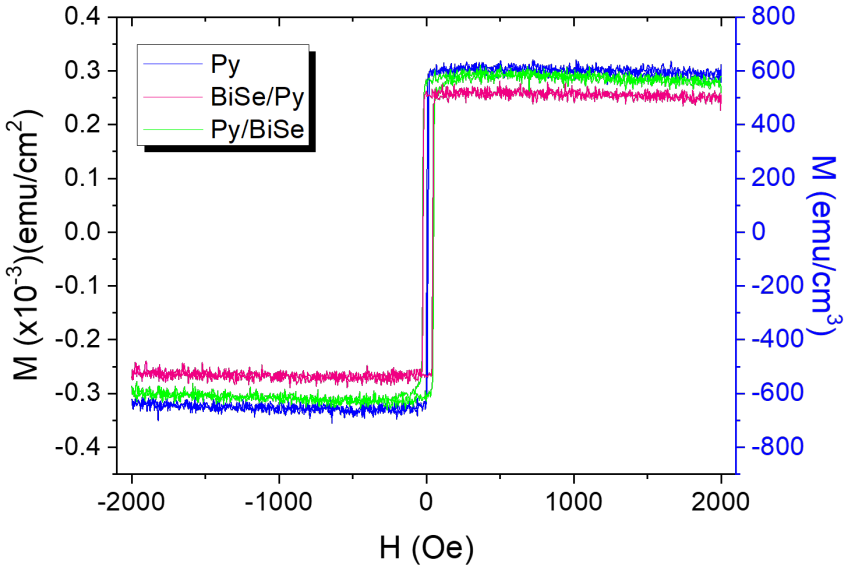

Figure 4.7: Magnetic characterization of bilayers. Magnetometry measurements of the Py/BiSe, BiSe/Py and Py/Pt bilayers for a different set of samples grown under the same conditions as the ones described above in section 4.3.1. The hysteresis loops were measured at room temperature with a vibrating sample magnetometer (VSM). The magnetization by unit volume in emu/cm^3 is calculated considering a Py thickness of 5 nm, while the moment per unit area is calculated normalizing by the surface of the sample measured in the VSM.

Figure 4.7 shows the in-plane hysteresis loops obtained by VSM for the new set of samples. We observe the same trend for the saturation magnetization (M_s) as in the measurements of the effective magnetization (M_{eff}) reported in the main text, but the absolute values differ, especially for the Py/BiSe sample, whose M_s here is around 500 emu/cm^3 compared to the 316 obtained for M_{eff} in the spin pumping measurements (table 4.1). This could be explained considering that, since there is a significant interdiffusion, and even Ni accumulated at the other side of the interface, the volume we need to calculate M_s is not well defined. In that sense, we

have included in Fig. 4.7 the magnetization considering a Py layer of 5 nm (right axis), but also the magnetic moment normalized by the surface of the sample (left axis).

Chapter 5

Quantification of spin-charge interconversion in sputtered BiSe with T-shaped devices

5.1 Introduction

As discussed in Chapter 1, the main motivation of this thesis is to find a material to be placed inside the readout node of the MESO device, in which BiSe was proposed as a promising candidate. However, we showed in Chapter 4 the formation of an interfacial layer between BiSe and transition metals by a solid-state reaction, in agreement with other recent studies [56, 198, 199]. This observation encourages rigorous characterization of sputtered BiSe.

In this chapter, we show the influence of the intermixing at the junction of BiSe and transition metal on the characterization of the electrical and spintronic properties of BiSe using a local spin Hall (T-shaped) device, which has a similar geometry to the MESO device (see section 2.3.2). In this approach, we used CoFe as the FM material in contact with BiSe instead of Py, which gives many problems as shown in Chapter 4. The sputtered BiSe/CoFe and CoFe/BiSe bilayers were first characterized by TEM and EDX to check the interfaces previous to the fabrication of the devices. Subsequently, electrical measurements and 3D FEM simulations were performed for the local devices in order to quantify the SCI efficiency (θ_{SH}^{BiSe}).

By studying the BiSe thickness dependence of the SCI signal and the cross-junction resistance, we observed a large variation in resistivity and θ_{SH}^{BiSe} correlated with the compositional change of BiSe caused by the adjacent transition metal layer. This result emphasizes the importance of proper material characterization, as it can greatly affect the SCI efficiency evaluation, especially in the case of structures or devices containing reactive materials such as BiSe and transition metals.

5.2 Experimental details

Initially, to characterize the resistivity of BiSe, we used nanowires of BiSe with different lengths between contact electrodes (see Fig. 5.1a). The device is fabricated by two eBL steps: First, the 320-nm-wide nanowire is patterned using a double layer of PMMA and then 30 nm of BiSe are deposited by RF sputtering from a stoichiometric Bi_2Se_3 target using an RF power of 35 W at 3 mTorr. This wire is capped *in situ* by sputtering 5-nm-thick SiO_2 using a RF power of 200 W at 3 mTorr.The capping layer is needed to protect BiSe by the anisole solvent of the PMMA resist, which damages the material. When dipping the BiSe sample in anisole (without the capping layer), the resistivity increases more than 10 times.

The second eBL step is for the Ti(5 nm)/Au(40 nm) contact electrodes. The eBL patterning of the electrodes was performed with a double layer of PMMA for electrodes with the same width of the BiSe wire at the cross junction. Subsequently, we performed ion-milling of the capping layer on top of the BiSe wire while monitoring the endpoint detector mass-spectrometer to stop the process when the capping layer is completely removed. The milling rate of BiSe is extremely fast (~ 0.4 nm/s), which is important to take it into account not to over-mill all the material. The Ti and Au deposition is performed by e-beam and thermal deposition, respectively.

On the other hand, thin film bilayers composed of BiSe (16 nm thick), CoFe (15 nm thick) and SiO_2 capping layer (5 nm thick) were prepared to characterize the sputtered BiSe/CoFe and CoFe/BiSe interfaces prior to fabrication of local spin Hall (T-shaped) devices and SCI experiments (see Fig. 5.2).

Finally, to study SCI in BiSe, we use the local spin Hall device shown in section 2.3.2, which corresponds to the architecture of the SO reading module of the MESO device (section 1.3). All materials constituting the local spin Hall device were grown by DC (metal) and RF (BiSe and SiO_2 capping layer) sputter deposition. The device consists of a top T-shaped nanostructure of BiSe (2 to 40 nm)/NM (Ti, Pt or Ta; 10 nm) and a bottom 15-nm-thick CoFe electrode, all with a width of 80 nm, following the fabrication steps described in section 3.1.2. Since sputtered BiSe has a high noise level in electrical measurements, a NM such as Ti, Pt, and Ta is deposited on top of BiSe to pick up the SCI output voltage through electrical shunting.

The devices are fabricated on cleaned Si/SiO_2 substrates by two steps of eBL. We use single layer PMMA, followed by the development, magnetron sputter deposition, lift-off and ion-milling (see Chapter 3 for details of each technique). The CoFe wire is patterned as the first layer and deposited by DC magnetron sputtering of 30 W at 2 mTorr of Ar pressure. To eliminate sidewalls on the CoFe wire, ion-milling (Ar flow of 15 sccm, acceleration voltage of 50 V, a beam current of 50 mA, and beam voltage of 300 V) is performed with an incident beam angle of 20° after the lift-off process (see step h in Fig. 3.1). The second step of the eBL is the T-shaped wire: after the development, BiSe is deposited by magnetron sputtering using the same conditions mentioned before. Subsequently, NM is deposited *in situ* using DC power (80 W for Pt, 100 W for Ti, 200 W for Ta) at 3 mTorr and lift-off is performed.

5.3 Characterization of BiSe

5.3.1 Resistivity of BiSe

The high resistivity reported for sputtered BiSe is one of the reasons it is considered a strong candidate for the magnetic readout node of MESO logic devices [11, 12, 200]. Figure 5.1b shows the resistance area product of a 30-nm-thick and 320-nm-wide BiSe nanowire measured at room temperature (300 K) with 4-points, for different electrode distances using the Ti/Au contacts. The resistivity of the BiSe nanowire (4000 ± 1000 $\mu\Omega$cm) was obtained from the linear fitting. Unlike metallic conductors, BiSe has a high noise level in the electrical measurements and thus a large dispersion from the fitting line.

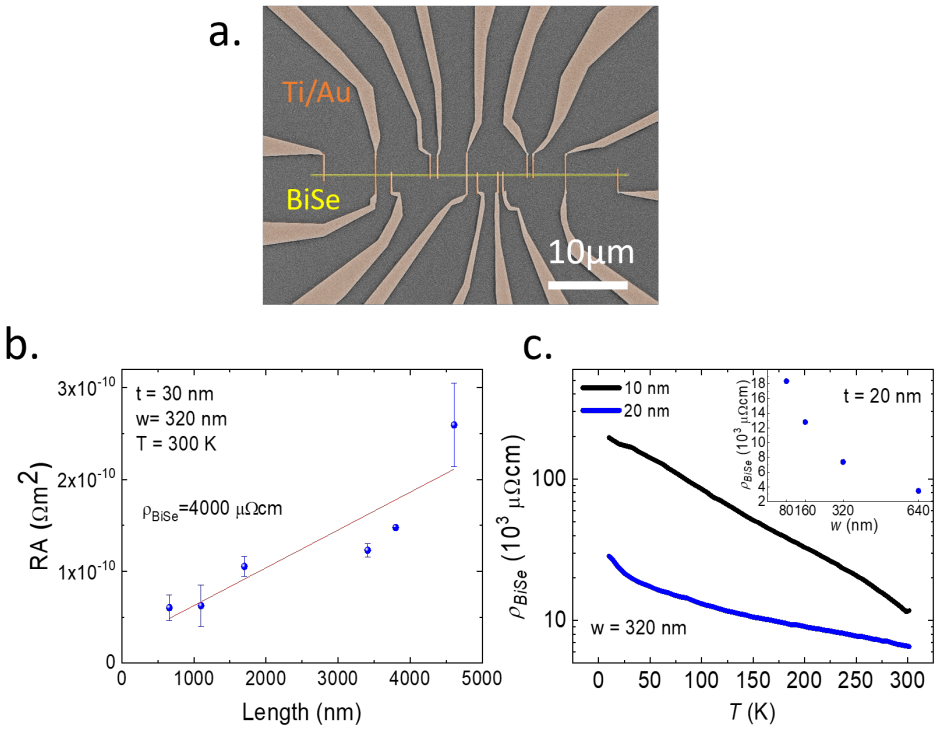

Figure 5.1: Electrical characterization of BiSe. a. Top-view SEM image of the BiSe wire used to measure the resistivity, with different lengths between metallic electrodes. The BiSe wire (yellow) is in the middle, with the metallic contacts of Ti (5 nm)/Au (40 nm) (orange). **b.** Length dependence of the resistance area product measured for a 320-nm-wide and 30-nm-thick BiSe wire at room temperature. From the linear fitting, a resistivity of 4000 $\mu\Omega$cm is determined. **c.** Resistivity of BiSe as a function of temperature for a 320-nm-wide wire with thickness of 10 nm (black) and 20 nm (blue). Inset: Width dependence of the resistivity of a 20-nm-thick BiSe wire.

As shown in Fig. 5.1c, the resistivity increases as the temperature decreases, indicating a semiconducting behavior, and varies with the thickness (10 and 20 nm), and width (80 - 640 nm) of the nanostructure. The BiSe wire with 80 nm width and 20 nm thickness has a resistivity of 18000 $\mu\Omega$cm at room temperature, which shows that the sputtered BiSe used in this experiment is similar to those previously reported [49].

5.3.2 TEM characterization

TEM images in Figs. 5.2a and 5.2b show the structures of SiO_2 substrate/BiSe/CoFe/SiO_2 capping layer and the opposite stacking order, SiO_2 substrate/CoFe/BiSe/SiO_2 capping layer, respectively. The sputtered BiSe layer is polycrystalline in both cases, although it is more oriented on top of the CoFe layer than on top of the SiO_2 substrate (see section 5.6.1 for complementary TEM characterization of the intermixed layer).

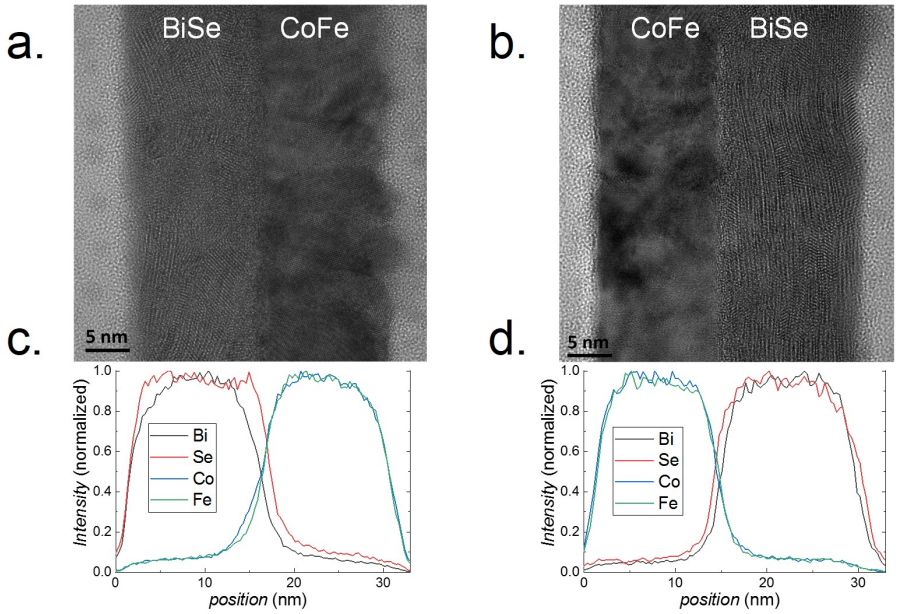

Figure 5.2: Characterization of BiSe interfaces for local devices. TEM images and normalized EDX element mapping results of bilayer stacks when BiSe is placed at the bottom [BiSe/CoFe (**a.** and **c.**)] and at the top [CoFe/BiSe (**b.** and **d.**)] of the FM material.

In both cases, an amorphous layer was found at the interface, being thicker in the BiSe/CoFe stack, when BiSe is at the bottom. Such layer corresponds to intermixing at the interface, as confirmed by normalized EDX spectroscopy, which shows

a clear shift of the Se curve (red) in both cases as shown in Figs. 5.2c and 5.2d, being larger in the BiSe/CoFe stack in agreement with the thicker amorphous layer. Since such an imperfection at the interface will adversely affect the spin injection between the two materials and the subsequent SCI, we chose the CoFe/BiSe stack (Figs. 5.2b and 5.2d) to minimize its influence and keep BiSe close to pristine conditions.

5.4 Local spin Hall devices

To quantify the signal arising from the ISHE, the transverse voltage (V_{ISHE}) is measured while an external magnetic field is applied along the easy axis of the CoFe electrode (x-axis) and a current (I_c) flows from CoFe to one end of the BiSe/NM T-shaped nanostructure, as shown in Fig. 5.3a. The reciprocal measurement (arising from the SHE) is described in Fig. 5.3b. Spin-polarized current in the CoFe wire flows vertically through BiSe to the NM due to the large difference in resistivity, and the ISHE occurs inside BiSe. The resulting charge current is then measured transversely in the T-shaped structure as an open circuit voltage, V_{ISHE}. When the magnetization of the CoFe electrode is switched, the spin polarization also reverses and V_{ISHE} changes sign. The ISHE resistance, defined as $R_{ISHE} = V_{ISHE}/I_c$, always contains a baseline value, and therefore it is more convenient to define the ISHE signal, $2\Delta R_{ISHE}$, as the difference between the two magnetic states (see Fig. 5.3c).

The converted current is mostly shunted by the CoFe electrode and, since the NM completely covers the BiSe T-shaped nanostructure, partially by the NM greatly reducing the magnitude of V_{ISHE}. What we finally measure is the voltage across the Hall cross shunted by the NM, thus being dependent on the resistivity of the NM. Nevertheless, the use of a NM layer is crucial, as it dramatically lowers the noise level and makes the ISHE signal measurable, in contrast to the use of lateral NM contacts in a BiSe-only T-shaped nanostructure.

Figure 5.3c shows the ISHE signal of 15.1 ± 0.4 mΩ measured on a BiSe (3 nm)/Ti (10 nm) device. The hysteresis loop was observed according to the switching field of the CoFe wire, and the current dependence and the reciprocal measurement (SHE signal shown in the inset of Fig. 5.3c) confirm that they were conducted in the linear response regime, which rules out the presence of any heating-related effects. The same measurement on a BiSe (3 nm)/Pt (10 nm) device is shown in

Fig. 5.3d, with an ISHE signal of 5.4 ± 0.5 mΩ, which is 3 times smaller than that of a BiSe/Ti device with the same thickness.

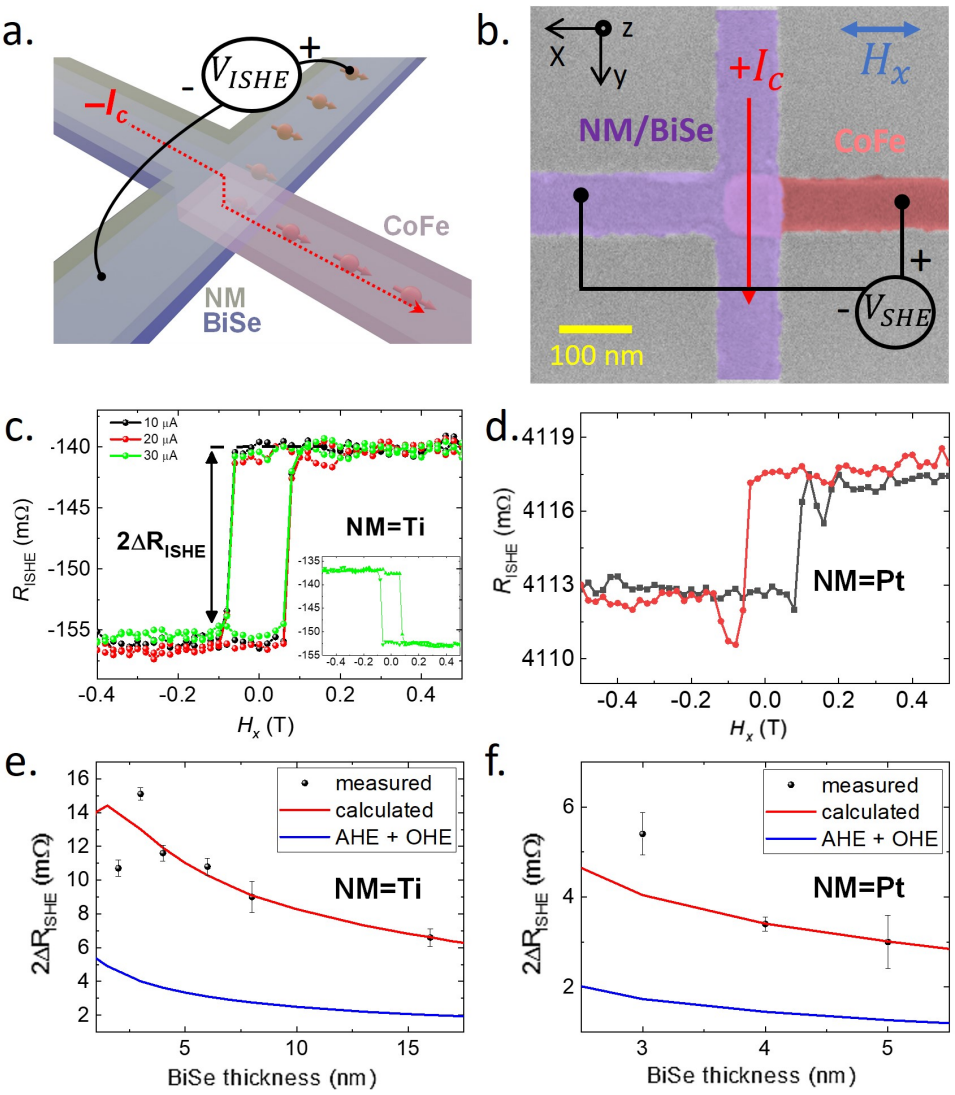

Figure 5.3: Local spin Hall device and SCI signals. a. Sketch of the local spin Hall device with the ISHE measurement configuration. **b.** False-colored SEM image of the local device, with the CoFe electrode in pink and the BiSe T-shaped structure in purple. The electrical configuration is presented for the SHE measurement. ISHE resistance, R_{ISHE}, measured using the configuration in panel a. as a function of the external magnetic field for **c.** BiSe(3 nm)/Ti (10 nm) and **d.** BiSe(3 nm)/Pt (10 nm) nanostructures. The inset in panel c. shows the SHE resistance measured using the configuration in panel b. as a function of the external magnetic field. The ISHE signal, $2\Delta R_{ISHE}$, as a function of BiSe thickness with the fitting curves obtained by 3D FEM simulations for **e.** BiSe/Ti and **f.** BiSe/Pt. All measurements are performed at room temperature.

Since the ISHE can occur in the adjacent NM when BiSe is thin, we need to prove whether the ISHE signal is generated in the BiSe. On comparison of the ISHE signals of the two devices, however, θ_{SH} of Ti is negligible (-0.00036) [201] while Pt is known as a material which has high θ_{SH} (~ 0.1) [72, 202] so even considering the high resistivity of Ti, the larger ISHE signal observed cannot be properly explained.

As a further check, we also fabricated devices with Ta as the NM. The sign of θ_{SH} in Ta is opposite to that of Pt [73], but the ISHE signal of a BiSe (2 nm)/Ta (10 nm) device has the same sign as those of the other devices (see Fig. 5.4), clearly showing that the ISHE appears in the thin BiSe layer, regardless of the NM used.

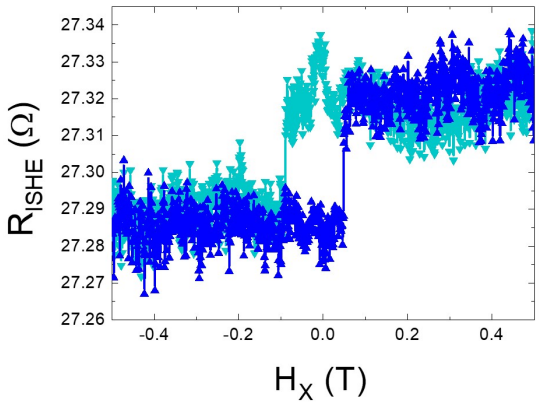

Figure 5.4: BiSe/Ta local device. ISHE resistance as a function of the external magnetic field obtained in a BiSe/Ta local spin Hall device.

Figure 5.3e shows $2\Delta R_{ISHE}$ as a function of the BiSe thickness in the BiSe ($2-16$ nm)/Ti (10 nm) local spin Hall devices. $2\Delta R_{ISHE}$ is largest for 3 nm of BiSe, and it decreases for thicker structures. The same experiment was conducted with BiSe ($3-5$ nm)/Pt (10 nm), as shown in Fig. 5.3f, yielding a similar trend. The ISHE signal could only be observed up to 16 nm of BiSe for Ti and up to 5 nm for Pt, with no signal obtained at a thickness beyond that, mostly due to the increasingly higher noise level and low ISHE signal.

We should mention that an AHE [34, 123, 127] and OHE [162] can appear as artifacts in the ISHE measurements (see section 5.6.2). The anomalous Hall angle obtained by applying an out-of-plane magnetic field to CoFe in our own devices is 1.5%. In the local spin Hall device, the contribution of the AHE is greatly reduced, since the magnetization points along the x-axis and only the contribution by the current flowing in the z-axis is considered. The contribution of the AHE was calculated by a 3D FEM based on the spin diffusion model [34, 123, 127, 203], and we

obtained less than 6 and 2 mΩ AHE signals in the whole thickness range for BiSe/Ti and BiSe/Pt structures, respectively. Additionally, the stray field of CoFe-induced OHE is calculated by 3D FEM simulation based on the Hall coefficient of BiSe/NM structures obtained by applying the out-of-plane magnetic field to each structure [162]. We obtained less than a 0.3 mΩ OHE contribution for both structures. As shown in Figs. 5.3e and 5.3f, the calculated AHE and OHE signals decay with BiSe thickness since current shunting is suppressed and the distance between FM and NM increases, respectively.

Next, we analyzed the thickness dependence of the ISHE signal by a 3D FEM simulation [34] also taking into account the AHE and the OHE discussed above. The simulation is performed by assuming that the resistivity of BiSe is 18000 $\mu\Omega$cm (20-nm-thick and 80-nm-wide wire in the inset of Fig. 5.1c). The resistivities of CoFe and Ti were 42 and 40 $\mu\Omega$cm, respectively, which were measured directly on the device. The obtained λ_s^{BiSe} is 0.5 nm (see section 5.6.3 for quantification of λ_s^{BiSe} by the local spin Hall devices) and θ_{SH}^{BiSe} is 27.5, a very large value that is in good agreement with the previously reported value [49], and it seems to prove once again that sputtered BiSe is one of the most promising materials for SCI devices, in particular for the MESO logic device, which also requires a high resistivity.

However, unlike the previous report, the quantum confinement [49] cannot be confirmed here, as a single θ_{SH}^{BiSe} value of 27.5 is obtained over the whole BiSe thickness range of 3-16 nm. The hybridization of the topological surface state reduces the SCI signal when a TI is thinner than 6 nm [204], but the maximum signal is at 3 nm, as shown in Fig. 5.3e. The activation of the topological surface state or the suppression of bulk conduction at cryogenic temperature reduces the resistivity [205, 206], which is not observed in this work, as shown in Fig. 5.1c. From all these facts, it is reasonable to consider sputtered polycrystalline BiSe as a normal conductor rather than a TI.

On the other hand, the cross junction resistance (R_{CJ}) as a function of the thickness of BiSe as shown in Figs. 5.5a and 5.5b disagrees with such a high resistivity of BiSe. The sketch in Fig. 5.5a shows the measurement configuration of R_{CJ}. In the BiSe/Ti structures shown in Fig. 5.5a, R_{CJ} shows a constant increase with the BiSe thickness from 2 to 16 nm, but the overall values are unexpectedly low. Even in BiSe/Pt devices shown in Fig. 5.5b, although the change of R_{CJ} is higher than that of BiSe/Ti, the values are rather similar. This measurement assumes a vertical current flowing uniformly across the junction. Considering the large resistivity difference between BiSe and metallic wires such as Pt, Ti, and CoFe, the current stays in the CoFe until reaching the junction and flows vertically through BiSe to

NM, so that the R_{CJ} is expected to be more than $80\ \Omega$ for 3-nm-thick BiSe when a resistivity of $18000\ \mu\Omega$cm and a junction area of 80 nm $\times$ 80 nm are considered. However, the measured R_{CJ} on the devices with BiSe thicknesses up to 4 nm has negative values, which is generally considered as a transparent interface, hinting that the resistivity of BiSe may be lower than that initially measured in nanostructures without the NM. In order to reliably extract the resistivity of BiSe, we perform a 3D FEM simulation [195] of the R_{CJ} measurements, where the independently measured resistivities of the NM (Ti or Pt) and CoFe are used as inputs and the only unknown parameter is the BiSe resistivity. The 3D FEM simulation results are shown by red lines in Figs. 5.5a and 5.5b. The resistivities of BiSe are calculated to be $600\ \mu\Omega$cm for the BiSe/Ti structure, which is 30 times smaller than the values measured in the narrowest BiSe wire in the inset of Fig. 5.1c, and $3700\ \mu\Omega$cm in the BiSe/Pt structure, about 6 times higher than that of BiSe/Ti. These results indicate that the top NM layer changes the resistivity of BiSe. In the following paragraphs, we will discuss the origin of such a variation and the consequences in the quantification of the spin Hall effect in sputtered BiSe.

To understand the relationship between BiSe resistivity and the NM used, we performed TEM and EDX experiments in SiO_2 substrate/CoFe (15 nm)/BiSe (30 nm)/Ti (10 nm)/Pt (10 nm) and SiO_2 substrate/CoFe (15 nm)/BiSe (30 nm)/Pt (10 nm) multilayer stacks as shown in Figs. 5.5c and 5.5d (see also section 5.6.1 for the analysis of the actual BiSe/Ti local spin Hall device). In order to obtain a quantitative elemental analysis from the EDX, we exfoliated single-crystal Bi_2Se_3 flakes on top of each stack. Since the Bi_2Se_3 flakes are stoichiometric, the composition of sputtered BiSe can be accurately determined by normalizing the Bi and Se intensity curves to 40% and 60%, respectively. In the BiSe/Ti structure, a clear peak of the Se curve, indicated by the blue arrow in Fig. 5.5c, appears as a result of strong intermixing near Ti [55, 56, 198, 199], and BiSe has a $50:50$ composition in the rest of the layer. No intermixing was observed between BiSe and Pt, where the composition was $45:55$. Eventually, we obtained two different BiSe compositions depending on the chosen NM, even with the same growth condition. This is the reason the resistivity of BiSe varied from 600 to $3700\ \mu\Omega$cm in the two structures depending on the NM used.

Still, the composition change alone does not explain the high resistivity ($18000\ \mu\Omega$cm) obtained in the BiSe wire measured laterally (Fig. 5.1c). Using impedance measurements, we confirmed that there are two resistance elements, the grain and grain boundary (see section 5.6.4). Accordingly, the absence of grain boundaries in the vertical direction for a BiSe thickness below 16 nm drastically reduces the

BiSe resistivity when it is measured along this direction as compared to the lateral measurement, which includes the grain boundary contribution making a high noise level. The BiSe wire has a resistivity of $18000\ \mu\Omega$cm as a series resistance of grain and grain boundary without intermixing, and the resistivity of $3700\ \mu\Omega$cm measured vertically in the BiSe/Pt structure is of the parallel resistance of grain and grain boundary without intermixing. On the other hand, in the BiSe/Ti structure, the resistivity of $600\ \mu\Omega$cm appears as a parallel resistance of grain and grain boundary accompanied by composition change due to intermixing. The different conditions are summarized in Table 5.1.

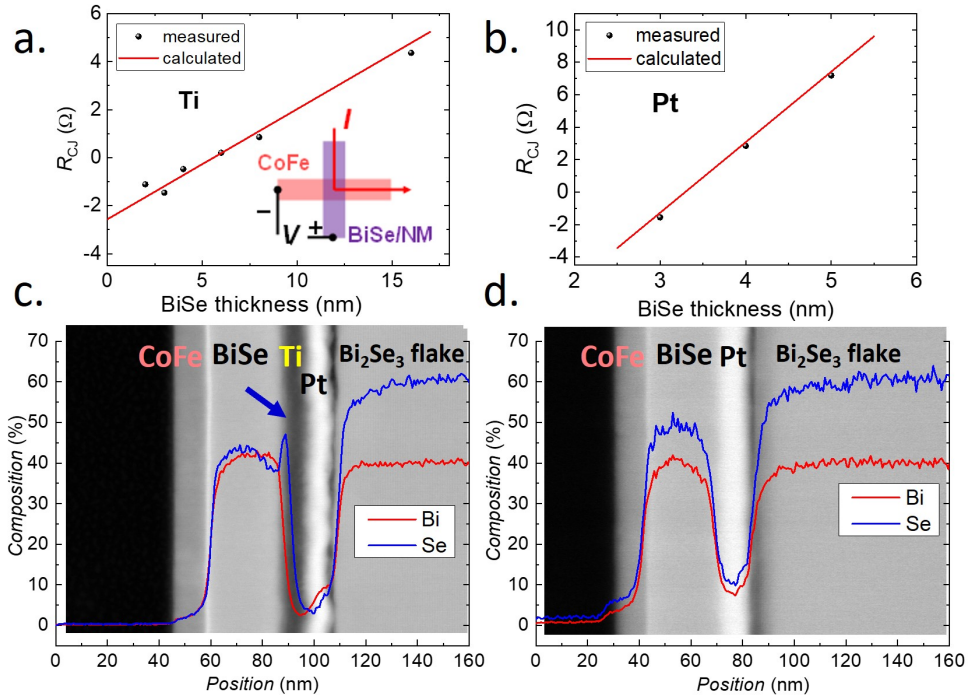

Figure 5.5: BiSe resistivity in the vertical direction. Resistances at the cross-juctions of **a.** BiSe/Ti and **b.** BiSe/Pt structures. Inset in panel a.: schematic representation of the cross-junction devices with the electrical configuration geometry. TEM images and EDX scans of **c.** CoFe/BiSe/Ti and **d.** CoFe/BiSe/Pt thin films compared with single crystal Bi_2Se_3 flakes exfoliated on top of the thin films for proper quantification of the composition.

Returning to the ISHE results of Figs. 5.3e and 5.3f, it is necessary to accurately estimate θ_{SH}^{BiSe} once again, because the resistivity of BiSe can affect the spin injection efficiency and current shunting, and consequently θ_{SH}^{BiSe}. As a result of the 3D FEM simulation performed using the resistivity obtained in Figs. 5.5a and 5.5b, a λ_s^{BiSe} value of 0.5 nm and θ_{SH}^{BiSe} value of 0.45 are estimated for the BiSe/Ti devices. In the

case of BiSe/Pt devices, we extract a λ_s^{BiSe} value of 0.35 nm and θ_{SH}^{BiSe} value of 3.2. These results are significantly different from previously reported values [49, 207] and our first estimation because the high BiSe resistivity reduces the ISHE signal by strong spin backflow. In addition, the ISHE signal reduction as BiSe gets thicker is completely explained by the spin diffusion model for the entire thickness ranges, indicating the absence of quantum confinement depending on the grain size [49].

Table 5.1: Summary of BiSe resistivities depending on measurements direction and NM

Structure	Measurement direction	Resistance of grain and boundary	Intermixing	Resistivity ($\mu\Omega$cm)
BiSe wire	lateral	in series	no	18000
BiSe/Pt	vertical	in parallel	no (Se 55%)	3700
BiSe/Ti	vertical	in parallel	yes (Se 50 %)	600

By comparing our results with the reported results (shown in Table 6.1), it is possible to strictly judge the SCI efficiency of sputtered BiSe. The BiSe thickness range used in this thesis covers all references in Table 6.1. The resistivity obtained in papers differs up to 1000 times [207, 208] because of different growth conditions and measurement techniques. Only Ref. [208] reports a resistivity similar to that of the BiSe/Ti structure with also a similar θ_{SH}^{BiSe}, in agreement with our claim. To compare with the published results of spin pumping experiments [50, 51], in which λ_{IREE} is used to quantify the SCI efficiency, the product $\lambda_s\theta_{SH}$ is considered. In fact, this product better quantifies the SCI efficiency in a local spin Hall device [34, 72, 102]. In particular, the θ_{SH}^{BiSe} value of 18.62 [49] is more than 50 times higher than 0.35 which is obtained in the BiSe/Ti structure, but the λ_{IREE} values of 0.32 nm [50] and 0.1 nm [51] are comparable to what we obtain in our local spin Hall devices using BiSe/Ti (0.225 nm) despite differences in experimental methods and ferromagnetic materials. These results indicate that intermixing must be considered in material characterization, especially an appropriate resistivity quantification and that θ_{SH} can be overestimated when these aspects are not properly considered.

5.5 Summary and conclusions

To conclude this chapter, we observed all electrical spin-to-charge conversion in sputtered BiSe in local spin Hall devices at room temperature (300 K) and showed that all parameters related to SCI efficiency, which are resis-

tivity, λ_s^{BiSe}, and θ_{SH}^{BiSe}, were affected by the intermixing with the adjacent nonmagnetic metal used to electrically shunt the BiSe. In particular, the fact that a Se concentration change by intermixing made a difference of 6 times in resistivity shows how easily θ_{SH}^{BiSe} can be overestimated by the resistivity without considering intermixing. Even though the ISHE signal obtained in this study is too small to realize a MESO logic device, it allowed us to quantify the SCI efficiency of sputtered BiSe in functional spintronic devices (instead of the commonly used BiSe/FM bilayers). The potential of highly resistive sputtered BiSe as the active element in the reading module can be exploited by improving different aspects, such as reducing the electrical noise caused by the grain boundary so that the top NM layer shunting the signal can be removed. The NM layer was applied to reduce the noise level in electrical measurements, but it is not a fundamental solution due to its low resistivity, leading to an overall ISHE signal reduction. We suggest that the SCI efficiency and the ISHE signal magnitude can be increased by protecting BiSe with a tunneling barrier, such as MgO, to prevent intermixing, current shunting, and spin back flow, while enhancing the spin injection efficiency.

5.6 Appendices

In this section, complementary data to support our results in previous sections are added.

5.6.1 Appendix A: Polycrystalline BiSe structure and intermixed layer

Figure 5.6a and 5.6b show the polycrystalline sputtered BiSe and the intermixed layer depending on its stacking order (bottom and top, respectively). While the BiSe/CoFe structure in Fig. 5.6a has a thick amorphous intermixed layer, the CoFe/BiSe in Fig. 5.6b has a vague one. In some grains, alternating Bi_2Se_3 quintuple layers and Bi bilayers are found, but its frequency varies even within a grain.

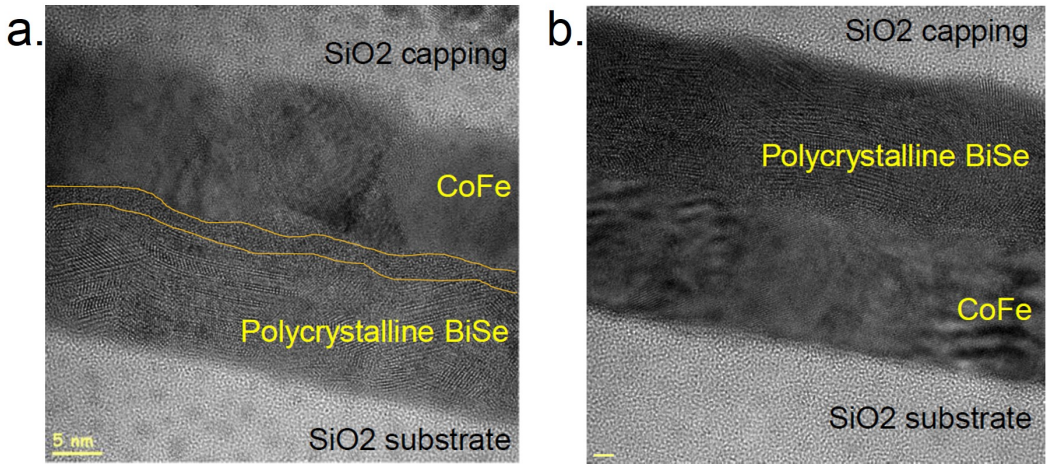

Figure 5.6: Polycrystalline BiSe and intermixed layer. High-resolution TEM images of two differente stacking order: **a**. BiSe/CoFe, and **b**. CoFe/BiSe structures, both samples capped with 5 nm SiO_2. Yellow lines are added to show the amorphous intermixed layer in between the BiSe layer and CoFe layer.

Figure 5.7 shows the TEM image and EDX profile for each element similar to Fig. 5.5, but with 16-nm-thick BiSe. These are obtained by cutting the BiSe/Ti T-shape wire of the local spin Hall device. To know the exact composition of BiSe, we used a Bi_2Se_3 flake exfoliated to normalize as shown in Fig. 5.5, but even without the flake, Se (red curve) diffusion can be clearly seen.

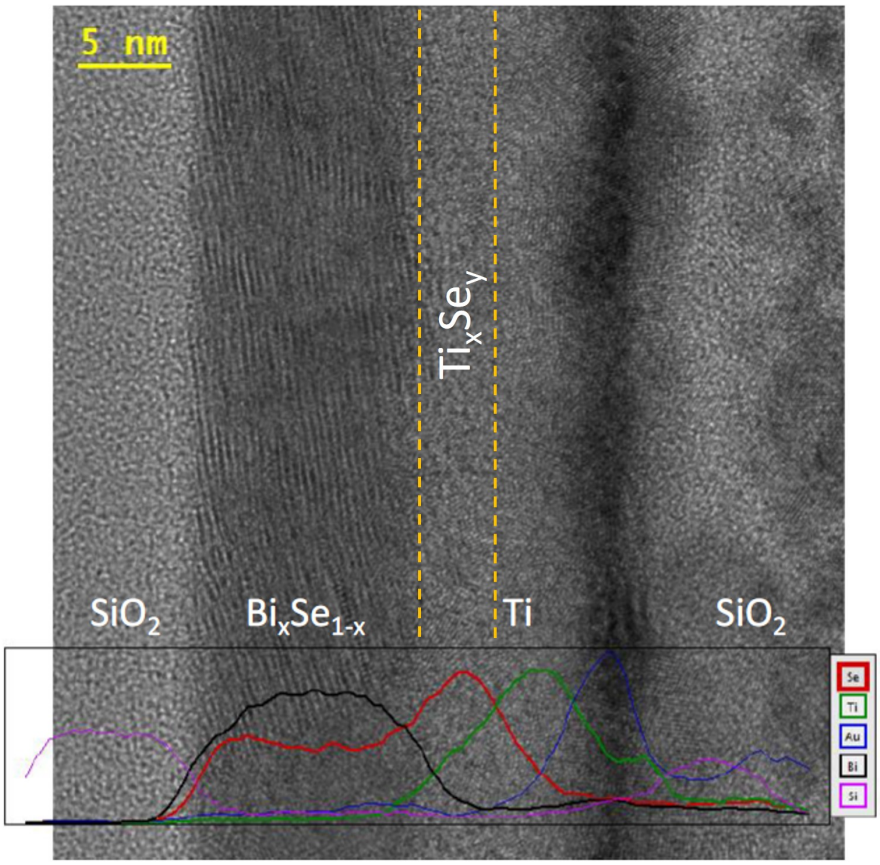

Figure 5.7: BiSe/Ti and intermixed layer in the local spin Hall device. TEM image and EDX profiles of BiSe/Ti structure. Se (red curve) is intermixed with Ti (green curve), creating a new layer at the interface.

5.6.2 Appendix B: Disentangling artifacts from the ISHE signals

Artifacts that can be observed with the ISHE measurement include PHE, OHE, and AHE. In order to disentangle each one, first we measured the PHE using a local spin Hall device. An in-plane magnetic field (3 T) was applied, while an angle scan was performed, as sketched in Fig. 5.8a. The result is shown in Fig. 5.8b. This measurement is composed of the sum of the two contributions, the ISHE and the PHE, which have an angular dependence following $\cos\theta$ and $\sin 2\theta$, respectively.

Since the ISHE signal is measured by applying a magnetic field in the x-axis, the amplitude of the cosine term becomes $2\Delta R_{ISHE}$. On the other hand, in the case of PHE, since the period is 2θ, there is no contribution as a signal in the same measurement. Although a baseline change due to misalignment between the injected current and the magnetic field (phase shift) can appear, it does not modify

the value of $2\Delta R_{ISHE}$ extracted from saturation at positive and negative magnetic fields, as discussed extensively in Ref. [127].

Secondly, the OHE is mainly induced by the stray field (H_{stray}) in the z-axis generated at the tip of the CoFe electrode, as shown in Fig. 5.8c. Since H_{stray} acts strongly up to about 20 nm from the CoFe tip, the simulation was performed considering the misalignment of 20 nm in the 3D FEM model. In an actual device, a misalignment is less than 20 nm, but this was considered in order to not underestimate the contribution. H_{stray} can have both x and z-axis components, and since the current at the junction has a z-axis component, the x-axis component of H_{stray} must also be taken into account. The external magnetic field is also applied in the x-axis, so it is expected to be observed with a slope in the ISHE resistance, but the observed signal is almost flat. Therefore, H_{stray} in x-axis is not considered.

To obtain the Hall coefficient, Hall bars of BiSe (16 nm)/NM (Ti or Pt 10 nm) were prepared, and the Hall effect was observed by applying an out-of-plane magnetic field as shown in Fig. 5.8d. Due to the large resistivity difference between BiSe and NM, most of the current flows through the NM, and the measurement result is totally dependent on NM. The same applies to the local spin Hall device, and since the distance between NM and CoFe changes according to the thickness of BiSe, the OHE also has a thickness dependence. The calculated OHE contribution in the entire thickness range of BiSe does not exceed 0.5 mΩ, and the results are shown together with AHE in Fig. 5.3.

And finally, the AHE presents as an artifact as the potential difference generated in the CoFe wire is transmitted to the NM. Considering the x-axis magnetization, AHE can occur only by the current in z-axis at the junction as shown in Fig. 5.8e. Figure 5.8f is the AHE signal of the CoFe wire, and the anomalous Hall angle (θ_{AH}) is 1.5% when CoFe is 15 nm thick and its resistivity is 42 $\mu\Omega$cm. The AHE contribution decreases with the thickness of BiSe because BiSe acts as a barrier. The 3D FEM simulation results based on the spin diffusion model [34, 123, 127, 203] are shown in Fig. 5.3. As shown in Figs. 5.3e, and 5.3f, the calculated AHE and OHE signals decay with BiSe thickness, since current shunting is suppressed and the distance between FM and NM increases.

In addition, it is possible to reduce the OHE and AHE contributions by changing the design of the device. Since the stray field is proportional to the area of the tip of the FM, making CoFe wire as thin and narrow as possible will minimize the OHE contribution. Extending the tip of the FM beyond the junction area, while isolating

it from the middle arm of the T-structure, is another possibility, but more challenging from the nanofabrication perspective.

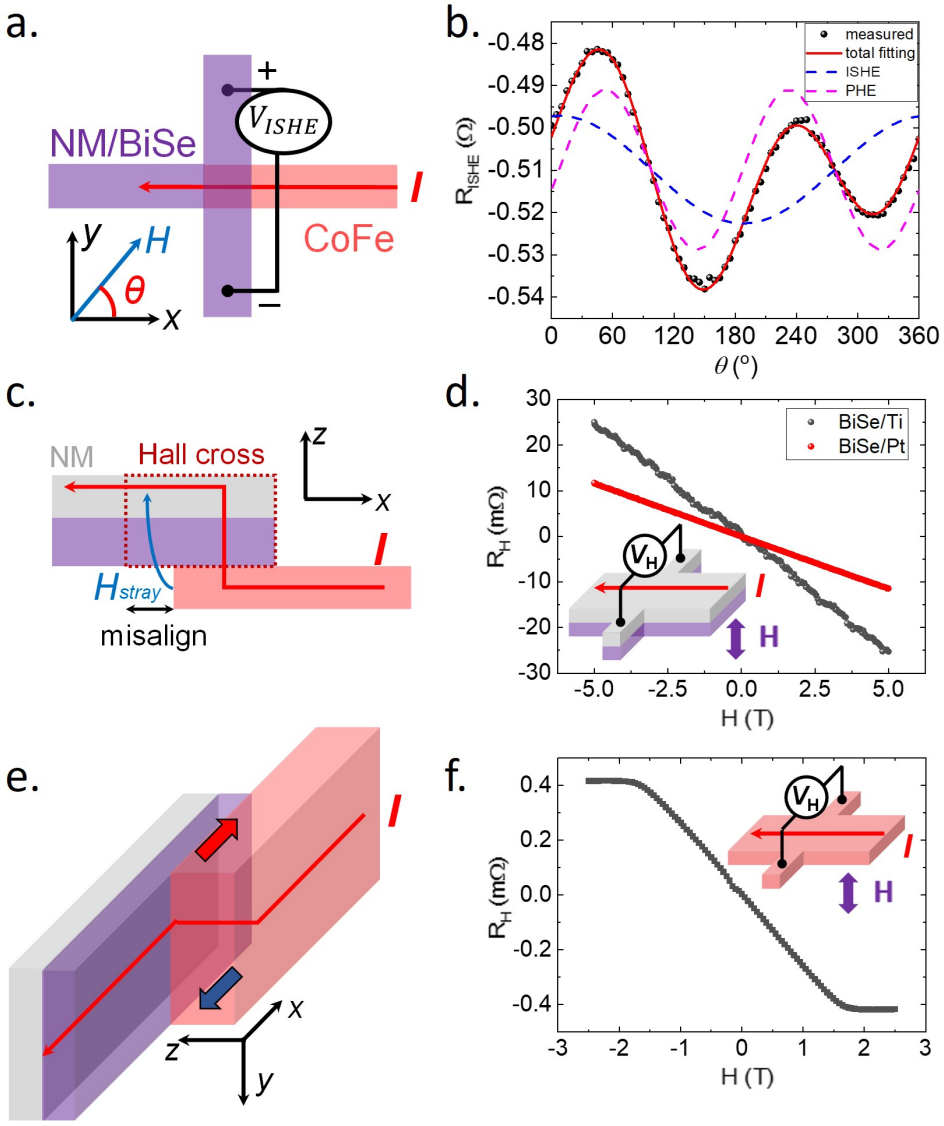

Figure 5.8: Hall effects contributions in a local device. Different contributions are present in a local spin Hall device. Schematics representation and signals of **a**, **b**, planar Hall effect, **c**,**d**, ordinary Hall effect, **e**,**f**, anomalous Hall effect.

In the case of the AHE, previous work by our group [127] showed that the relative thickness of the FM and the SOM can be tuned to completely remove the AHE contribution. The optimal thicknesses will also depend on the resistivity of each material. Inserting a MgO barrier between CoFe and BiSe could also be an effective way to reduce both the OHE and the AHE contributions. In the OHE case, the

MgO barrier plays the role of a spacer, so the stray field at BiSe/NM will decrease. In the AHE case, since the anomalous Hall voltage induced in CoFe will be blocked by the barrier, it will not be transferred to the BiSe/NM wire.

5.6.3 Appendix C: Spin diffusion length of BiSe by the local spin Hall devices

FEM simulations [34, 123, 127, 203] are performed within the framework of the two-current drift-diffusion model, with the collinear magnetization of the FM electrode along the easy axis. The geometry construction and 3D mesh were elaborated using the free software GMSH [176] with the associated solver GETDP [177] for calculations, post-processing, and data flow control.

The fitting parameters of 3D FEM simulation in this model are the spin Hall angle (θ_{SH}^{BiSe}) and the spin diffusion length (λ_s^{BiSe}) of BiSe while spin polarization, anomalous Hall angle and magnetization of CoFe, Hall coefficient of NM and resistivities of wires are fixed parameters. The spin current injected into BiSe will be converted into a transverse charge current (I_{ISHE}) proportional to θ_{SH}^{BiSe} and the amount of local I_{ISHE} will decay with λ_s^{BiSe}, sketched as a red line in Figs. 5.9a and 5.9b. Detailed local current density is shown in Figs. 5.9c and 5.9d. When λ_s^{BiSe} is much shorter than the BiSe thickness, the I_{ISHE} is concentrated near the interface between CoFe and BiSe, so it easily flows back into the CoFe electrode, reducing the ISHE signal which is measured along the BiSe/NM wire. On the other hand, when λ_s^{BiSe} becomes comparable to the BiSe thickness, the distribution of I_{ISHE} over BiSe thickness will span over the entire thickness, increasing the current shunting to the NM layer. Therefore, the measured ISHE signal depends on BiSe thickness and λ_s^{BiSe} as shown in Fig. 5.9e, whereas $\theta_{SH}^{BiSe}$is related to the overall signal magnitude. When λ_s^{BiSe} and BiSe thickness are similar, the signal magnitude is proportional to the resistivity of NM because what we measure is the voltage. Finally, we can simultaneously obtain λ_s^{BiSe} and θ_{SH}^{BiSe} by performing the 3D FEM simulation.

Figure 5.9f shows the result of 3D FEM simulation for ISHE signal in BiSe/Ti local spin Hall device using a BiSe resistivity of $18000\ \mu\Omega$cm. The parameters used for the model are the resistivity of CoFe ($42\ \mu\Omega$cm), Ti ($40\ \mu\Omega$cm), the spin polarization of CoFe (0.48), and the spin diffusion length of CoFe, which is calculated by $\rho_{CoFe} \cdot \lambda_{CoFe} = 1.29\ f\Omega\,\mathrm{m}^2$ (taken from Ref. [75]). Because of such a high resistivity of BiSe, the charge current shunting to the NM layer is highly suppressed in the simulation, thus θ_{SH}^{BiSe} becomes high, 27.5, to compensate for the suppression of this shunting.

λ_s^{BiSe} is estimated to be 0.5 nm, which is 4 times shorter than the thinnest BiSe layer used in our experiment, so we consider that ISHE occurs only in BiSe.

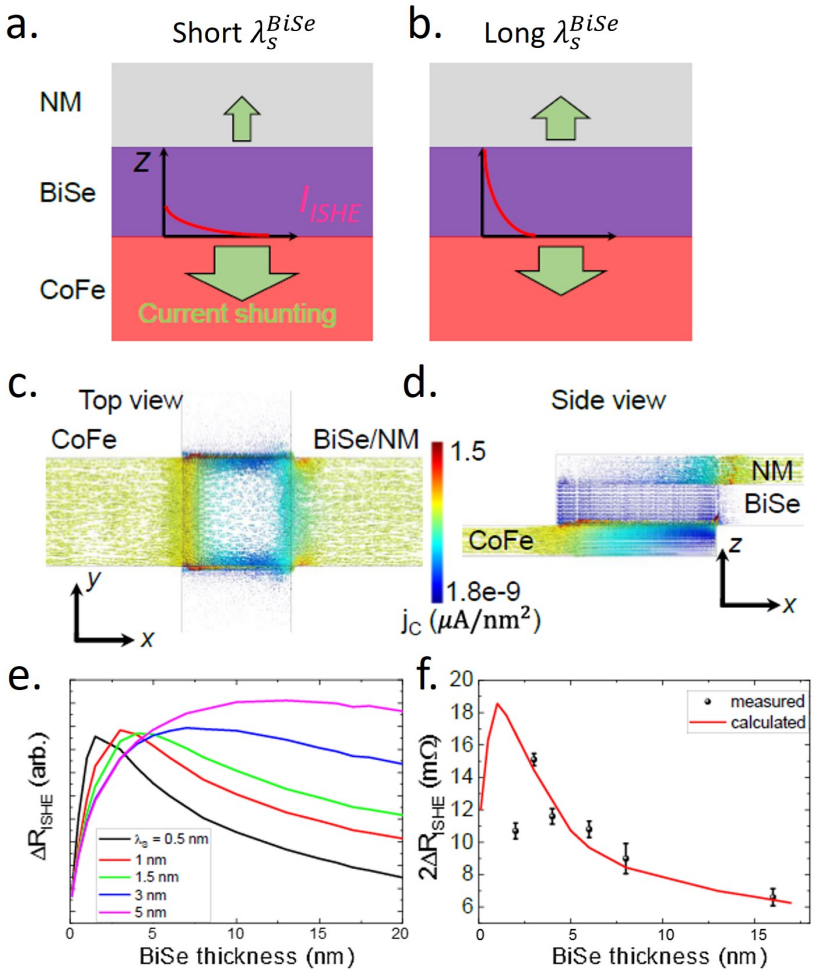

Figure 5.9: Spin diffusion length of BiSe extracted by the local spin Hall devices. Schematic illustration of the shunting of the converted charge current (I_{ISHE}) into the CoFe and NM layers when λ_s^{BiSe} is **a**. shorter than, and **b**. comparable to the thickness of BiSe layer. Local current density obtained from the 3D FEM simulation in **c**. top view, and **d**. side (transversal) view. 3D FEM simulation results of **e**. λ_s^{BiSe} dependence, and **f**. BiSe thickness dependence of ISHE signal observed in BiSe/Ti local spin Hall devices.

On the other hand, the 3D FEM simulation has a limitation. The previous simulation shows the results considering both AHE and OHE, but it was modeled under one important assumption, which is the absence of the intermixed layer. Figures 5.2, 5.5, 5.6 and 5.7 show the intermixing occurring at the interfaces of CoFe/BiSe and BiSe/NM. The intermixed layers are at the CoFe/BiSe and BiSe/Ti interfaces

and are generated mostly by the diffusion of Se atoms. As a result, layers composed of CoFe-Se and Ti-Se are formed, and the Se concentration of BiSe decreases by the amount of Se escaped. The resistivity of BiSe decreases due to the change in the Se concentration, and the resistivity of the intermixed layer is expected to increase.

The local spin Hall device has a CoFe/BiSe/NM structure (two interfaces), but since there is no practical way to obtain all parameters for the 3D FEM model such as resistivity, spin diffusion length, and spin polarization of the interfaces, these interfaces cannot be considered. On the other hand, in general, the higher the interface resistance, the more evenly the current flows through layers, and the shunting of the converted charge current is suppressed. Also, the CoFe/BiSe interface can affect the spin injection efficiency. Formation of the CoFe-Se layer can lower the spin polarization of the FM interface and increase the spin injection efficiency by reducing the spin backflow by increasing the interface resistance. However, considering the high BiSe resistivity, such effects are not expected to be significant.

The presence of the intermixed layers can also affect the resistivity evaluation of each layer. For example, the resistivity of Ti was obtained from a BiSe/Ti bilayer wire, and since BiSe resistivity is much higher than that of Ti, most of the current flows through Ti and the resistivity of the bilayer wire is almost the same as that of Ti. However, this assumption is incomplete because it does not consider intermixed layers which can effectively increase the Ti resistivity as the intermixed layer increase. Since the information regarding their resistivity cannot be obtained experimentally, intermixed layers are not considered in the 3D FEM model.

5.6.4 Appendix D: Grain boundary of BiSe

Figure 5.5 shows that the resistivity of BiSe is changed by the intermixing at the thickness of BiSe below 16 nm. On the other hand, even in the BiSe/Pt structure with limited intermixing, the resistivity of BiSe does not reach the 18000 $\mu\Omega$cm obtained in a long nanowire (inset in Fig. 5.1c), which is thought to be due to the grain boundaries. Figure 5.10a and 5.10b show the R_{CJ} of thicker BiSe in addition to the thickness range plotted in Figs. 5.5a and 5.5b. The R_{CJ} with BiSe thicker than 16 nm deviates significantly from the fitting line and increases more steeply, which means that BiSe resistivity increases.

Figure 5.10c shows a top-view SEM image of the grain structure of a 32-nm-thick BiSe film. The lateral grain size is 15-20 nm (in agreement with the AFM showed in section 3.2.2), and it is expected to have the same dimensions in the growth direc-

tion. Since BiSe has only one grain in the vertical direction below a thickness of 16 nm, R_{CJ} is affected by the resistance inside the BiSe grain. However, above 16 nm, more than one grain is present, therefore boundaries that have higher resistivity are involved in the magnitude of R_{CJ}. The tunneling behavior shown in Fig. 5.10d is sometimes observed in BiSe thickness over 16 nm, and it suggests the presence of a thin insulating layer inside. Note that the applied current for Figs. 5.10a and 5.10b is 10 μA in linear response.

For further verification, the impedance of a 16-nm-thick BiSe wire was measured by applying an alternating voltage of 30 mV in a frequency range from 1 kHz to 10 MHz and presented as a Nyquist plot in Fig. 5.10e. In the case of a uniform conductor, only one arc appears, but as shown in Fig. 5.10e, two arcs are partially overlapped, meaning that BiSe has two resistance components. Fitting was performed with EC-Lab software, and the resulting two resistance values are shown in Fig. 5.10f. Considering the grain size of 15 nm and the thin grain boundary (< 2 nm), the resistance difference of about 2 times causes a big difference in resistivity.

A schematic representation is presented in Fig. 5.10g, which shows why the resistivities measured in the BiSe wire and at the cross-junction are different. A resistance measurement in the wire is done in the lateral direction (V_L), while R_{CJ} is measured in the vertical direction (V_V). In lateral (vertical) direction, grain and grain boundary exist as a series (parallel) resistance when BiSe is thinner than 16 nm, the maximum size of the grain. It explains the factor of 5, the difference between the BiSe wire (18000 $\mu\Omega$cm) and the BiSe/Pt structure (3700 $\mu\Omega$cm).

In this sense, since the grain boundary is much more resistive than the grain, most spin current will flow through the grain and then will be spin-to-charge converted inside, as shown in Fig. 5.10h. The induced voltage is within the grain, not at the grain boundary, which means that even though the obtained resistivity is high due to the grain boundary, the signal magnitude of ISHE is dependent on the resistivity of the grain.

The BiSe resistivity increases due to the grain boundary at thicknesses above 16 nm as shown in Fig. 5.10a and 5.10b. However, since it is also affected by the intermixing, the resistivity varies depending on NM. In the case of the BiSe/Pt structure, the resistivity recovers to that of BiSe wire when it is calculated using the R_{CJ} value, thickness, and junction area. Also, since the grain boundary acts as a shunting barrier, it interferes with the observation of the ISHE signal in the local spin Hall device.

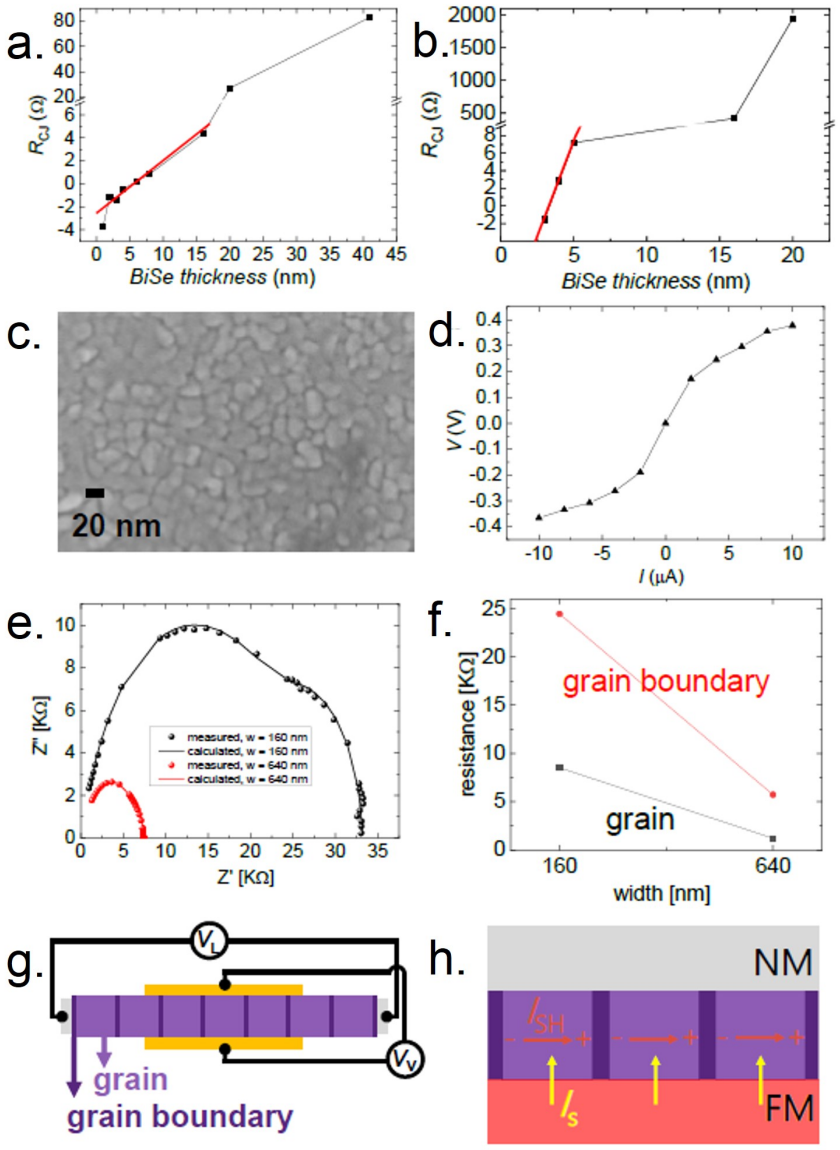

Figure 5.10: Grain and grain boundary of BiSe. Cross junction resistance as a function of BiSe thickness of **a**. BiSe/Ti, and **b**. BiSe/Pt structures. **c**. SEM image of 32-nm-thick BiSe thin film. **d**. Tunneling behavior in 32-nm-thick BiSe junction. **e**. Nyquist plot of impedance analysis on BiSe wire for two different widths (160 and 640 nm) and **f**. two resistance terms as a fitting result. **g**. Schematics of grain and grain boundary with measurement direction, lateral (V_L) and vertical (V_V). **h**. Schematics of the ISHE considering it occurs inside the grains.

Chapter 6

Quantification of spin-charge interconversion in sputtered BiSe with nonlocal spin valves

6.1 Introduction

As mentioned in previous chapters, some works [49–53] reported large SCI at room temperature in polycrystalline Bi_xSe_{1-x} (BiSe) grown by sputtering, a simple technique compatible with industrial processes. Although the Rashba-Edelstein effect is the origin of SCI in ideal TIs, many works use the spin Hall angle (θ_{SH}) to quantify SCI efficiency in this class of materials. Either in this case, or when using a material with SHE, the spin diffusion length (λ_s) is also needed to properly quantify the SCI efficiency. However, λ_s for sputtered BiSe is usually taken from the few reports [47, 57–59] that grow Bi_2Se_3 epitaxially, which shows not only a different crystallinity but also a different composition. Such dissimilarity inevitably leads to inaccuracies in the subsequent quantification of SCI efficiency.

In addition, most techniques for quantifying SCI require the SCI material to be in direct contact with a FM metal or transition metal, but recent work on Bi_2Se_3 reports interdiffusion [55, 56, 198] by solid-state reaction when in contact with metals, which has been confirmed in Chapters 4 and 5. This creates a new layer at the interface through which the spins are injected or pumped, making the quantification of the spin properties (λ_s and θ_{SH}) of this material problematic.

In this Chapter, we characterize sputtered BiSe using the spin absorption technique. Using lateral spin valves (LSVs), we were able to perform two separate measurement configurations [70–73], which allows us to independently quantify the spin diffusion length (λ_s^{BiSe}) and the spin Hall angle (θ_{SH}^{BiSe}) of BiSe.

The use of a nonlocal measurement avoids spurious effects related to local currents, such as Oersted fields in SOT techniques or fringe-field-induced voltages in three-terminal potentiometric techniques [114]. Furthermore, in order to reduce interdiffusion observed in Chapter 5, we grow the metals in contact with the BiSe wire by e-beam evaporation, a gentler deposition technique than sputtering. A much better quality of the device interface is confirmed by TEM and elemental analysis characterization. This information allows us to model our devices and perform a 3D FEM analysis to extract the spin transport parameters at different temperatures. The SCI efficiency, characterized by the $\theta_{SH}^{BiSe}\lambda_s^{BiSe}$ product and equivalent to λ_{IREE} [102], is observed to be up to 0.93 nm (at 100 K), with a value of 0.63 nm at room temperature.

6.2 Experimental details

All LSV devices were fabricated on Si/SiO_2 (150 nm) substrates. Three eBL steps are required for the complete fabrication of the LSVs, following the steps described in Chapter 3. The first step is used to define the FM wires: we spin-coated the substrates with a positive resist (ZEP), patterned it with eBL, deposited 30 nm of Py by e-beam evaporation (base pressure of 2×10^{-9} Torr, rate of 0.6 Å/s) and lift-off. In order to remove possible sidewalls on the wires after lift-off, the sample was Ar-ion-milled with an angle of 10° (with respect to the substrate plane) and an acceleration voltage of 50 V.

The second step defines the BiSe wires: we spin-coated a double layer of PMMA, patterned it with eBL, deposited 10 nm of BiSe by sputtering at room temperature using a target of stoichiometric Bi_2Se_3 (99.999% pure) in a UHV seven target AJA sputtering system at a base pressure of 3×10^{-8} Torr. Bi_2Se_3 was sputtered at 35 W RF power and 3 mTorr Ar pressure to achieve a deposition rate of 0.09 Å/s. The wires were then capped *in situ* with 2 nm of Pt (80 W DC power at 3 mTorr Ar pressure) and lift-off was performed.

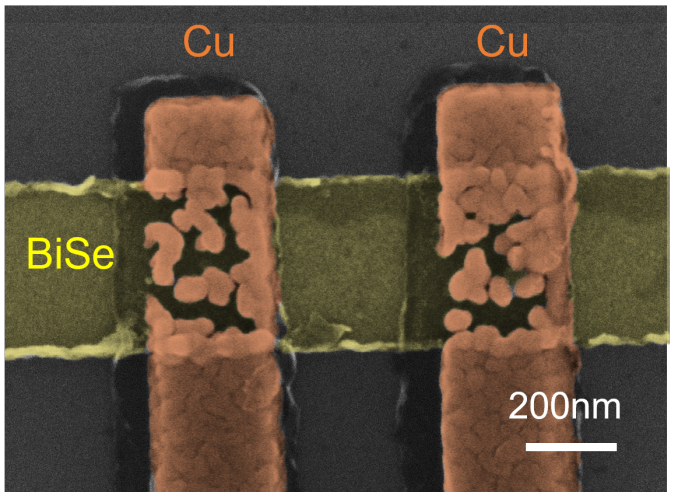

Figure 6.1: Cu growth on BiSe. False-colored SEM image of two 100-nm-thick Cu wires on top of a 30-nm-thick BiSe wire. The image shows clearly how Cu does not grow as a homogeneous layer on top of BiSe but as unconnected islands.

The third step defined the spin transport channel of Cu: we used a double layer of PMMA, patterned it with eBL, and then used Ar-ion milling to remove the Pt cap and clean the surfaces of the Py wires. We then transferred the sample to our UHV evaporation system to grow 2 nm of Ti by e-beam evaporation (at a rate of

0.2 Å/s), followed by 100 nm of Cu *in situ* by thermal evaporation at a rate of 1.5 Å/s. The Ti layer is added to facilitate Cu growth on BiSe (see Fig. 6.1) and acts as an interface between the Cu channel and the Py and BiSe electrodes. Lift-off was then performed. Finally, the entire sample was capped by sputtering 5 nm of SiO_2 (200 W RF at 3 mTorr of Ar).

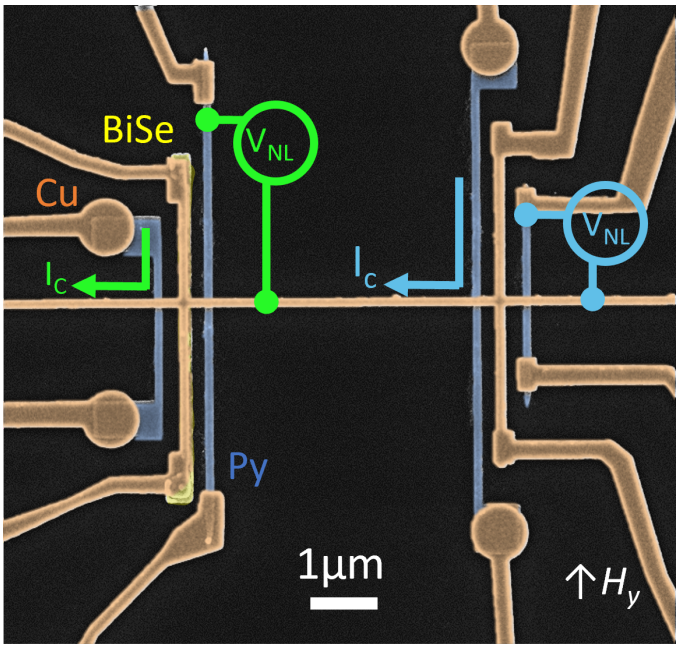

Figure 6.2: Nonlocal spin valves for reference and spin absorption. Top-view false-colored SEM image of the LSV devices with the ferromagnetic Py electrodes (blue) and spin transport Cu channel (orange). The reference device is at the right side, and the device for the spin absorption with the middle wire of BiSe (yellow) is at the left side. The electrical configuration for the absorption measurements is shown in blue (reference configuration) and green (absorption configuration).

6.3 Spin absorption measurements

In a reference LSV without the BiSe wire (right device in Fig. 6.2), a charge current (I_C) is injected from one of the ferromagnetic Py electrodes into the non-magnetic Cu channel, creating a spin accumulation at the interface, as explained in section 2.1.3. These spins diffuse through the Cu channel as a pure spin current (I_s) with a characteristic diffusion length (λ_s^{Cu}) and are detected by the second Py electrode as a nonlocal voltage (V_{NL}).

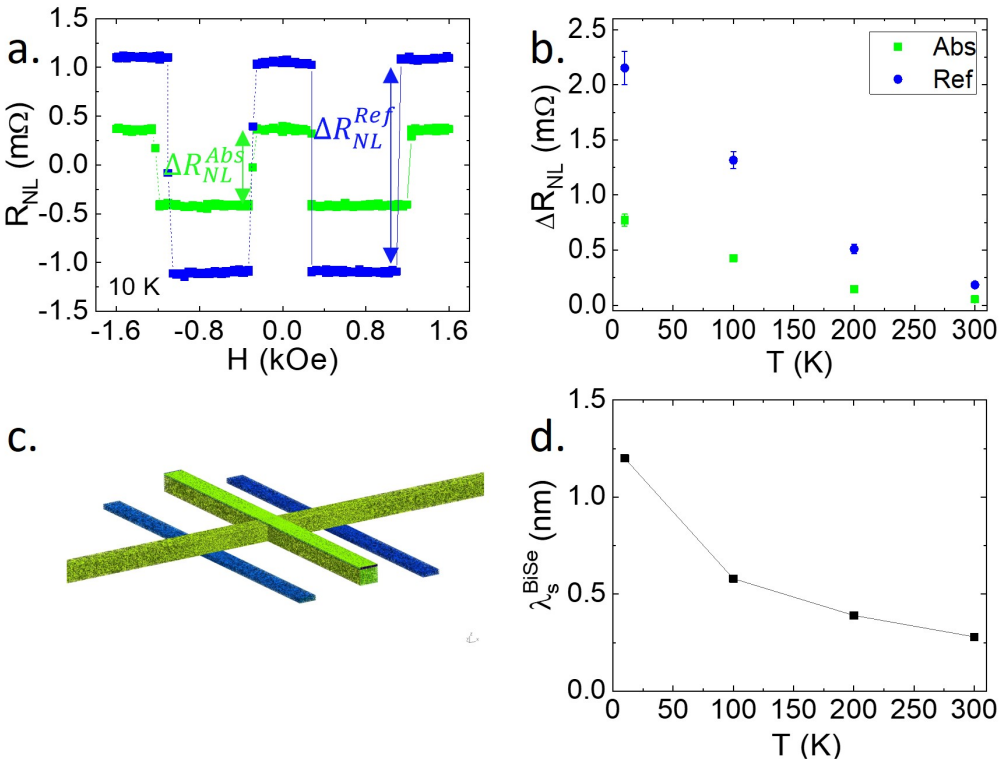

Figure 6.3: Nonlocal spin valves signals and spin diffusion length. a. Nonlocal resistance R_{NL} as a function of the external magnetic field for the reference LSV (blue curve) and LSV with the middle wire (green curve) at 10 K. The corresponding spin signals are labeled. **b.** Spin signals as a function of temperature for the reference LSV and the LSV with the middle wire. **c.** Geometry and mesh of the 3D FEM model. **d.** Spin diffusion length of BiSe, λ_s^{BiSe}, extracted from the data in panel b with a 3D FEM analysis, as a function of temperature. In the 3D FEM simulation, the resistivity of the Ti layer between Cu and BiSe is set to be 50 $\mu\Omega$cm.

The nonlocal resistance, R_{NL}, is defined as the V_{NL} normalized to I_C. An external magnetic field is applied along the easy axis of the ferromagnet ($\pm$ y-direction) to control the reversal of the two Py magnetizations. The value of R_{NL} changes sign when the magnetization configuration of the two Py electrodes switches from parallel (R_{NL}^{P}) to antiparallel (R_{NL}^{AP}). The difference between these two configurations (ΔR_{NL}^{Ref}=$R_{NL}^{P}-R_{NL}^{AP}$) allows us to obtain the spin signal by removing any baseline arising from non-spin related effects.

In a similar LSV device, we place a BiSe wire in the middle of the two Py electrodes (Fig. 6.2), for spin absorption configuration as explained in section 2.1.4. A part of the spin current diffusing along the Cu channel will be absorbed in the BiSe wire and, thus, the spin signal measured by the Py detector, ΔR_{NL}^{Abs}, will be smaller than

ΔR_{NL}^{Ref} (see Fig. 6.3a). The Ti/Cu cross is placed on top of the BiSe wire in order to have better electrical contact due to the high resistivity of this material and to help us to perform spin-to-charge conversion measurements in the same device (see section 6.4).

Figure 6.3b plots the values of ΔR_{NL}^{Ref} and ΔR_{NL}^{Abs} at different temperatures (T) between 10 and 300 K. The decrease of the spin signals with increasing T is expected because λ_s^{Cu} decreases with temperature (as previously reported [209]) and less spin current reaches the FM detector.

To extract the spin diffusion length of BiSe (λ_s^{BiSe}) we performed a 3D FEM simulation. Although, in section 2.1.4, we introduced the 1D spin diffusion model to extract λ_s^{SOM} from spin absorption devices, in our case the BiSe wire is completely shunted by the Cu channel, making the 1D approximation no longer valid. For the 3D FEM simulation:

1. The experimental resistivities for all materials (see Fig. 6.8).

2. The interface spin polarization (α_I) of the Py/Ti and λ_s^{Cu} of the Cu channel, obtained from reference LSVs with different electrode distances (L) by fitting the spin signals ΔR_{NL} vs L using the 1D spin diffusion model (Eq. 2.19), as explained in Chapter 2 and shown in section 6.8.2.

3. The contact resistance of the Py/Ti/Cu interface extracted from an interface resistance measurement with four probe configuration (see section 6.8.3).

4. The measured spin signal after absorption (ΔR_{NL}^{Abs}).

Besides λ_s^{BiSe}, the only unknown parameter in the 3D FEM simulation is the resistivity of the Ti layer (ρ_{Ti}) between Cu and BiSe. Unfortunately, it is not possible to extract exactly the resistivity of this layer due to the design of the electrodes, where the Ti layer is sandwiched between the Cu channel and the BiSe wire. Thus, we estimate this resistivity (50 $\mu\Omega$cm) in a separate experiment (see section 6.8.4).

We extracted λ_s^{BiSe} at different temperatures, plotted in Fig. 6.3d (see section 6.8.5 for details). The value extracted is in all cases of the order or smaller than 1 nm, reaching 0.28 nm at room temperature. This value is much smaller than the values of 1.6 to 6.2 nm reported for epitaxially-grown Bi_2Se_3 [57, 58].

6.4 Spin-charge interconversion on BiSe

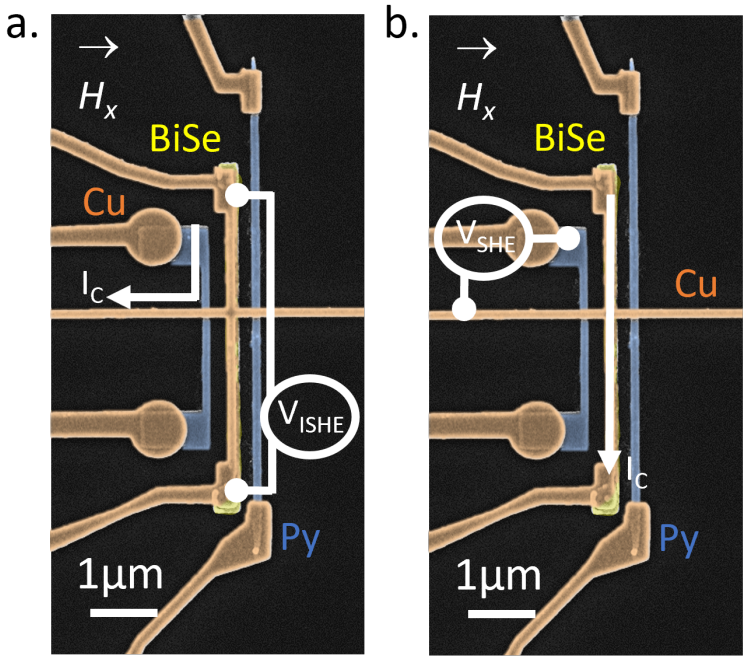

Figure 6.4: Spin-charge interconversion configuration. a. ISHE and **b.** SHE electrical configuration indicated with the white lines.

In the same device where the spin absorption measurement is performed, we also measure the inverse spin Hall effect (ISHE) using the electrical configuration shown in Fig. 6.4a (white lines), as explained in section 2.3.1. This time, we inject a charge current (I_C) from one of the Py electrodes into the Cu channel while applying an in-plane magnetic field along the hard axis of Py (x-direction). An x-polarized spin current is created and reaches the BiSe wire, where it is partially absorbed in the z-direction and converted into a charge current (I_{ISHE}) along the y-direction (Fig. 2.9). This charge current is detected as a voltage (V_{ISHE}) along the BiSe wire (shunted by Cu) under open-circuit conditions. The ISHE resistance (R_{ISHE}=V_{ISHE}/I_c) is measured by sweeping the external magnetic field along x-direction. By reversing the field, the opposite R_{ISHE} is obtained, because the Py magnetization changes direction and, thus, the spin polarization of the spin current. The difference between the two R_{ISHE} values at saturation is denoted as the ISHE signal ($2\Delta R_{ISHE}$) and allows removing any background signal. Indeed, the combination of Seebeck and Peltier effects can give rise to a baseline in the non-local signal because they are linear with the applied current, as explained in Ref. [210]. However, this contribution is removed by taking the difference between the

two values at saturation. Since the material we study is not magnetic, a spurious contribution due to the combination of Peltier effect and anomalous Nernst effect as the one observed in the Weyl ferromagnet Co_2MnGa [211] is not present in our case.

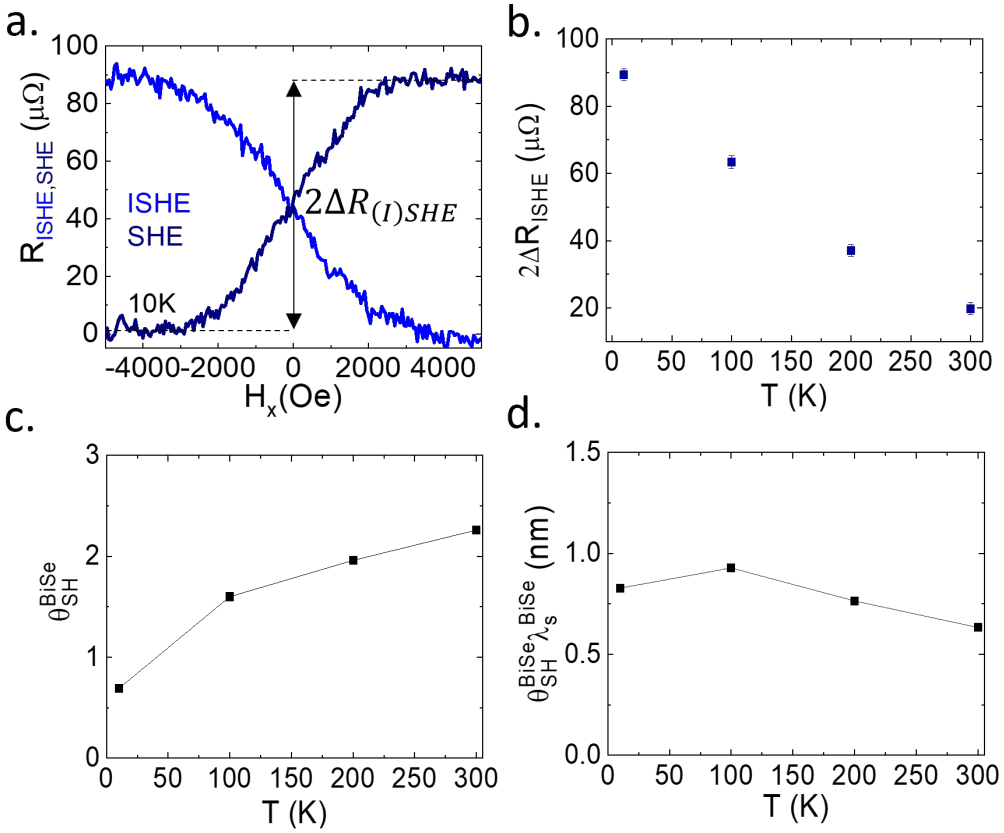

Figure 6.5: Spin-charge interconversion. a. ISHE (R_{ISHE}) and SHE (R_{SHE}) resistances as a function of the external magnetic field at 10 K. **b.** ISHE signal ($2\Delta R_{ISHE}$) as a function of temperature. **c.** Spin Hall angle of BiSe (θ_{SH}^{BiSe}) extracted from the data in panel b and a 3D FEM analysis, considering a Ti resistivity of 50 $\mu\Omega$cm. **d.** $\theta_{SH}^{BiSe}\lambda_s^{BiSe}$ product as a function of temperature.

As shown in section 2.3.1, it is possible to obtain the direct SHE by swapping the current and voltage probes, now by applying the charge current in the BiSe wire and picking up the output voltage between the Py electrode and the Cu channel (see Fig. 6.4b). Both SHE and ISHE resistance curves have the same amplitude but opposite sign [$R_{ISHE}(H)$= $R_{SHE}(-H)$, see Fig. 6.5a], as expected from Onsager's reciprocity [103, 212]. The (I)SHE signals decrease with increasing T, as exposed in Fig. 6.5b. To extract the spin Hall angle (θ_{SH}^{BiSe}), we performed a 3D FEM simulation using the same geometry (dimensions) and material parameters as before,

plus the λ_s^{BiSe} value extracted in the very same device. Figure 6.5c shows the θ_{SH}^{BiSe} values extracted as a function of T, from 0.69 at 10 K to 2.26 at 300 K (see section 6.8.6). These values are more accurate than those previously reported in sputtered BiSe because of the knowledge of λ_s^{BiSe}. As a control experiment, we measure the reference device (without the BiSe) with the direct spin Hall configuration. As expected, no signal is observed (see section 6.8.7).

The product $\theta_{SH}^{BiSe}\lambda_s^{BiSe}$, which is the figure of merit for the efficiency of a MESO device, is shown in Fig. 6.5d as a function of T. $\theta_{SH}^{BiSe}\lambda_s^{BiSe}$ does not change significantly with T, having values between 0.63 and 0.92 nm, slightly higher than the prototypical heavy metals [73, 123, 160, 202].

6.5 Structural characterization

After the magnetotransport characterization (sections 6.3 and 6.4), we characterized the device cross-sections by TEM/STEM imaging combined with EDX analysis with particular emphasis on materials interfaces. Interfaces play a key role in spintronic and spin-orbitronic devices, since they can enhance or reduce the efficiency of the spin current injection in SCI experiments [55, 80, 132, 193–195].

Figure 6.6a shows a cross-sectional view of the LSV. The two Py electrodes (spin injector and detector) can be observed at the right and left of the image with the 10-nm-thick BiSe wire between them. They are covered by a homogeneous 2-nm-thick Ti layer followed by the 100-nm-thick Cu channel. The chemical distribution has been characterized by EDX. Figure 6.6b shows the different elemental maps for the elements of interest obtained by EDX in the region indicated by the orange rectangle in Fig. 6.6a (see section 6.8.8 for complete EDX analysis). The elemental maps evidence that the 2-nm-thick Ti buffer layer is oxidized along all the device. Figure 6.6d shows a higher resolution image of the area in the blue rectangle in Fig. 6.6c: the chemical distribution of Bi and Se within the BiSe wire shows that the two elements are not homogeneously distributed and suggest diffusion has taken place inside the wire. BiSe is a highly reactive material in contact with other metallic materials, creating segregation and inhomogeneity within the material that complicates the quantification of spin transport parameters.

Figure 6.6e shows a high-resolution TEM image of the same wire (red rectangle in Fig. 6.6c), where the polycrystalline and granular structure of the BiSe layer can be

observed. In some grains, alternating Bi_2Se_3 quintuple layers and Bi bilayers are visible, in agreement with the observation in section 5.6.1. The layer of Ti on top of BiSe can be clearly distinguished and shows an amorphous morphology. Since, after Ar-ion milling, the Ti and then the Cu spin transport channel are deposited *ex-situ* by e-beam evaporation, the interface does not show a detectable interdiffusion, in contrast to what is reported by contacting BiSe with transition metals by *in-situ* sputter deposition (Chapters 4 and 5) and molecular-beam-epitaxy-grown Bi_2Se_3 with metallic contacts deposited by e-beam evaporation [56].

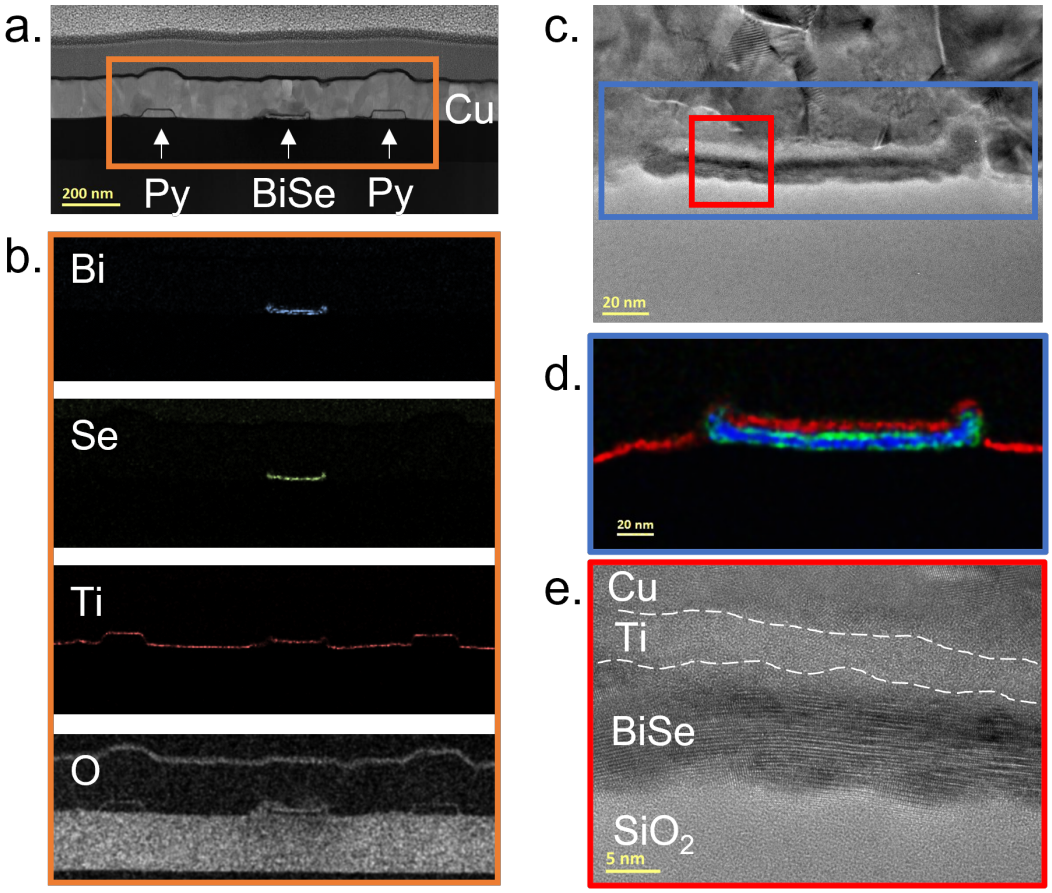

Figure 6.6: Structural characterization by TEM. a. Cross-sectional TEM image of the LSV device. The orange rectangle indicates the area where EDX analysis in panel b is performed. **b.** EDX analysis of the cross section of the LSV, showing the elements of interest in each subpanel: Bi (blue), Se (green), Ti (red), and O (grey). **c.** Cross-sectional TEM image of the BiSe wire inside the LSV. **d.** Color-coded elements image corresponding to the blue rectangle area in panel c. **e.** High resolution TEM image corresponding to the red rectangle area in panel c.

6.6 Oxidized Ti interface layer

In the 3D FEM simulations described in previous section and performed for both spin absorption and spin Hall measurements, we considered a metallic Ti layer with $\rho_{Ti} = 50\ \mu\Omega$cm, a value obtained from our control experiment explained in section 6.8.4. However, as pointed out in the previous section, our EDX analysis shows that the Ti layer in the LSV becomes oxidized.

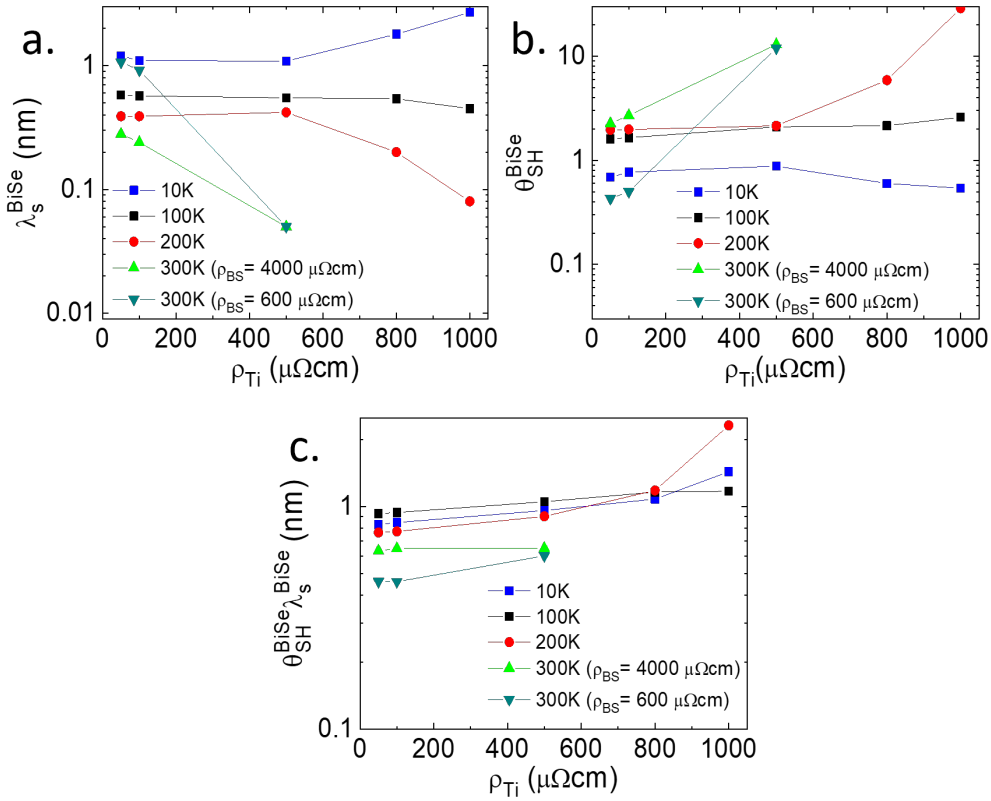

Figure 6.7: Spin diffusion length and spin Hall angle of BiSe considering an oxidezed Ti interface a. Spin diffusion length, λ_s^{BiSe}, **b.** spin Hall angle, θ_{SH}^{BiSe}, and **c.** the $\theta_{SH}^{BiSe}\lambda_s^{BiSe}$ product extracted from the 3D FEM analysis as a function of the Ti resistivity (ρ_{Ti}) at different temperatures, from 10 K up to 300 K. Additionally, at 300 K, we also use a lower resistivity of BiSe reported in Chapter 5.

Therefore, to obtain more accurate values of λ_s^{BiSe} and θ_{SH}^{BiSe}, we need to account for the presence of oxygen by increasing the resistivity of Ti. As mentioned, our device geometry does not allow extraction of the resistivity of the Ti layer in contact with the BiSe, however since the Ti layer also covers the Py electrodes, we were able

to measure the interface resistance at that junction using the four-probe configuration. Taking this value and calculating the resistivity for the 2-nm-thick oxidized Ti layer, we obtained $\rho_{Ti} \approx 1000\ \mu\Omega$cm. The same material will grow differently on different materials and, therefore, we cannot directly assume that the resistivity of Ti on Py will be the same as that of Ti on BiSe, but we can take it as an upper limit.

Repeating the 3D FEM simulation with ρ_{Ti} values from 50 to 1000 $\mu\Omega$cm we extracted λ_s^{BiSe} as a function of ρ_{Ti}, which is plotted in Fig. 6.7a. At 10 K, for example, λ_s^{BiSe} varies between 1.1 and 2.7 nm. In order to rule out higher resistivities of the Ti layer, we also performed a simulation using $\rho_{Ti} = 1500\ \mu\Omega$cm. In this case, λ_s^{BiSe} tends to infinity, that is, fewer spins can reach the BiSe layer, rendering the properties of this second layer irrelevant in the 3D model.

We also performed a simulation considering the BiSe resistivity measured in the vertical direction (across the thickness) at 300 K as is shown in Chapter 5 ($\rho_{BiSe} = 600\ \mu\Omega$cm), a much lower value compared to the longitudinal measured at room temperature ($\rho_{BiSe} = 4100\ \mu\Omega$cm, see Fig. 6.8c). Comparison of the extracted λ_s^{BiSe} for the simulations using longitudinal values of ρ_{BiSe} (see Fig. 6.7a, blue, black, red and light green curves) shows λ_s^{BiSe} to be relatively small in all cases, and to decrease with increasing temperature for any ρ_{Ti}. However, comparing λ_s^{BiSe} at room temperature (light green and dark cyan curves) and ρ_{Ti} lower than 100 $\mu\Omega$cm, we find that the low BiSe resistivity value (~ 6 times smaller) yields a spin diffusion length more than three times larger than the one obtained using the longitudinal higher value ($\rho_{BiSe} = 4100\ \mu\Omega$cm).

We additionally performed a 3D FEM simulation to extract the conversion efficiency (θ_{SH}^{BiSe}), using now the new values of λ_s^{BiSe} for each value of ρ_{Ti} from 50 to 1000 $\mu\Omega$cm. Our simulation results for θ_{SH}^{BiSe} as a function of ρ_{Ti} are plotted in Fig. 6.7b. As an example, the value at 10 K varies between 0.54 and 0.88. We also performed the simulation considering $\rho_{BiSe} = 600\ \mu\Omega$cm at 300 K. Finally, the product $\theta_{SH}^{BiSe}\lambda_s^{BiSe}$ as a function of ρ_{Ti} is shown in Fig. 6.7c. Interestingly, this product does not present large variations with the resistivity of the interface layer, being fairly constant and generally lower than 1 nm. This indicates the robustness of this figure of merit in our analysis independently of the assumed resistivity of the interfacial Ti. Table 6.1 summarizes our results, taking the minimum and maximum values of these parameters for each temperature. Results from Chapters 5 and previous reports on sputtered BiSe are also included for comparison.

Table 6.1: Summary of ρ_{BiSe}, λ_s^{BiSe}, θ_{SH}^{BiSe}, λ_{IREE} and the method used in this thesis (Chapter 5 and 6) and previous reports on sputtered BiSe with the temperature.

Sample	t_{BiSe} (nm)	T (K)	ρ_{BiSe} ($\mu\Omega$cm)	λ_s^{BiSe} (nm)	$\theta_{\text{SH}}^{\text{BiSe}}$	λ_{IREE} (nm)	Method
BiSe	10	10	6200	1.09-2.70	0.54-0.88	0.82-1.46[a]	LSV (chapter 6)
		100	5900	0.45-0.58	1.60-2.61	0.92-1.17[a]	
		200	5100	0.08-0.39	1.96-28.90	0.76-2.31[a]	
		300	4100	0.05-0.28	2.26-13.01	0.63-0.65[a]	
		300	600[b]	0.05-1.07	0.43-11.99	0.46-0.60[a]	
BiSe/Ti	2-16	300	600	0.5	0.45	0.225[a]	Local device (chapter 5)
BiSe/Pt	3-5	300	3700	0.35	3.2	1.12[a]	
BiSe/CoFeB	4-40	300	12820	-	18.62	-	Harmonic Hall [49]
BiSe/YIG	4-16	300	-	-	-	0.11	Spin pumping [51]
BiSe/CoFeB	2-16	300	-	-	-	0.32	Spin pumping [50]
BiSe/Py	5-10	300	1000000	-	75	-	ST-FMR [207]
BiSe/Co	3-15	300	890	-	0.35	-	Harmonic Hall [208]

[a] $\lambda_{IREE}=\theta_{SH}^{BiSe}\lambda_s^{BiSe}$. [b] Resistivity taken from chapter 5

6.7 Summary and conclusions

We successfully injected a pure spin current into highly resistive sputtered BiSe using nonlocal spin valves and performed spin absorption measurements from 10 K up to room temperature. A 3D FEM analysis of the absorption data allowed us to extract the spin diffusion length λ_s^{BiSe} in this system for the first time. Spin-charge interconversion measurements were performed on the same device to extract the spin Hall angle, θ_{SH}^{BiSe}. From these two experiments,

we were able to reliably obtain the $\theta_{SH}^{BiSe}\lambda_{s}^{BiSe}$ product, a relevant figure of merit characterizing SCI in MESO devices. Despite the uncertainty regarding the resistivity of the Ti layer separating the Cu spin channel and the sputtered BiSe, the obtained values, generally lower than 1 nm, are robust. Although existing literature has reported a high SCI efficiency for BiSe and put this material forward as a promising candidate for MESO logic devices, our work shows otherwise. A more accurate characterization, relying on nonlocal devices that eliminate spurious effects, allows us to unveil that the SCI efficiency of BiSe is in fact too small to be used for MESO technology.

6.8 Appendices

In this section, complementary data to support our results in previous sections are added.

6.8.1 Appendix A: Electrical characterization

We extracted the resistivities of 100-nm-thick Cu and 30-nm-thick Py in the very same device of the LSVs, and are plotted in Figs. 6.8a and 6.8b, respectively. In a separated Hall bar nanostructure, we measured the resistivity of 10-nm-thick and 120-nm-wide BiSe (same dimensions used in the LSVs), see Fig. 6.8c, and extracted the 3D carrier concentration (see Fig. 6.8d).

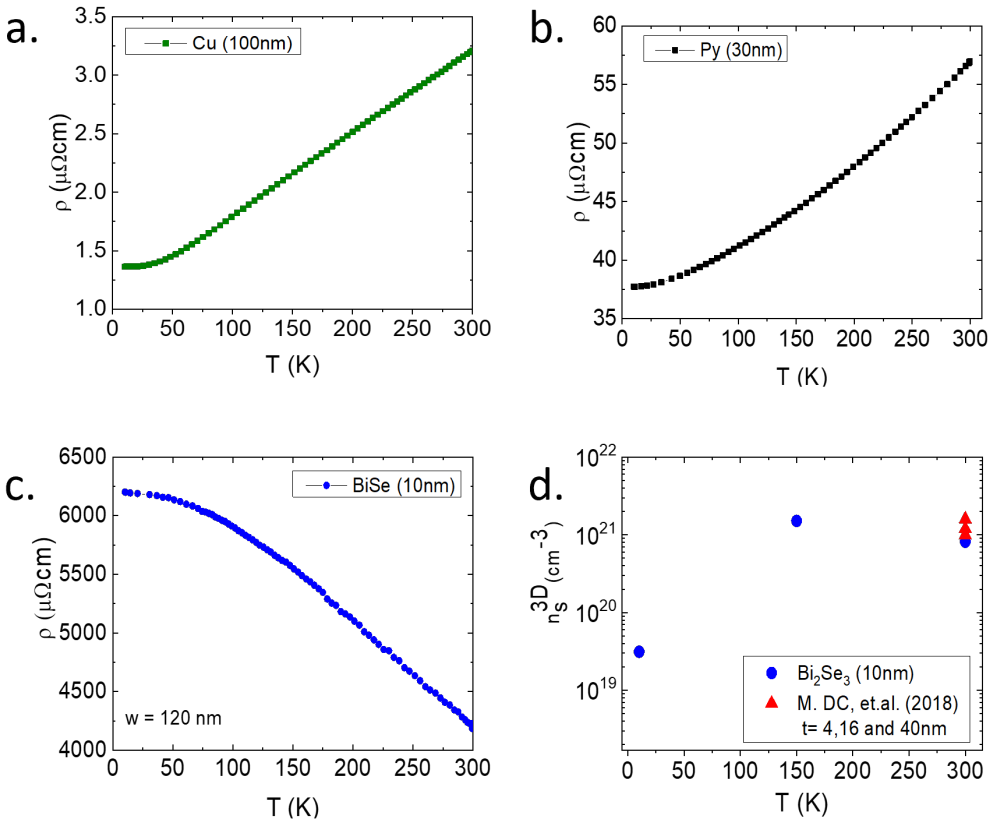

Figure 6.8: Resistivities. Resistivity as a function of temperature for **a.** Cu (100 nm thick) and **b.** Py (30 nm thick). **c.** Resistivity as a function of temperature for a 10-nm-thick and 120-nm-wide BiSe wire, measured performed in a separated device (without the Cu at the top). **d.** 3D carrier concentration, determined by Hall measurements, for BiSe (10 nm thick). Results from Ref. [49] are included for comparison.

6.8.2 Appendix B: Dependence of the spin signal on the inter-electrode distance

In order to extract the spin diffusion length of Cu (λ_s^{Cu}) and the interface spin polarization (α_I) of Py/Ti/Cu, on the same Si/SiO_2 chip as that containing the devices presented previously, but in a separate device (to guarantee the same experimentally conditions), we fabricated lateral spin valves (LSVs) with different Py electrode distances, as shown in Fig. 6.9a.

The experimental spin signals (ΔR_{NL}) decrease as both L and T increase. The ΔR_{NL} obtained as a function of L are fitted following the 1D spin diffusion model (Eq. 2.19) for each temperature, from which α_I and λ_s^{Cu} is obtained.

The rest of parameters appearing in Eq. 2.19 are known (dimensions and resistivities). The spin polarization of Py (α_{Py}) and the spin diffusion length of Py (λ_s^{Py}), are taken from Ref. [70]. The interface resistance (R_I) is extracted as explained in the following section.

6.8.3 Appendix C: Interface resistance

We performed 3D FEM simulations to extract the interface resistance, R_I, at the Py/Ti/Cu junction using *Comsol multiphysics*. We extracted R_I by adjusting this resistance in the interface area ($R_I A_I$, where $A_I = 5.0 \times 10^{-14}$ m^2) using the FEM calculation to reproduce the experimentally measured resistance R_{meas}. In this simulation, we considered that Ti is not an extra layer but an interface and the resistivities of Cu and Py wires presented in Figs 6.8a and 6.8b, respectively.

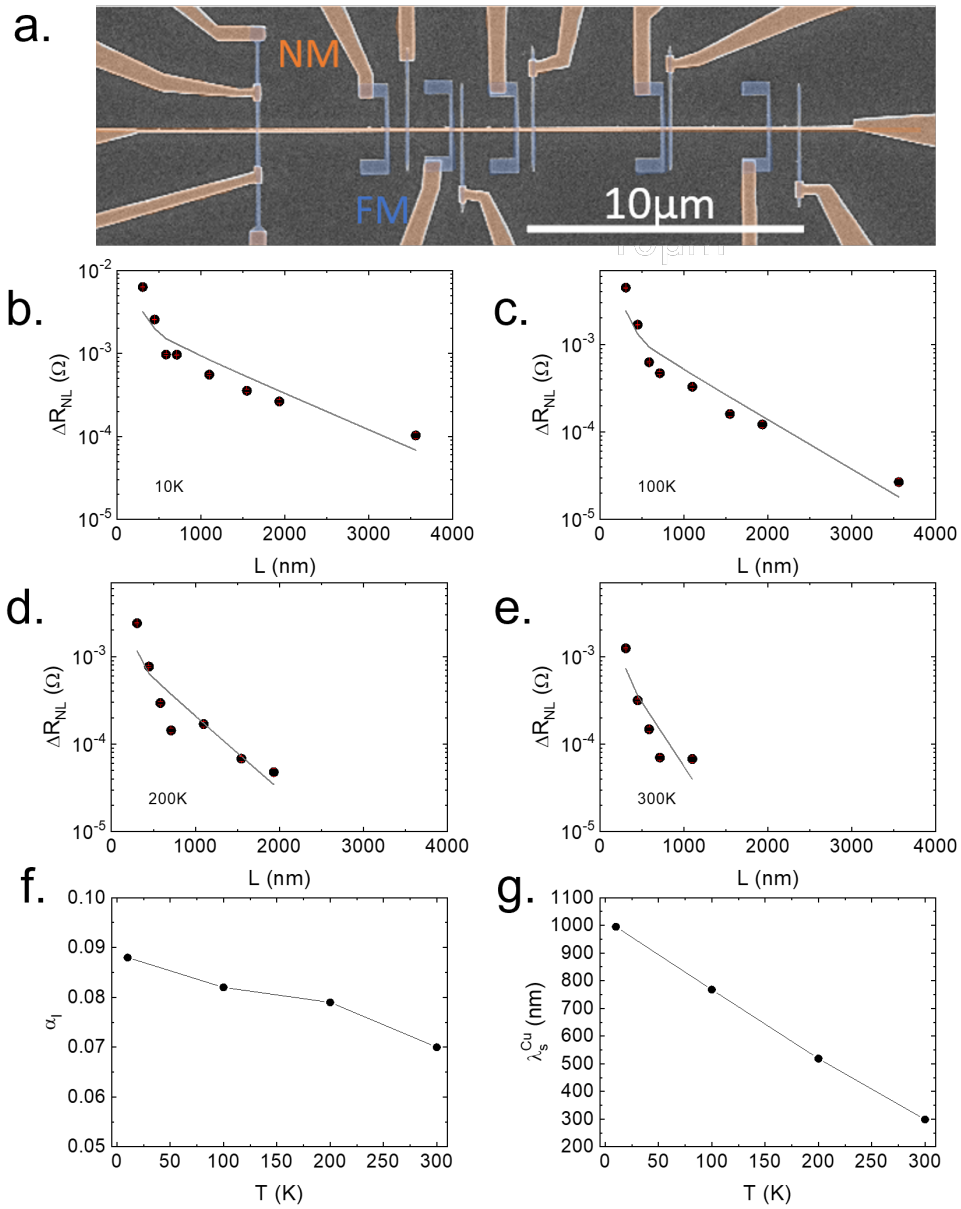

Figure 6.9: Dependance of the spin signal on the inter-electrode distance. a. SEM image of LSVs with different distances between FM electrodes (L). FM (Py) electrodes are false-colored in blue and the NM (Cu) spin transport channel in orange. A 2-nm-thick Ti layer is used between the Py and the Cu. The spin signal ΔR_{NL} as a function of L at **b.** 10 K, **c.** 100 K, **d.** 200 K, and **e.** 300 K. Black circles are the experimental data (error bars are smaller than the symbol size) and solid grey lines are the fit to Eq. 2.19. **f.** Interface spin polarization (α_I) and **g.** spin diffusion length of Cu (λ_s^{Cu}) extracted from the fit at different temperatures.

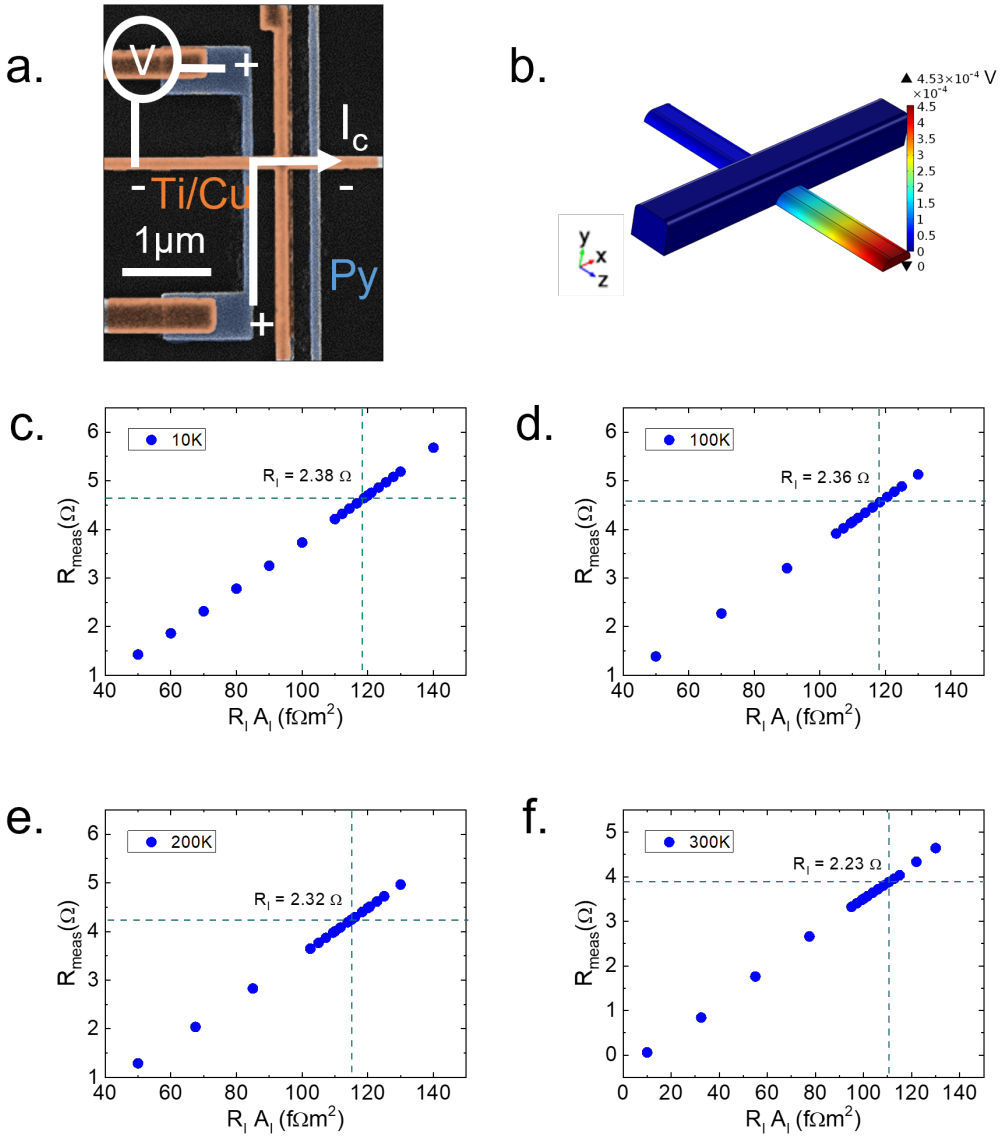

Figure 6.10: Interface resistance Py/Ti/Cu. a. SEM image of the LSV devices presented in this chapter (Fig. 6.2) with the four-point electrical configuration to extract the interface resistance of Py/Ti/Cu (in the injection or detection area, both considered equal). **b.** 3D FEM simulation model presenting the geometry and the electrical potential driven by the applied current to extract the interface resistance (R_I) at **c.** 10 K, **d.** 100 K, **e.** 200 K, and **f.** 300 K.

6.8.4 Appendix D: Ti resistivity

To extract the resistivity of the Ti layer on top of the BiSe, we fabricated a set of BiSe/Ti/Au stacks, varying the Ti thickness ($t_{Ti} = 1, 2, 3, 4$ and 5 nm, the sketch is shown in the inset of Fig. 6.11), keeping the BiSe thickness constant ($t_{BiSe} = 10$ nm), and adding Au as a capping layer ($t_{Au} = 3$ nm). The stacks are patterned as Hall bars (width $w = 100$ nm and length $L = 800$ nm) to measure the total resistance (R_{Tot}), whose inverse is plotted as a function of t_{Ti} in Fig. 6.11. By applying the parallel resistance model:

$$\frac{L}{wR_{Tot}} = \frac{t_{BiSe}}{\rho_{BiSe}} + \frac{t_{Ti}}{\rho_{Ti}} + \frac{t_{Au}}{\rho_{Au}} \tag{6.1}$$

where $\rho_{(Ti,BiSe,Au)}$ corresponds to the resistivity of Ti, BiSe and Au, we can extract the resistivity of the Ti layer from the linear slope of the data in Fig. 6.11. The result for 1-nm-thick Ti is not taken into account for the fitting, as clearly lies outside of the straight line. This might indicate that Ti does not grow uniformly at this thickness.

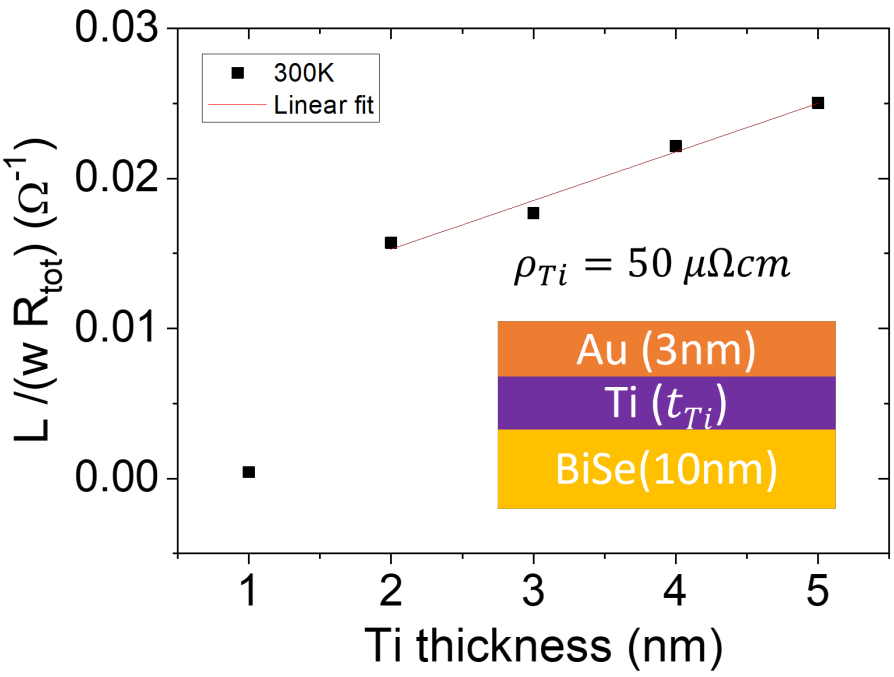

Figure 6.11: Ti resistivity. Inverse of the total resistance of the BiSe (10 nm)/Ti (t_{Ti})/Au (3 nm) stack as a function of the Ti thickness. Inset: Sketch of the stack. Measurements performed at 300 K.

6.8.5 Appendix E: 3D FEM simulation to extract the spin diffusion length of sputtered BiSe

To extract the spin diffusion length of BiSe (λ_s^{BiSe}), we simulated the spin absorption measurements (ΔR_{NL}^{abs}) at 10 K, 100 K, 200 K, and 300 K by using a 3D FEM based on the two-current drift-diffusion model.

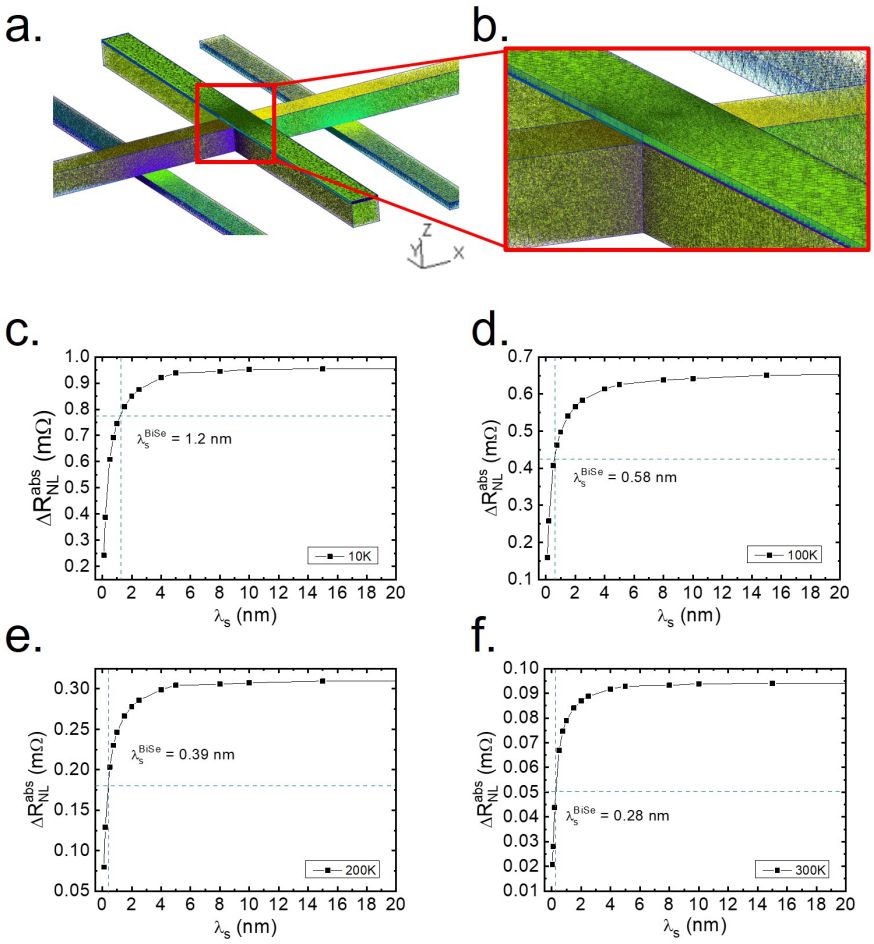

Figure 6.12: Spin diffusion length of BiSe. a. Geometry of the simulated device and the mesh of the finite elements and **b.** zoom on the 10-nm-thick BiSe wire with the 2-nm-thick Ti (purple) and 100-nm-thick Cu layers at the bottom. 3D FEM analysis output to extract the spin diffusion length of BiSe (λ_s^{BiSe}) considering a ρ_{Ti} of 50 $\mu\Omega$cm at **c.** 10 K, **d.** 100 K, **e.** 200 K, and **f.** 300 K.

Figures 6.12a and b show the geometry of the simulated device (the actual device can be seen in Fig. 6.2) and the mesh of the finite elements. The geometry construction and 3D-mesh were elaborated using the free software GMSH [176] with

the associated solver GETDP [178, 179, 181] for calculations, post-processing and together with a Phyton code to data flow controlling. Input parameters were taken from the resistivity characterization of each material shown in Fig. 6.8, λ_s^{Cu} and α_I extracted as shown in section 6.8.2, and interface resistance of the Py/Ti/Cu junction extracted as shown in section 6.8.3. The resistivity of the 2-nm-thick Ti layer between Cu and BiSe wires was estimated from the control experiment described in section 6.8.4. λ_s^{Ti} was calculated assuming the Elliott-Yafet mechanism for spin relaxation ($\rho_{Ti}\lambda_s^{Ti}$ = cnt.) and taking the constant from Ref. [201] ($\lambda_s^{Ti} = 13.3$ nm for $\rho_{Ti} = 300$ $\mu\Omega$cm). We simulated the spin absorption experiment by adjusting λ_s^{BiSe} in the FEM calculation to reproduce the experimental spin signal in the absorption device (ΔR_{NL}^{abs}, shown in Fig. 6.3a). The simulation is repeated for the experimental ΔR_{NL}^{abs} values at each temperature (shown in Fig. 6.3b). The output results are shown in Figs. 6.12c-f.

6.8.6 Appendix F: 3D FEM simulation to extract the spin Hall angle of sputtered BiSe

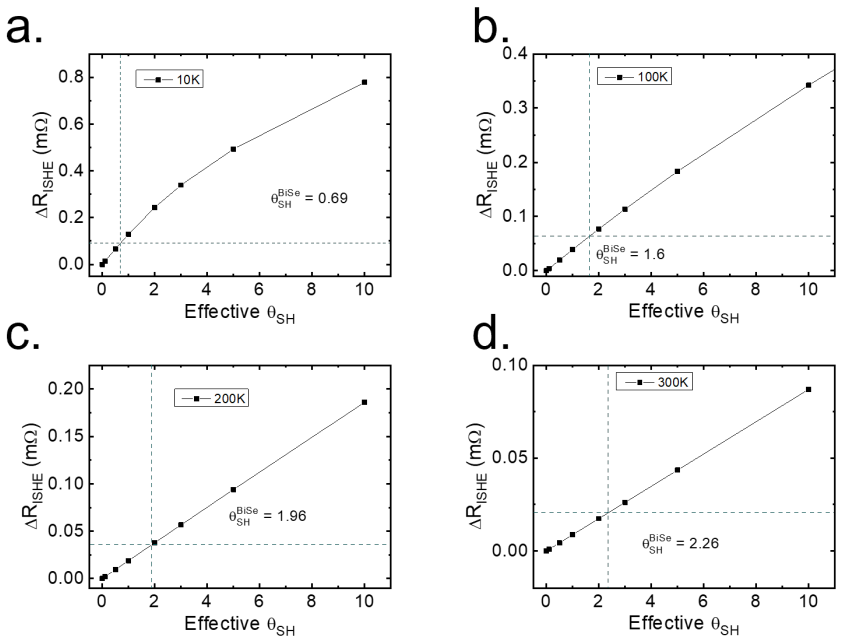

Figure 6.13: Spin Hall angle of sputtered BiSe. 3D FEM analysis output to extract the spin Hall angle of BiSe (θ_{SH}^{BiSe}) considering a ρ_{Ti} of 50 $\mu\Omega$cm at **a.** 10 K, **b.** 100 K, **c.** 200 K, and **d.** 300 K.

To extract the spin Hall angle of BiSe (θ_{SH}^{BiSe}), a 3D FEM simulation is performed in a similar manner as the one in section 6.8.5 but for the spin-to-charge conversion measurements (ΔR_{ISHE}) at 10 K, 100 K, 200 K, and 300 K. Since we use the same device as for spin absorption, the geometry is the same, but the electrical contacts are changed (see Fig. 6.4). Also, the model is designed taking into account the length of the electrodes, to be long enough in such a way that have more than 3 times the spin diffusion lengths in the materials, and much longer than the widths of the electrode such that the spin current vanishes at their ends, in the case of the ISHE configuration. Moreover, the mesh size in the vicinity of the interface is set smaller in such a way that is possible to ensure that the SOM-based effects are calculated properly, this is the area where the spin-to-charge current conversion takes place. Then, by adjusting the effective spin Hall angle, θ_{SH}^{eff}, in the simulation to reproduce the experimental value ($\Delta R_{(I)SHE}$, shown in Fig. 6.5) and using the same input parameters as in section 6.8.5 and the obtained value of λ_s^{BiSe} (presented in section 6.8.5 and shown in Fig. 6.3d), we obtained θ_{SH}^{BiSe} for each temperature. The output results are shown in Fig. 6.13.

6.8.7 Appendix G: Control experiment for spin-charge interconversion measurements

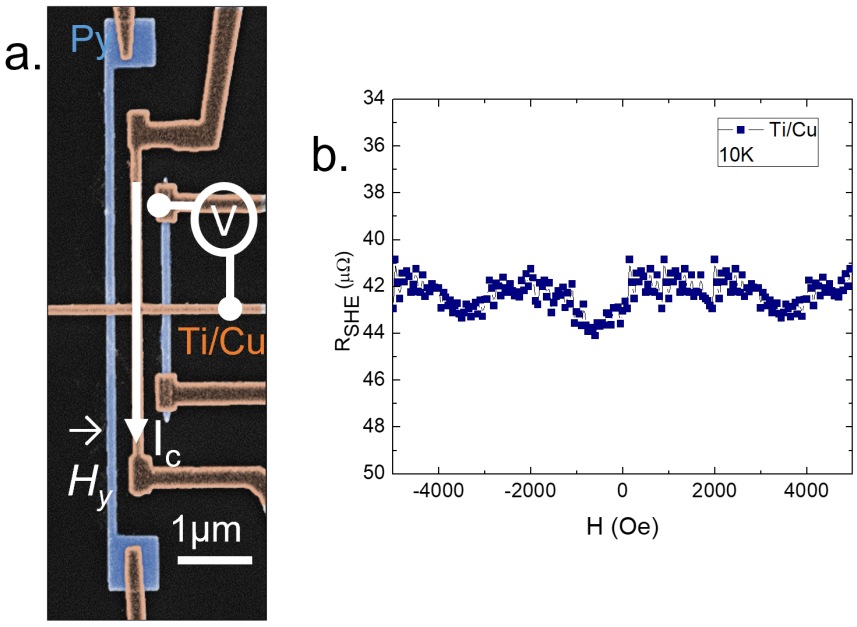

Figure 6.14: Control experiment of spin-charge interconversion measurement. a. Top-view SEM image of the reference LSV with the electrical configuration for the SHE measurement. **b.** SHE resistance in Ti/Cu as a function of the external magnetic field at 10 K, measured with the configuration shown in panel a.

We performed a control spin-charge interconversion experiment in the reference device (i.e., without the BiSe wire at the bottom of the Ti/Cu cross). In such reference device, no spin-charge interconversion is expected. The experiment is performed in the same conditions as in the devices with the BiSe wire. The control experiment consists in injecting a charge current directly in the cross of Ti (2 nm)/ Cu (100 nm), while reading the voltage between the Py electrode and the Cu channel and applying the magnetic field in the hard axis of the Py electrode. Figure 6.14 displays the SHE resistance as a function of the magnetic field. No SHE signal is observed above the $\sim 5\ \mu\Omega$ noise level, meaning that the presence of SHE is negligible.

6.8.8 Appendix H: Structural characterization

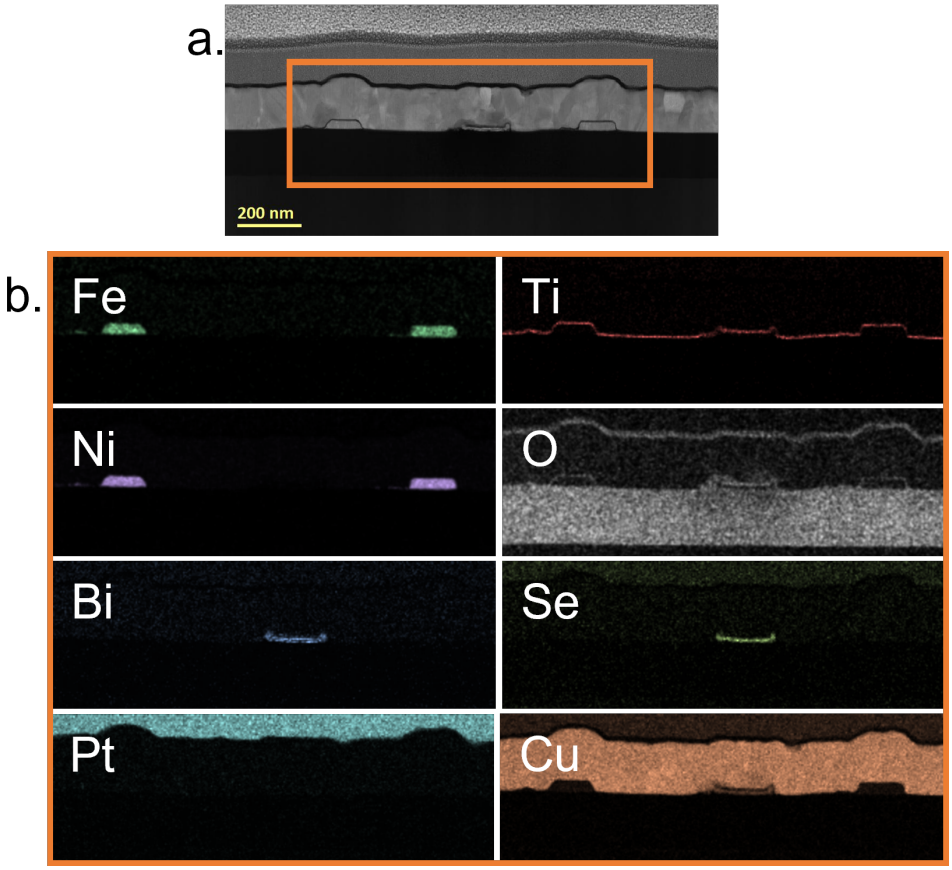

Figure 6.15: Structural characterization by TEM. a. Cross-section TEM image of the LSV used in this work. **b.** EDX analysis for each relevant element present in the sample, performed in the area marked with an orange box in panel a.

We performed a cross section cut to study the interfaces by TEM and EDX in the very same device where we performed the spin absorption and the spin Hall measurements. With the EDX elemental analysis, it is possible to clearly observe the Ti layer (2 nm) in between the BiSe wire (10 nm) and the Cu channel (100 nm), as well as the presence of oxygen in the Ti layer. The detailed results are shown in Figs. 6.15 and 6.16.

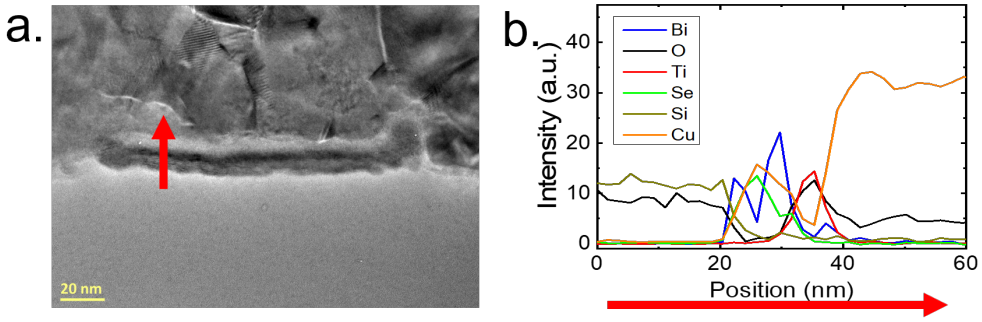

Figure 6.16: High-resolution TEM and elemental profile. a. High-resolution TEM image of the BiSe wire region. **b.** Elemental profile through the BiSe wire. The red arrow represents the scanning direction (also labeled in panel a), from the substrate (Si/SiO_2) to the top of the sample (Ti/Cu).

Chapter 7

Charge-to-spin conversion in sputtered BiSe/graphene heterostructure by nonlocal spin injection

7.1 Introduction

In the previous chapters, we focused on characterizing and understanding the role of interfaces for a more accurate quantification of the spin transport properties of BiSe. We found that BiSe is highly reactive in contact with other transition metals, forming a new layer at the interfaces of the spintronic devices. In Chapter 4, the strong interdiffusion on the spin pumping devices did not allow us to quantify the spin transport parameters of BiSe. In Chapter 5, we improved the quality of the FM/BiSe interface on the T-shaped devices for local spin injection. However, it was necessary to add a NM (Ti or Pt) layer on top of the BiSe T-shaped electrode to improve the signal-to-noise ratio. This top layer changed the stoichiometry of BiSe and, thus, its resistivity and SCI efficiency. This was especially severe in the case of Ti, which also showed interdiffusion with BiSe. The resulting interdiffusion identified in both chapters affected the output we measured in the different configurations and thus complicated the quantification of the spin transport properties.

Furthermore, in Chapter 6, we successfully reported a more accurate estimation for the spin transport parameters of BiSe using nonlocal spin injection with metallic LSVs. However, a seed layer of Ti was needed for a proper Cu growth on top of BiSe. To reduce the interdiffusion and improve the interface quality with Ti, we changed the deposition technique to e-beam evaporation, instead of sputtering. With this, the only unknown parameter is the resistivity of the seed layer (ρ_{Ti}).

In an effort to suppress this interdiffusion between BiSe and the metal contacts, and also avoid the use of the Ti layer to grow Cu on top of BiSe, we propose the use of LSV, but replacing the metallic spin transport channel (Cu) with a few layers of graphene. This graphene channel not only avoids interdiffusion [213] at the junction with the BiSe, but also has a higher resistivity (compared to the metallic Cu channel), which is an advantage to reduce the shunting factor and increase the output signal.

In this Chapter, we fabricate sputtered BiSe LSVs with few-layer graphene as spin transport channel. Nonlocal charge-to-spin conversion (CSC) signals are successfully measured in the LSVs. Interestingly, when measuring the spin current, we detect simultaneous contributions originating from three different spin polarization directions. This phenomenon has been previously observed in graphene-based van der Waals heterostructures where the symmetries are reduced [112–115], suggesting that sputtered polycrystalline material leads to the same symmetry reduc-

tion in graphene. Although this is an unexpected result, it could open up new possibilities in the design of novel spintronic devices, which would benefit from flexible configurations to generate, detect and control spin currents.

7.2 Experimental details

To fabricate the LSV with graphene, we first mechanically exfoliated HOPG with a tape [163] and transferred the desired material (flakes) to the surface of clean Si/SiO_2(300 nm) substrates, as explained in section 3.1.5. After the transfer, we scanned the flakes with an optical microscope to find the flake with the shape and dimensions needed for the LSV, see Fig. 7.1a.

After the flake is selected, we spin-coat the sample with double layer PMMA to add structural references (crosses in Fig. 7.1b) by eBL, which allows us to align the flake for further lithography steps. Next, we pattern the metallic contacts on the graphene flake and deposit Ti(5 nm)/Au(45 nm) as shown in Fig. 7.1c.

Subsequently, we spin-coat again with double layer PMMA to continue with the third lithography step to pattern the BiSe wire (Fig. 7.1d), grow the 30-nm-thick BiSe by sputtering with the same conditions reported in previous chapters, and cap it with SiO_2 (5 nm) *in situ* (same sputtering conditions as in Chapter 6), followed by the lift-off process.

Afterwards, the metallic contacts for the BiSe are patterned by eBL. After development, we Ar-ion mill the SiO_2 capping layer with the help of the mass spectrometer and immediately transfer the sample to the evaporation chamber to grow Ti (5 nm)/Au (45 nm), followed by lift-off process (see Fig. 7.1e).

The fifth and final lithography step is used to pattern the ferromagnetic electrodes. After development, we grow by e-beam deposition 3 Å of Ti, let it oxidize by air, and then grow 35-nm-thick Co capped *in situ* by thermal deposition of 5-nm-thick Au (Fig. 7.1f), followed by the lift-off process.

When the sample is ready after the five lithography steps, depositions, lift-offs, and Ar-ion milling processes, we contact it with Al wire using a wire bonder at low power conditions. To contact the back-gate, we carefully scratch the SiO_2 in one corner of the sample with a diamond tip and contact it with the Al wire using higher power conditions.

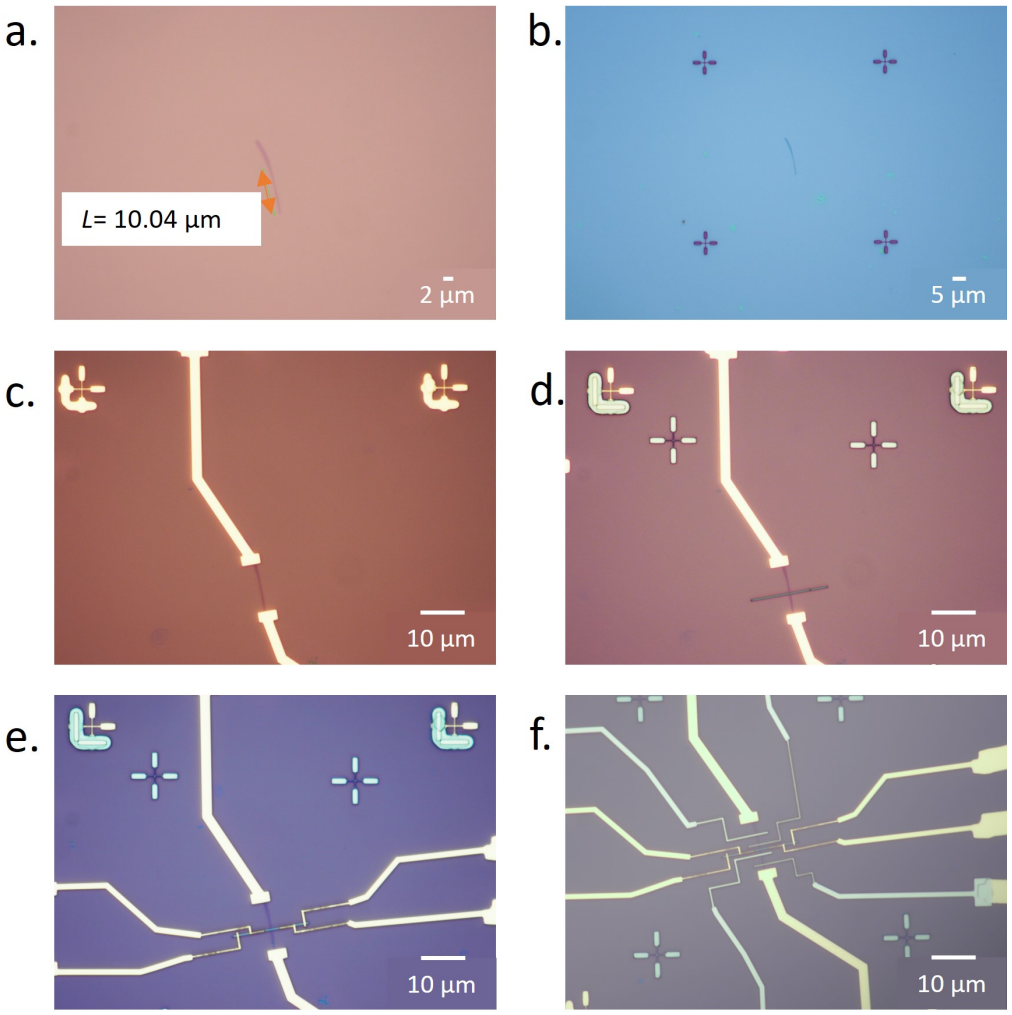

Figure 7.1: LSV fabrication with graphene as spin transport channel. a. HOPG is exfoliated in a clean substrate and the desired flake is selected. **b**. The first lithography step adds markers for the alignment of the flake. **c**. The second lithography step is used for contacting the graphene flake with Ti (5 nm)/Au (45 nm) electrodes. **d**. The third lithography step adds the sputtered BiSe (30 nm thick) wire with a capping layer of SiO_2 (5 nm). **e**. The fourth lithography step adds the metallic contacts to the BiSe wire, by milling the capping layer and again Ti/Au deposition. **f**. The fifth lithography step is performed to pattern the FM electrodes with Ti (3 Å)/Co (35 nm)/Au (5 nm).

7.3 Spin-to-charge conversion signals in graphene LSV

First, it is important to clarify that the SCI signal can have different origins when using graphene-based LSVs devices. In this case, a SOM is combined with a graphene flake, forming a hybrid system at the interface between

both materials which can be interpreted as a proximity effect, in which the SOM imprints its SOC into the graphene. We can thus refer to this system as "proximitized graphene". Therefore, in addition to the SHE of the bulk SOM, the proximitized graphene can show SHE and REE. In order to identify how these different components will appear in the SCI signal, the contributions from each spin polarization when sweeping the magnetic field along one direction (H_x) are analyzed (see Fig. 7.2).

When using a SOM/graphene LSV with a spin-to-charge conversion (SCC) configuration, a magnetic field could be applied to control the direction of the spin polarization $s = (s_x, s_y, s_z)$. In addition, the magnetization of the FM electrode tends to lie along its easy axis, which corresponds to the y direction due to the shape anisotropy. Thus the FM magnetization can be along the $+y$ or $-y$ direction. The nonlocal resistance (R_{NL}) measured when the initial state of the FM is along the $+y$ direction is called $R_{NL}^{\uparrow}$, whereas when the initial state of the FM is along the $-y$ direction it is called $R_{NL}^{\downarrow}$.

When applying H_x, the orientation of the injected spins can be influenced by the precession or by the pulling of the FM. First, when $H_x = 0$, the Co magnetization lies along the easy axis ($s = \pm s_y$). Figure 7.2a shows the schematic representation of the direction of the magnetization along the $+y$-direction ($s = +s_y$). The signal associated with the SCI of $+y$-spin component is maximum at $H_x = 0$, which is represented by the blue solid line ($R_{NL}^{\uparrow}$) in Fig. 7.2b. Similarly, when the initial state of magnetization is opposite ($-y$-direction), the polarization of the injected spins is then $s = -s_y$, this signal is illustrated in Fig. 7.2b by the red dashed line ($R_{NL}^{\downarrow}$).

However, when H_x is finite but small, the direction of the injected spins is perpendicular to the direction of the field, and thus the spins will precess in the graphene channel in the $y-z$ plane (see Fig. 7.2c). As precession begins, the resulting SCI signal from the y-spin component decreases. This is because there are fewer y-spins reaching the SOM wire. For a given positive value of H_x (with $+y$-spin component) the spins reaching the SOM will be polarized along the $+z$-direction ($R_{NL}^{\uparrow}$). On the other hand, for an opposite negative value of H_x, the spins will be polarized along the $-z$-direction. The R_{NL} signal associated with the SCI of s_z spins will also depend on the precession, resulting in an antisymmetric Hanle curve. Figure 7.2d shows the schematic representation of the signal when the initial state of the magnetization is along the $+y$ (blue solid line, $R_{NL}^{\uparrow}$) or $-y$ (red dashed line, $R_{NL}^{\downarrow}$) directions. The two curves are antisymmetric with the magnetic field and have opposite signs for the same value of H_x.

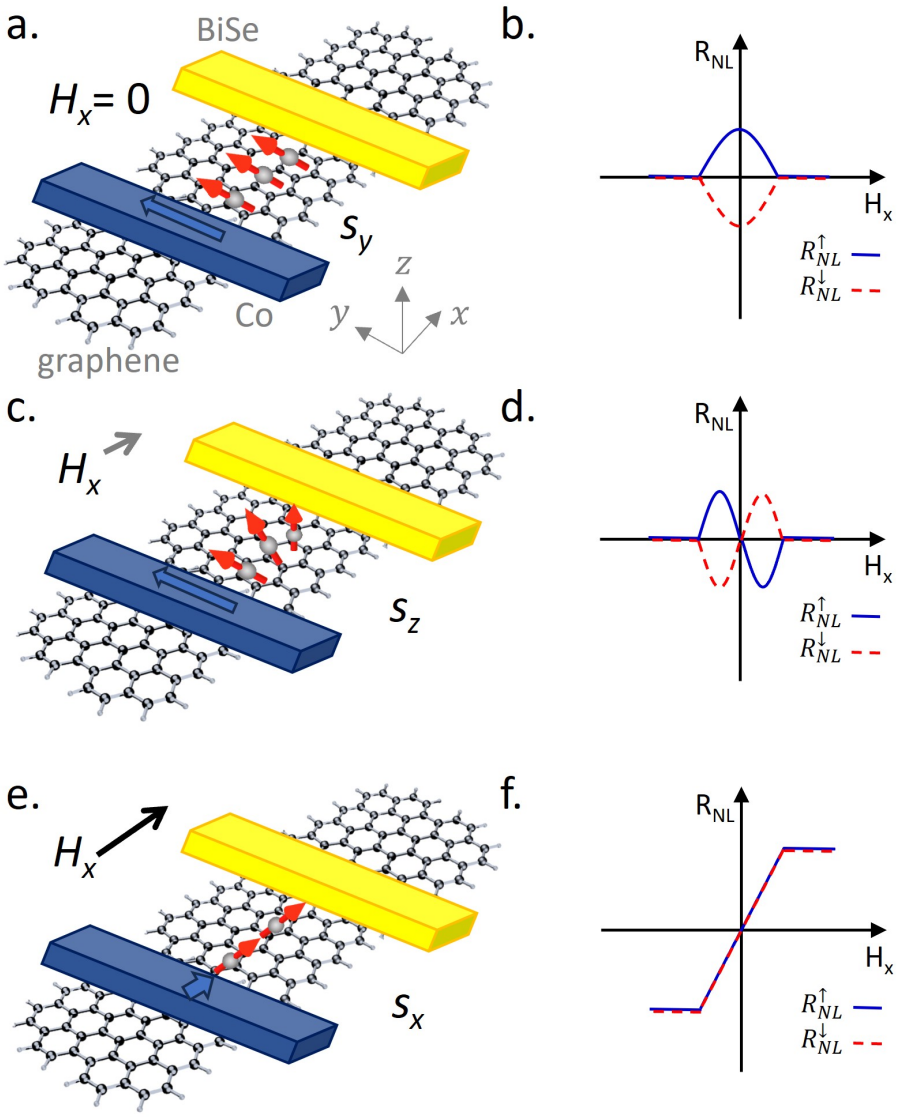

Figure 7.2: Spin components of the spin-to-charge conversion signal with the graphene-based LSV by applying an in-plane magnetic field along the hard axis of the Co electrode. Schematic representation of the **a-b.** y-component, **c-d.** z-component, and **e-f.** x-component of the SCC signal.

For sufficiently large values of H_x, the magnetization of the FM is pulled in the direction of the field until they align. The schematic representation when the FM magnetization is along the $+x$-direction and thus the x-spins are injected is shown

in Fig. 7.2e. The R_{NL} signal associated with the SCI of s_x spins is independent of the initial state of the magnetization because it comes from the pulling of the magnetization, which is why the blue ($R^{\uparrow}_{NL}$) and red ($R^{\downarrow}_{NL}$) curves in Fig. 7.2f are superimposed. These S-shaped curves are antisymmetric with respect to H_x and both have the same sign.

All three contributions (Figs. 7.2b, 7.2d and 7.2f) could be present simultaneously. To separate the different SCC contribution in the R_{NL} vs H_x measurements, we define $R^{Ave}_{SCC} = (R^{\uparrow}_{NL} + R^{\downarrow}_{NL})/2$ and $R_{SCC} = (R^{\uparrow}_{NL} - R^{\downarrow}_{NL})/2$. R^{Ave}_{SCC} corresponds to the SCI of the s_x spins, because the signal is independent of the initial magnetization. R_{SCC} contains the signals from s_y and s_z, because they depend on the initial magnetization. They can be further distinguished by taking the symmetric and antisymmetric parts, respectively [112, 162].

7.4 Charge-to-spin conversion in BiSe/graphene LSV

In general, using LSV devices, both spin-to-charge (SCC) and charge-to-spin (CSC) conversion can be studied, as we did in the previous chapter, leading to reciprocal signals. Both configurations were successfully measured in Chapter 6 due to the channel of Ti/Cu layer deposited at the top of the BiSe wire (see Fig. 6.4). In this chapter, the objective is to remove this shunting channel and leave just the BiSe wire (see Fig. 7.3a). However, the noise when measuring voltage in the BiSe wire was too high because of its high resistivity, hiding any possible nonlocal signal by measuring in the SCC configuration. In contrast, the use of a CSC configuration, where the BiSe wire is used to inject the charge current, greatly improved the signal-to-noise ratio.

To perform such measurement, we apply a constant current $I_c = 20\ \mu$A to the BiSe wire. The charge current (j_c) injected is converted into a spin current (j_s) due to the SHE or a spin density (μ_S) due to the REE, either of which diffuses away in the graphene channel until it reaches the Co electrode, which is detected as a voltage (V_{NL}), as explained in Chapter 2. In our measurements, the direction of j_c (along y-direction) is fixed, whereas the orientation of s is controlled with the external magnetic field as we discussed in the previous section.

We study the CSC by sweeping H_x, and the resulting curves for R_{NL} as a function of H_x at 150 K are shown in Fig. 7.3b. The measurement was performed in four steps: for the first two steps, R_{NL} was measured while sweeping H_x from 0 to 10 kOe and

0 to -10 kOe, with the magnetization of the Co electrode initially saturated in the $+y$-direction prior to each sweep ($R_{NL}^{\uparrow}$, blue curve). Then, similar measurements were repeated for the magnetization of the Co electrode initially set along the $-y$-direction ($R_{NL}^{\downarrow}$, red curve). During the measurement, a gate voltage (V_g) was applied (graphene Dirac point was -17 V). The results shown here correspond to a $V_g = +10$ V, as we obtained the best signal-to-noise ratio.

In order to disentangle the CSC component arising from the different spin polarizations, we follow the protocol discussed in section 7.3 and we calculate R_{CSC}^{Sym} (Fig. 7.3c), R_{CSC}^{Anti} (Fig. 7.3d) and R_{CSC}^{Ave} (Fig. 7.3e).

Initially, the s_x component (R_{CSC}^{Ave}) was the only signal expected coming from the SHE in the BiSe wire. However, we observed two other components (R_{CSC}^{Sym} and R_{CSC}^{Anti}), indicating other CSC contributions in our system. Let us discuss the origin of each one of these components.

The s_x-induced CSC (R_{CSC}^{Ave}) can arise from the SHE in BiSe (with the conventional restriction that j_s, j_c and s must be mutually orthogonal) after is absorbed along z-direction into BiSe. However, the REE in proximitized graphene also gives rise to s_x-spins, making the two contributions indistinguishable. We can compare these results with the ones for SHE in the metallic LSV (Fig. 6.5a). We expect a sign reversal in the s-shaped curve of Fig. 7.3e if the signal is dominated by the SHE of BiSe [because the BiSe wire has opposite stacking order (top/bottom) with respect the spin transport channel, while we keep the electrical configuration]. The absence of this sign reversal between curves in Fig. 6.5a and Fig. 7.3e suggests that the CSC signal originates mostly from the REE in proximitized graphene.

The s_y-induced CSC (R_{CSC}^{Sym}) can only arise from an effect that allows the spin polarization to be parallel to the charge current, since both are along y in this case. As discussed in detail in section 2.2.2, this contribution has been observed in transition metal dichalcogenides (TMD)/graphene van der Waals heterostructures with a certain twist angle, breaking the mirror symmetry in the graphene plane. This allows for an unconventional REE (UREE) in which the spin polarization and the charge current are parallel. Our result is thus unexpected, because it implies that we are also breaking this symmetry, but by depositing a thin film which is polycrystalline, unlike the single crystal TMDs.

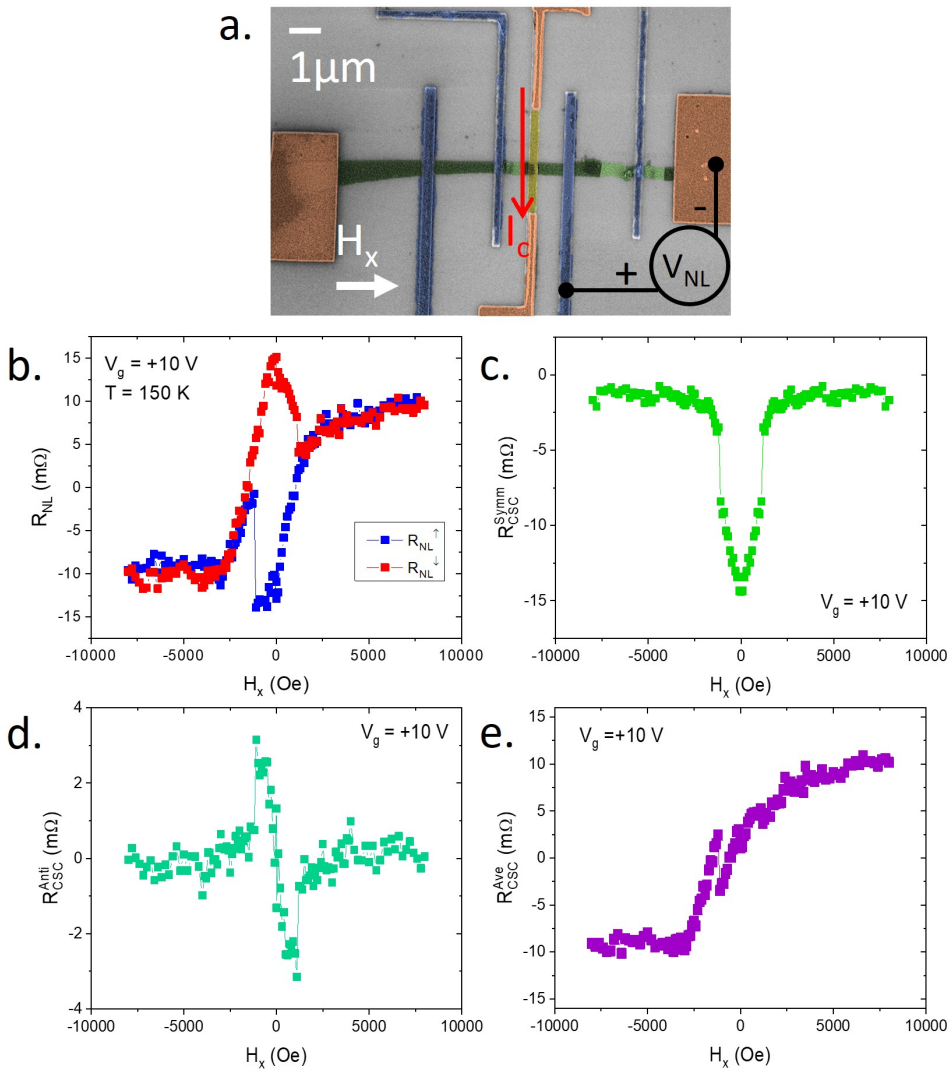

Figure 7.3: Spin-to-charge conversion in BiSe using LSV with graphene by applying H_x. a. Top view false-colored SEM image of the LSV with graphene as spin transport channel (green), BiSe wire (yellow), Ti/Au contacts (orange), and Co electrodes (blue), with the schematic representation of the direct SHE configuration measurements. **b**. Nonlocal resistance as a function of H_x using the configuration shown in panel a, with initial positive ($R^{\uparrow}_{NL}$, blue squares) and negative ($R^{\downarrow}_{NL}$, red squares) magnetization direction of the FM detector measured at 150 K and $V_g = +10$ V. An offset of 4.84 mΩ has been subtracted. **c**. Net symmetric and **d**. antisymmetric Hanle precession signal extracted from the two curves in panel a. by taking $R_{CSC} = R^{\uparrow}_{NL} - R^{\downarrow}_{NL})/2$ and then extracting the symmetric and antisymmetric component. **e.** Average signal extracted from the two curves in panel a. by taking $R^{Ave}_{CSC} = R^{\uparrow}_{NL} + R^{\downarrow}_{NL})/2$.

To further confirm the UREE arising from s_y spins, we measure R_{NL} while sweeping H_y. Due to the shape anisotropy, the easy axis of the Co electrode, and thus its magnetization at zero field, lies along the y direction. By applying a sufficient magnetic field along $\pm y$-direction (H_y), the magnetization of the Co electrode and thus s = (0, $\pm$ s_y,0) of the injected spins can be switched (the coercive field of Co electrodes is typically < 500 Oe). However, H_y does not induce spin precession during spin transport along the graphene channel, because s and H_y are parallel to each other and consequently j_s has one of the two polarization directions ($\pm s_y$). Very interestingly, we observed a square hysteresis loop for R_{NL} as a function of H_y, shown in Fig. 7.4, with the signal switching sign at the coercive field of the Co electrode ($\sim$ 300 Oe). The amplitude of the signal corresponds to the one observed for R_{CSC}^{Sym} in Fig. 7.3c. We also note an opposite sign between the measured V_{NL} corresponding to the CSC from s_x (Fig. 7.3e) and s_y (Figs. 7.3c and 7.4b), indicating that the sign of the conventional and unconventional REEs are opposite.

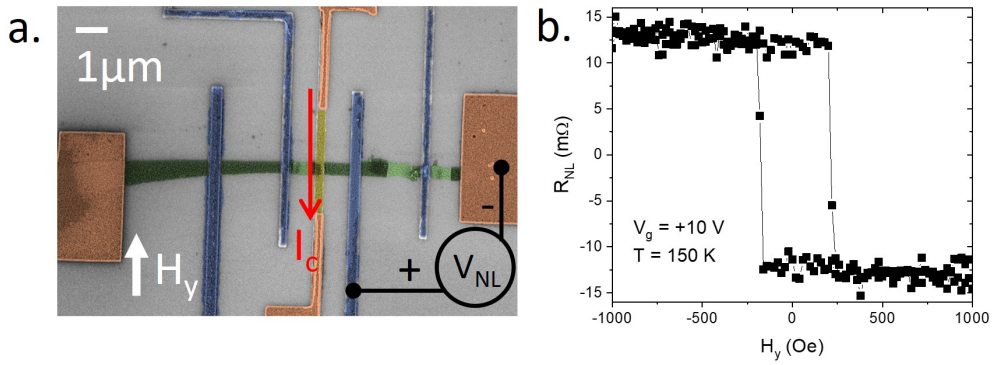

Figure 7.4: Charge-to-spin conversion in BiSe using LSV with graphene by applying H_y. a. Top view false-colored SEM image of the LSV with graphene and BiSe with the schematic representation of the direct SHE configuration measurements with the external magnetic field applied in the easy axis.**b**. Nonlocal resistance as a function of H_y using the configuration shown in panel a, measured at 150 K and $V_g = +10$ V. An offset of 4.7 mΩ has been subtracted.

Finally, the s_z-induced CSC (R_{CSC}^{Anti}) arises from the SHE in the proximitized graphene, also following the orthogonal relation between j_c (injected along y), j_s (diffusing along x) and s (polarized out of plane). The presence of this component is not surprising, since SHE in graphene has been reported with different materials deposited on top, such as Bi_2O_3 [214] or CuO_x [215]. The origin of this SHE could be either intrinsic or extrinsic, as discussed in these works [214, 215].

7.5 Summary and conclusions

We observed an omnidirectional CSC in BiSe/graphene LSV and disentangled each CSC component arising from the different spin polarization directions. The s_x-component can be compared with the one obtained with the metallic LSV in the previous Chapter (Fig. 6.5a), suggesting that the s_x-component in BiSe/graphene LSV is dominated by the REE in proximitized graphene rather than the SHE in bulk BiSe. The s_z-component is also observed and originated from the SHE in the proximitized graphene (orthogonal relation between j_c, j_s and s). The s_y-component observed is possible when mirror symmetries are broken, leading to UREE in proximitized graphene. The UREE had been previously observed only in TMD/graphene van der Waals heterostructures [112, 113, 162] but now we also are capable of detecting it with a sputtered material on graphene, which makes it simpler. Further investigation is needed to quantify the CSC efficiency of BiSe/graphene LSV device, such as the SCI experiments by applying the magnetic field out-of-plane, and the spin transport characterization of the graphene channel (Hanle curves). Although it was completely unexpected in this study, this omnidirectional CSC provides new possibilities in the design of novel spintronic devices, that could use the three spin directions to realize complex operations, and benefit from flexible configurations to generate, detect and control spin currents.

7

Chapter 8

Conclusions and Outlook

This thesis presents a systematic study of sputtered polycrystalline and highly resistive Bi_xSe_{1-x} as a SOM for SCI experiments. This material has been strongly suggested as a candidate to be placed in the readout SO node of Intel's proposed MESO device [11]. In order to quantify its SCI efficiency, it is necessary to properly extract its spin transport parameters such as the spin diffusion length and the spin Hall angle. Towards this objective, we have used different SCI experimental techniques. Here, we summarize the main results of the thesis, as well as future perspectives using these devices towards the implementation of functional spin-based devices.

One of the most established approaches to perform SCI measurements is the spin pumping technique. Chapter 4 presents our first approach to study SCI in sputtered Bi_xSe_{1-x} by spin pumping. We show the results on the frequency dependence of the spin pumping voltage of Py/Bi_xSe_{1-x} and Bi_xSe_{1-x}/Py bilayers and observe that the Gilbert damping of Py is very different in the two stacks. By studying the structural composition by STEM-EDX of both systems, we find a strong interdiffusion, so that the chemical composition of the magnetic layers and the interfaces are not homogeneous and therefore the models used to characterize the properties of the system are no longer valid. Ignoring these inhomogeneities in the interfaces and films would lead to an incorrect estimation of the SCI efficiency.

In Chapter 5, we use a different technique to perform SCI measurements, with an architecture similar to the SO readout node of the MESO device, using a local T-shaped device. Taking advantage of the knowledge gained in Chapter 4, we first study the interfaces when Bi_xSe_{1-x} is sputtered bottom/top on bilayer samples with the FM layer, in this case CoFe. In both stacks, an amorphous layer is found at the interface, which is thicker when Bi_xSe_{1-x} is at the bottom. Such a layer corresponds to interfacial mixing, as confirmed by normalized EDX. We therefore fabricate local T-shaped devices with CoFe at the bottom, so that the interdiffusion is lower. Nevertheless, to improve the signal-to-noise ratio, we have to add a NM (Ti or Pt) layer on top of the Bi_xSe_{1-x} T-shaped electrode. We are able to observe SCI in sputtered Bi_xSe_{1-x} in local spin Hall measurements at room temperature and show that all parameters related to SCI efficiency, namely the resistivity, the spin diffusion length (λ_s) and the spin Hall angle (θ_{SH}), are affected by the intermixing with the top metal contact. In particular, the fact that a change in Se concentration by interdiffusion made a 6-fold difference in Bi_xSe_{1-x} resistivity shows how easily θ_{SH} can be overestimated by a resistivity without considering interdiffusion.

In general, λ_s, which is an essential parameter for proper quantification of SCI efficiency, is unknown for sputtered Bi_xSe_{1-x}. Instead, it is usually taken from a few

reports on epitaxially grown Bi_2Se_3, which has not only a different crystal structure but also a different composition. This dissimilarity inevitably leads to inaccuracies in the subsequent quantification of the SCI efficiency of Bi_xSe_{1-x}. Although we extract a λ_s value in Chapter 5, there were two unknown parameters and only one experiment. To improve the quantification, in Chapter 6 we characterize sputtered Bi_xSe_{1-x} for the first time by the spin absorption technique using lateral spin valves. The use of a nonlocal measurement avoids spurious effects related to local currents and allows us to independently quantify λ_s and θ_{SH} of Bi_xSe_{1-x} in the same device, making this quantification more accurate than previous reports. Despite the uncertainty in the resistivity of the Ti layer separating the Cu spin channel and the sputtered Bi_xSe_{1-x}, the values obtained for the $\theta_{SH}\lambda_s$ product, generally less than 1 nm, are robust. The quantification from the measurements was carefully done with a 3D model, which includes input from TEM characterization of the same devices. We were able to measure and quantify these parameters from 10 K up to 300 K, concluding that the SCI efficiency of this material is not exceptional.

In an effort to suppress this interdiffusion between Bi_xSe_{1-x} and the metal contacts, in Chapter 7 we propose the use of LSV as the characterization technique, but instead of a metallic spin transport channel like Cu, we use a few layers of graphene. Surprisingly, we observe omnidirectional CSC in Bi_xSe_{1-x}/graphene LSV, evidencing that we have CSC components beyond the SHE in bulk Bi_xSe_{1-x} we were looking for. In fact, by comparing with the results in Chapter 6, we conclude that the CSC signal from the s_x-component is dominated by the REE in proximitized graphene rather than the SHE in bulk Bi_xSe_{1-x}. The s_y-component is observed because the mirror symmetries of our Bi_xSe_{1-x}/graphene heterostructure are broken, allowing the UREE in proximitized graphene. Interestingly, s_y follows an unusual non-orthogonal configuration. The s_z-component is also observed, which originates from the SHE in the proximitized graphene (orthogonal relation between j_c, j_s and s). This omnidirectional CSC opens new possibilities for the design of novel spintronic devices that could use the three spin directions to realize complex operations that could benefit from flexible configurations to generate, detect, and control spin currents.

The results presented in this thesis highlight the importance of studying the interfacial and compositional properties of Bi_xSe_{1-x} systems for SCI, since they tend to produce systems with very high interdiffusion and thus the performance is highly dependent on the quality of the layers and interfaces as well as their stoichiometric composition.

However, materials with Bi-based composition are an interesting alternative for SCI and for the development of spin-based devices as MESO logic devices, such as Dirac semimetals, which have gapless electronic excitations protected by topology and symmetry [216]. Their characteristic electronic properties lead to protected surface states and novel responses to applied electric and magnetic fields. Theoretical studies of Dirac semimetals such as Bi and Bi_xSb_{1-x} alloys predicted large SCI efficiencies maximizing at the Dirac point [217–219]. A recent experimental study of the spin-orbit torque based on the Harmonic Hall technique on a series of Bi_xSb_{1-x} alloys grown by sputtering reports a large SCI efficiency arising from the carriers near their Dirac point [220]. In addition, the absence of Se in its chemical composition is also a clear advantage over Bi_xSe_{1-x} for improving the quality of device interfaces.

These Bi-based materials have a high resistivity, a key ingredient to increase the output signals in the readout SO node of the MESO; however, a high resistivity of the SOM will additionally introduce two related problems, such as the conductivity mismatch and the shunting effects with the metallic FM, and these will dramatically reduce the voltage output of the SO node. We propose that the SCI efficiency and voltage output can be studied by introducing a tunneling barrier between the FM and the SOM. Our group has recently investigated the advantage of a tunnel barrier (Supp. Info. in Ref. [34]) in a T-shaped device with β-Ta and CoFe, by introducing an insulating barrier of AlO_x, where an increase in the generated output current and voltage was observed. Nevertheless, an optimization of the barrier layer is required due to the lack of reproducibility. Since tunnel barriers with high spin polarization (P_i) have been well studied in the case of MTJs [20–22, 221], the best candidate material as a tunnel barrier in the SO node is the crystalline (100) MgO in combination with Fe-based alloys (CoFe, CoFeB). The tunnel barrier can prevent mixing, current shunting, and spin backflow while increasing spin injection efficiency.

Bibliography

1. Moore, G. Cramming more components onto integrated circuits. *Electronics* **38,** 114–117 (1965).
2. Rupp, K. *et al.* 50 years of microprocessor trend data. *Microprocessor Trend Data Repository, https://github.com/karlrupp/microprocessor-trend-data/blob/master/50yrs/50-years-processor-trend.png* (2022).
3. Dennard, R. *et al.* Design of ion-implanted MOSFET's with very small physical dimensions. *IEEE Journal of Solid-State Circuits* **9,** 256–268 (1974).
4. Nikonov, D. E. & Young, I. A. Overview of beyond-CMOS devices and a uniform methodology for their benchmarking. *Proceedings of the IEEE* **101,** 2498–2533 (2013).
5. Nikonov, D. E. & Young, I. A. Benchmarking of Beyond-CMOS Exploratory Devices for Logic Integrated Circuits. *IEEE Journal on Exploratory Solid-State Computational Devices and Circuits* **1,** 3–11 (2015).
6. Ferain, I., Colinge, C. A. & Colinge, J.-P. Multigate transistors as the future of classical metal–oxide–semiconductor field-effect transistors. *Nature* **479,** 310–316 (2011).
7. Auth, C. *et al. A 10nm high performance and low-power CMOS technology featuring 3 rd generation FinFET transistors, Self-Aligned Quad Patterning, contact over active gate and cobalt local interconnects* in *2017 IEEE International Electron Devices Meeting (IEDM)* (2017), 29–1.
8. Holt, W. M. 1.1 Moore's law: A path going forward," in 2016 IEEE International Solid-State Circuits Conference (ISSCC). *San Francisco,* 8–13 (2016).
9. Dieny, B. *et al.* Opportunities and challenges for spintronics in the microelectronics industry. *Nature Electronics* **3,** 446–459 (2020).
10. Bhatti, S. *et al.* Spintronics based random access memory: a review. *Materials Today* **20,** 530–548 (2017).

11. Manipatruni, S., Nikonov, D. E. & Young, I. A. Beyond CMOS computing with spin and polarization. *Nature Physics* **14,** 338–343 (2018).

12. Manipatruni, S. *et al.* Scalable energy-efficient magnetoelectric spin–orbit logic. *Nature* **565,** 35–42 (2019).

13. Blundell, S. *Magnetism in condensed matter* (American Association of Physics Teachers, 2003).

14. Binasch, G., Grünberg, P., Saurenbach, F. & Zinn, W. Enhanced magnetoresistance in layered magnetic structures with antiferromagnetic interlayer exchange. *Physical Review B* **39,** 4828–4830 (1989).

15. Baibich, M. N. *et al.* Giant magnetoresistance of (001) Fe/(001) Cr magnetic superlattices. *Physical Review Letters* **61,** 2472–2475 (1988).

16. *Press release. NobelPrize.org. The Discovery of Giant Magnetoresistance* `https://www.nobelprize.org/prizes/physics/2007/press-release/`. 2007. (accessed: 16.03.2023).

17. Marchon, B., Pitchford, T., Hsia, Y.-T., Gangopadhyay, S., *et al.* The head-disk interface roadmap to an areal density of Tbit/in 2. *Advances in Tribology* **2013** (2013).

18. Alexander, M., Thomas, W., Viktor, S. & Siegfried, S. CMOS-compatible spintronic devices: a review. *Semiconductor Science and Technology* **31,** 113006 (2016).

19. Behin-Aein, B., Datta, D., Salahuddin, S. & Datta, S. Proposal for an all-spin logic device with built-in memory. *Nature Nanotechnology* **5,** 266–270 (2010).

20. Julliere, M. Tunneling between ferromagnetic films. *Physics Letters A* **54,** 225–226 (1975).

21. Yuasa, S., Nagahama, T., Fukushima, A., Suzuki, Y. & Ando, K. Giant room-temperature magnetoresistance in single-crystal Fe/MgO/Fe magnetic tunnel junctions. *Nature Materials* **3,** 868–871 (2004).

22. Parkin, S. S. *et al.* Giant tunnelling magnetoresistance at room temperature with MgO (100) tunnel barriers. *Nature Materials* **3,** 862–867 (2004).

23. Ikeda, S. *et al.* Tunnel magnetoresistance of 604% at 300 K by suppression of Ta diffusion in Co Fe B/ Mg O/ Co Fe B pseudo-spin-valves annealed at high temperature. *Applied Physics Letters* **93,** 082508 (2008).

24. Ohno, H., Stiles, M. & Dieny, B. Advancements in spintronics. *Solid State Technology,* hal–02059603f (2017).

25. Engel, B. *et al.* A 4-Mb toggle MRAM based on a novel bit and switching method. *IEEE Transactions on Magnetics* **41,** 132–136 (2005).
26. Slonczewski, J. C. Current-driven excitation of magnetic multilayers. *Journal of Magnetism and Magnetic Materials* **159,** L1–L7 (1996).
27. Berger, L. Emission of spin waves by a magnetic multilayer traversed by a current. *Physical Review B* **54,** 9353–9358 (1996).
28. *STT-MRAM: Introduction and market status* `https://https://www.mram-info.com/stt-mram`. (accessed: 16.03.2023).
29. Sato, N., Xue, F., White, R. M., Bi, C. & Wang, S. X. Two-terminal spin–orbit torque magnetoresistive random access memory. *Nature Electronics* **1,** 508–511 (2018).
30. Manipatruni, S. *et al.* Voltage control of unidirectional anisotropy in ferromagnet-multiferroic system. *Science Advances* **4,** eaat4229 (2018).
31. Heron, J. *et al.* Deterministic switching of ferromagnetism at room temperature using an electric field. *Nature* **516,** 370–373 (2014).
32. Vaz, D. C. *et al.* Voltage-based magnetization switching and reading in magnetoelectric spin-orbit nanodevices. *arXiv preprint arXiv:2302.12162* (2023).
33. Vaz, D. C. *et al. Functional demonstration of a fully integrated magneto-electric spin-orbit device* in *2021 IEEE International Electron Devices Meeting (IEDM)* (2021), 32–4.
34. Pham, V. T. *et al.* Spin–orbit magnetic state readout in scaled ferromagnetic/heavy metal nanostructures. *Nature Electronics* **3,** 309–315 (2020).
35. Wang, Y. *et al.* Room temperature magnetization switching in topological insulator-ferromagnet heterostructures by spin-orbit torques. *Nature Communications* **8,** 1364 (2017).
36. Mellnik, A. *et al.* Spin-transfer torque generated by a topological insulator. *Nature* **511,** 449–451 (2014).
37. Jamali, M. *et al.* Giant spin pumping and inverse spin Hall effect in the presence of surface and bulk spin- orbit coupling of topological insulator Bi_2Se_3. *Nano Letters* **15,** 7126–7132 (2015).
38. Gilbert, M. J. Topological electronics. *Communications Physics* **4,** 70 (2021).
39. Fan, Y. *et al.* Magnetization switching through giant spin–orbit torque in a magnetically doped topological insulator heterostructure. *Nature Materials* **13,** 699–704 (2014).

40. Han, J. *et al.* Room-temperature spin-orbit torque switching induced by a topological insulator. *Physical Review Letters* **119,** 077702 (2017).

41. Khang, N. H. D., Ueda, Y. & Hai, P. N. A conductive topological insulator with large spin Hall effect for ultralow power spin–orbit torque switching. *Nature Materials* **17,** 808–813 (2018).

42. Shao, Q. *et al. Room temperature highly efficient topological insulator/Mo/CoFeB spin-orbit torque memory with perpendicular magnetic anisotropy* in *2018 IEEE International Electron Devices Meeting (IEDM)* (2018), 36.3.1–36.3.4.

43. Khokhriakov, D., Hoque, A. M., Karpiak, B. & Dash, S. P. Gate-tunable spin-galvanic effect in graphene-topological insulator van der Waals heterostructures at room temperature. *Nature Communications* **11,** 3657 (2020).

44. Barua, S. & Rajeev, K. Status of surface conduction in topological insulators. *AIP Advances* **4,** 017135 (2014).

45. Wu, H. *et al.* Room-temperature spin-orbit torque from topological surface states. *Physical Review Letters* **123,** 207205 (2019).

46. Zhang, S. & Fert, A. Conversion between spin and charge currents with topological insulators. *Physical Review B* **94,** 184423 (2016).

47. Li, C. *et al.* Electrical detection of charge-current-induced spin polarization due to spin-momentum locking in Bi_2Se_3. *Nature Nanotechnology* **9,** 218–224 (2014).

48. Moore, J. E. The birth of topological insulators. *Nature* **464,** 194–198 (2010).

49. Dc, M. *et al.* Room-temperature high spin-orbit torque due to quantum confinement in sputtered Bi_xSe_{1-x} films. *Nature Materials* **17,** 800–807 (2018).

50. Dc, M. *et al.* Observation of high spin-to-charge conversion by sputtered bismuth selenide thin films at room temperature. *Nano Letters* **19,** 4836–4844 (2019).

51. Dc, M. *et al.* Room-temperature spin-to-charge conversion in sputtered bismuth selenide thin films via spin pumping from yttrium iron garnet. *Applied Physics Letters* **114,** 102401 (2019).

52. Lu, Q. *et al.* Giant tunable spin Hall angle in sputtered Bi_2Se_3 controlled by an electric field. *Nature Communications* **13,** 1650 (2022).

53. Han, K. H. *et al.* Gate Control of Spin–Orbit Torque in a Sputtered $Bi_2Se_3/Ni_{81}Fe_{19}$ Device. *ACS Applied Electronic Materials* **5,** 2725–2731 (2023).

54. Novoselov, K. S. *et al.* Room-temperature quantum Hall effect in graphene. *Science* **315,** 1379–1379 (2007).

55. Bonell, F. *et al.* Control of spin–orbit torques by interface engineering in topological insulator heterostructures. *Nano Letters* **20,** 5893–5899 (2020).

56. Walsh, L. A. *et al.* Interface chemistry of contact metals and ferromagnets on the topological insulator Bi_2Se_3. *The Journal of Physical Chemistry C* **121,** 23551–23563 (2017).

57. Wang, H. *et al.* Surface-state-dominated spin-charge current conversion in topological-insulator–ferromagnetic-insulator heterostructures. *Physical Review Letters* **117,** 076601 (2016).

58. Deorani, P. *et al.* Observation of inverse spin Hall effect in bismuth selenide. *Physical Review B* **90,** 094403 (2014).

59. Liu, L. *et al.* Spin-polarized tunneling study of spin-momentum locking in topological insulators. *Physical Review B* **91,** 235437 (2015).

60. Maekawa, S., Kikkawa, T., Chudo, H., Ieda, J. & Saitoh, E. Spin and spin current—From fundamentals to recent progress. *Journal of Applied Physics* **133,** 020902 (2023).

61. BALTZ, V. in *The basics of electron transport in spintronics* (EDP Sciences, 2023).

62. Mott, N. F. The electrical conductivity of transition metals. *Proceedings of the Royal Society of London. Series A-Mathematical and Physical Sciences* **153,** 699–717 (1936).

63. Fert, A. & Campbell, I. Two-current conduction in nickel. *Physical Review Letters* **21,** 1190 (1968).

64. Jedema, F., Nijboer, M., Filip, A. & Van Wees, B. Spin injection and spin accumulation in all-metal mesoscopic spin valves. *Physical Review B* **67,** 085319 (2003).

65. Valet, T. & Fert, A. Theory of the perpendicular magnetoresistance in magnetic multilayers. *Physical Review B* **48,** 7099–7113 (1993).

66. Casanova, F., Sharoni, A., Erekhinsky, M. & Schuller, I. K. Control of spin injection by direct current in lateral spin valves. *Physical Review B* **79,** 184415 (2009).

67. Takahashi, S. & Maekawa, S. Spin injection and detection in magnetic nanostructures. *Physical Review B* **67,** 052409 (2003).

68. Idzuchi, H., Fukuma, Y. & Otani, Y. Spin transport in non-magnetic nanostructures induced by non-local spin injection. *Physica E: Low-dimensional Systems and Nanostructures* **68,** 239–263 (2015).

69. Das, K., Dejene, F., Van Wees, B. & Vera-Marun, I. J. Temperature dependence of the effective spin-mixing conductance probed with lateral non-local spin valves. *Applied Physics Letters* **114,** 072405 (2019).

70. Sagasta, E. *et al.* Spin diffusion length of Permalloy using spin absorption in lateral spin valves. *Applied Physics Letters* **111,** 082407 (2017).

71. Isasa, M. *et al.* Spin transport enhancement by controlling the Ag growth in lateral spin valves. *Journal of Physics D: Applied Physics* **48,** 215003 (2015).

72. Sagasta, E. *et al.* Tuning the spin Hall effect of Pt from the moderately dirty to the superclean regime. *Physical Review B* **94,** 060412 (2016).

73. Sagasta, E. *et al.* Unveiling the mechanisms of the spin Hall effect in Ta. *Physical Review B* **98,** 060410 (2018).

74. Laczkowski, P. *et al.* Evaluation of spin diffusion length of AuW alloys using spin absorption experiments in the limit of large spin-orbit interactions. *Physical Review B* **92,** 214405 (2015).

75. Zahnd, G. *et al.* Spin diffusion length and polarization of ferromagnetic metals measured by the spin-absorption technique in lateral spin valves. *Physical Review B* **98,** 174414 (2018).

76. Niimi, Y. *et al.* Extrinsic spin Hall effects measured with lateral spin valve structures. *Physical Review B* **89,** 054401 (2014).

77. Morota, M. *et al.* Indication of intrinsic spin Hall effect in 4 d and 5 d transition metals. *Physical Review B* **83,** 174405 (2011).

78. Hirsch, J. Spin Hall effect. *Physical Review Letters* **83,** 1834–1837 (1999).

79. Edelstein, V. M. Spin polarization of conduction electrons induced by electric current in two-dimensional asymmetric electron systems. *Solid State Communications* **73,** 233–235 (1990).

80. Soumyanarayanan, A., Reyren, N., Fert, A. & Panagopoulos, C. Emergent phenomena induced by spin–orbit coupling at surfaces and interfaces. *Nature* **539,** 509–517 (2016).

81. Manchon, A., Koo, H. C., Nitta, J., Frolov, S. M. & Duine, R. A. New perspectives for Rashba spin–orbit coupling. *Nature Materials* **14,** 871–882 (2015).

82. Dyakonov, M. I. & Perel, V. Current-induced spin orientation of electrons in semiconductors. *Physics Letters A* **35,** 459–460 (1971).

83. D'yakonov, M. & Perel, V. Spin orientation of electrons associated with the interband absorption of light in semiconductors. *Soviet Journal of Experimental and Theoretical Physics* **33,** 1053 (1971).

84. Hall, E. H. XVIII. On the “Rotational Coefficient” in nickel and cobalt. *The London, Edinburgh, and Dublin Philosophical Magazine and Journal of Science* **12,** 157–172 (1881).

85. Kimura, T., Otani, Y., Sato, T., Takahashi, S. & Maekawa, S. Room-temperature reversible spin Hall effect. *Physical Review Letters* **98,** 156601 (2007).

86. Sinova, J., Valenzuela, S. O., Wunderlich, J., Back, C. & Jungwirth, T. Spin Hall effects. *Reviews of Modern Physics* **87,** 1213 (2015).

87. Tian, Y., Ye, L. & Jin, X. Proper scaling of the anomalous Hall effect. *Physical Review Letters* **103,** 087206 (2009).

88. Isasa, M., Villamor, E., Hueso, L. E., Gradhand, M. & Casanova, F. Temperature dependence of spin diffusion length and spin Hall angle in Au and Pt. *Physical Review B* **91,** 024402 (2015).

89. Karplus, R. & Luttinger, J. Hall effect in ferromagnetics. *Physical Review* **95,** 1154–1160 (1954).

90. Jungwirth, T., Niu, Q. & MacDonald, A. Anomalous Hall effect in ferromagnetic semiconductors. *Physical Review Letters* **88,** 207208 (2002).

91. Tanaka, T. *et al.* Intrinsic spin Hall effect and orbital Hall effect in 4 d and 5 d transition metals. *Physical Review B* **77,** 165117 (2008).

92. Smit, J. The spontaneous Hall effect in ferromagnetics II. *Physica* **24,** 39–51 (1958).

93. Zimmermann, B. *et al.* Skew scattering in dilute ferromagnetic alloys. *Physical Review B* **90,** 220403 (2014).

94. Berger, L. Side-jump mechanism for the Hall effect of ferromagnets. *Physical Review B* **2,** 4559–4566 (1970).

95. Bihlmayer, G., Noël, P., Vyalikh, D. V., Chulkov, E. V. & Manchon, A. Rashba-like physics in condensed matter. *Nature Reviews Physics* **4,** 642–659 (2022).

96. Anadón, A. *et al.* Engineering the spin conversion in graphene monolayer epitaxial structures. *APL Materials* **9,** 061113 (2021).

97. Bychkov, Y. A. & Rashba, É. I. Properties of a 2D electron gas with lifted spectral degeneracy. *Journal of Experimental and Theoretical Physics Letters* **39,** 78 (1984).

98. Sánchez, J. R. *et al.* Spin-to-charge conversion using Rashba coupling at the interface between non-magnetic materials. *Nature Communications* **4,** 2944 (2013).

99. Isshiki, H., Muduli, P., Kim, J., Kondou, K. & Otani, Y. Phenomenological model for the direct and inverse Edelstein effects. *Physical Review B* **102,** 184411 (2020).

100. Kondou, K. *et al.* Fermi-level-dependent charge-to-spin current conversion by Dirac surface states of topological insulators. *Nature Physics* **12,** 1027–1031 (2016).

101. Sanz-Fernández, C. *et al.* Quantification of interfacial spin-charge conversion in hybrid devices with a metal/insulator interface. *Applied Physics Letters* **117,** 142405 (2020).

102. Rojas-Sánchez, J.-C. & Fert, A. Compared efficiencies of conversions between charge and spin current by spin-orbit interactions in two- and three- dimensional systems. *Physical Review Applied* **11,** 054049 (2019).

103. Pham, V. T. *et al.* Large spin-charge interconversion induced by interfacial spin-orbit coupling in a highly conducting all-metallic system. *Physical Review B* **104,** 184410 (2021).

104. Isasa, M. *et al.* Origin of inverse Rashba-Edelstein effect detected at the Cu/Bi interface using lateral spin valves. *Physical Review B* **93,** 014420 (2016).

105. Tsai, H. *et al.* Clear variation of spin splitting by changing electron distribution at non-magnetic metal/Bi_2O_3 interfaces. *Scientific Reports* **8,** 5564 (2018).

106. Groen, I. *et al.* Emergence of large spin-charge interconversion at an oxidized Cu/W interface. *Physical Review B* **107,** 184438 (2023).

107. Lesne, E. *et al.* Highly efficient and tunable spin-to-charge conversion through Rashba coupling at oxide interfaces. *Nature Materials* **15,** 1261–1266 (2016).

108. Vaz, D. C. *et al.* Mapping spin–charge conversion to the band structure in a topological oxide two-dimensional electron gas. *Nature Materials* **18,** 1187–1193 (2019).

109. Park, H. *et al.* Enhanced spin-to-charge conversion efficiency in ultrathin Bi_2Se_3 observed by spintronic terahertz spectroscopy. *ACS Applied Materials & Interfaces* **13,** 23153–23160 (2021).

110. Benítez, L. A. *et al.* Tunable room-temperature spin galvanic and spin Hall effects in van der Waals heterostructures. *Nature Materials* **19,** 170–175 (2020).

111. Ghiasi, T. S., Kaverzin, A. A., Blah, P. J. & Van Wees, B. J. Charge-to-spin conversion by the Rashba–Edelstein effect in two-dimensional van der Waals heterostructures up to room temperature. *Nano Letters* **19,** 5959–5966 (2019).

B

112. Ingla-Aynés, J. *et al.* Omnidirectional spin-to-charge conversion in graphene/$NbSe_2$ van der Waals heterostructures. *2D Materials* **9,** 045001 (2022).

113. Ontoso, N. *et al.* Unconventional charge-to-spin conversion in graphene/$MoTe_2$ van der Waals heterostructures. *Physical Review Applied* **19,** 014053 (2023).

114. Safeer, C. *et al.* Large multidirectional spin-to-charge conversion in low- symmetry semimetal $MoTe_2$ at room temperature. *Nano Letters* **19,** 8758–8766 (2019).

115. Camosi, L. *et al.* Resolving spin currents and spin densities generated by charge-spin interconversion in systems with reduced crystal symmetry. *2D Materials* **9,** 035014 (2022).

116. Roy, A., Guimarães, M. H. & Sławińska, J. Unconventional spin Hall effects in nonmagnetic solids. *Physical Review Materials* **6,** 045004 (2022).

117. Seemann, M., Ködderitzsch, D., Wimmer, S. & Ebert, H. Symmetry-imposed shape of linear response tensors. *Physical Review B* **92,** 155138 (2015).

118. Tenzin, K. *et al.* Analogs of Rashba-Edelstein effect from density functional theory. *Physical Review B* **107,** 165140 (2023).

119. Culcer, D. & Winkler, R. Generation of spin currents and spin densities in systems with reduced symmetry. *Physical Review Letters* **99,** 226601 (2007).

120. Lee, S. *et al.* Charge-to-spin conversion in twisted graphene/WSe_2 heterostructures. *Physical Review B* **106,** 165420 (2022).

121. Veneri, A., Perkins, D. T., Péterfalvi, C. G. & Ferreira, A. Twist angle controlled collinear Edelstein effect in van der Waals heterostructures. *Physical Review B* **106,** L081406 (2022).

122. Niimi, Y. *et al.* Giant spin Hall effect induced by skew scattering from bismuth impurities inside thin film CuBi alloys. *Physical Review Letters* **109,** 156602 (2012).

123. Pham, V. T. *et al.* Ferromagnetic/nonmagnetic nanostructures for the electrical measurement of the spin Hall effect. *Nano Letters* **16,** 6755–6760 (2016).

124. Torres, W. S. *et al.* Calculation method of spin accumulations and spin signals in nanostructures using spin resistors. *The European Physical Journal B* **91,** 37 (2018).

125. Schmidt, G., Ferrand, D., Molenkamp, L., Filip, A. & Van Wees, B. Fundamental obstacle for electrical spin injection from a ferromagnetic metal into a diffusive semiconductor. *Physical Review B* **62,** R4790 (2000).

126. Rashba, E. Theory of electrical spin injection: Tunnel contacts as a solution of the conductivity mismatch problem. *Physical Review B* **62,** R16267 (2000).

127. Groen, I. *et al.* Disentangling spin, anomalous, and planar Hall effects in ferromagnet–heavy-metal nanostructures. *Physical Review Applied* **15,** 044010 (2021).

128. Mizukami, S., Ando, Y. & Miyazaki, T. Ferromagnetic resonance linewidth for NM/80NiFe/NM films (NM= Cu, Ta, Pd and Pt). *Journal of Magnetism and Magnetic Materials* **226,** 1640–1642 (2001).

129. Mizukami, S., Ando, Y. & Miyazaki, T. Effect of spin diffusion on Gilbert damping for a very thin permalloy layer in Cu/permalloy/Cu/Pt films. *Physical Review B* **66,** 104413 (2002).

130. Urban, R., Woltersdorf, G. & Heinrich, B. Gilbert damping in single and multilayer ultrathin films: Role of interfaces in nonlocal spin dynamics. *Physical Review Letters* **87,** 217204 (2001).

131. Tserkovnyak, Y., Brataas, A. & Bauer, G. E. Spin pumping and magnetization dynamics in metallic multilayers. *Physical Review B* **66,** 224403 (2002).

132. Rojas-Sánchez, J.-C. *et al.* Spin pumping and inverse spin Hall effect in platinum: the essential role of spin-memory loss at metallic interfaces. *Physical Review Letters* **112,** 106602 (2014).

133. Rojas-Sánchez, J.-C. *et al.* Spin to charge conversion at room temperature by spin pumping into a new type of topological insulator: α-Sn films. *Physical Review Letters* **116,** 096602 (2016).

134. Rojas-Sánchez, J.-C. *et al.* Spin pumping and inverse spin Hall effect in germanium. *Physical Review B* **88,** 064403 (2013).

135. Gilbert, T. L. A phenomenological theory of damping in ferromagnetic materials. *IEEE Transactions on Magnetics* **40,** 3443–3449 (2004).

136. Saitoh, E., Ueda, M., Miyajima, H. & Tatara, G. Conversion of spin current into charge current at room temperature: Inverse spin-Hall effect. *Applied Physics Letters* **88** (2006).

137. Azevedo, A., Vilela-Leão, L., Rodríguez-Suárez, R., Santos, A. L. & Rezende, S. Spin pumping and anisotropic magnetoresistance voltages in magnetic bilayers: Theory and experiment. *Physical Review B* **83,** 144402 (2011).

138. Kajiwara, Y. *et al.* Transmission of electrical signals by spin-wave interconversion in a magnetic insulator. *Nature* **464,** 262–266 (2010).

139. Vlietstra, N. *et al.* Exchange magnetic field torques in YIG/Pt bilayers observed by the spin-Hall magnetoresistance. *Applied Physics Letters* **103,** 032401 (2013).

140. Sun, Y. *et al.* Damping in yttrium iron garnet nanoscale films capped by platinum. *Physical Review Letters* **111,** 106601 (2013).

141. Huang, S.-Y. *et al.* Transport magnetic proximity effects in platinum. *Physical Review Letters* **109,** 107204 (2012).

142. Murakami, S., Nagaosa, N. & Zhang, S.-C. Dissipationless quantum spin current at room temperature. *Science* **301,** 1348–1351 (2003).

143. Kato, Y. K., Myers, R. C., Gossard, A. C. & Awschalom, D. D. Observation of the spin Hall effect in semiconductors. *Science* **306,** 1910–1913 (2004).

144. Riego, P. *et al.* Absence of detectable current-induced magneto-optical Kerr effects in Pt, Ta, and W. *Applied Physics Letters* **109,** 172402 (2016).

145. Stamm, C. *et al.* Magneto-optical detection of the spin Hall effect in Pt and W thin films. *Physical Review Letters* **119,** 087203 (2017).

146. Tulapurkar, A. *et al.* Spin-torque diode effect in magnetic tunnel junctions. *Nature* **438,** 339–342 (2005).

147. Liu, L., Moriyama, T., Ralph, D. & Buhrman, R. Spin-torque ferromagnetic resonance induced by the spin Hall effect. *Physical Review Letters* **106,** 036601 (2011).

148. Pi, U. H. *et al.* Tilting of the spin orientation induced by Rashba effect in ferromagnetic metal layer. *Applied Physics Letters* **97,** 162507 (2010).

149. Tatara, G. & Kohno, H. Theory of current-driven domain wall motion: Spin transfer versus momentum transfer. *Physical Review Letters* **92,** 086601 (2004).

150. Garello, K. *et al.* Symmetry and magnitude of spin–orbit torques in ferromagnetic heterostructures. *Nature Nanotechnology* **8,** 587–593 (2013).

151. Yun, S. J., Park, E.-S., Lee, K.-J. & Lim, S. H. Accurate analysis of harmonic Hall voltage measurement for spin–orbit torques. *NPG Asia Materials* **9,** e449–e449 (2017).

152. Yasuda, K. *et al.* Current-nonlinear Hall effect and spin-orbit torque magnetization switching in a magnetic topological insulator. *Physical Review Letters* **119,** 137204 (2017).

153. Kim, J. *et al.* Layer thickness dependence of the current-induced effective field vector in Ta| CoFeB| MgO. *Nature Materials* **12,** 240–245 (2013).

154. Norrman, K., Ghanbari-Siahkali, A. & Larsen, N. 6 Studies of spin-coated polymer films. *Annual Reports Section" C"(Physical Chemistry)* **101,** 174–201 (2005).

155. Jun, S.-I., Rack, P. D., McKnight, T. E., Melechko, A. V. & Simpson, M. L. Direct-current substrate bias effects on amorphous silicon sputter-deposited films for thin film transistor fabrication. *Applied Physics Letters* **87,** 132108 (2005).

156. Zhang, J. X. & Hoshino, K. *Molecular sensors and nanodevices: principles, designs and applications in biomedical engineering* (Academic Press, 2018).

157. Swann, S. Magnetron sputtering. *Physics in technology* **19,** 67 (1988).

158. Wang, Z. & Zhang, Z. in *Advanced Nano Deposition Methods* 33–58 (John Wiley & Sons, Ltd, 2016). ISBN: 9783527696406. https://onlinelibrary.wiley.com/doi/abs/10.1002/9783527696406.ch2.

159. Rossnagel, S. Thin film deposition with physical vapor deposition and related technologies. *Journal of Vacuum Science & Technology A: Vacuum, Surfaces, and Films* **21,** S74–S87 (2003).

160. Yan, W. *et al.* Large room temperature spin-to-charge conversion signals in a few-layer graphene/Pt lateral heterostructure. *Nature Communications* **8,** 661 (2017).

161. Safeer, C. *et al.* Room-temperature spin Hall effect in graphene/MoS_2 van der Waals heterostructures. *Nano Letters* **19,** 1074–1082 (2019).

162. Safeer, C. *et al.* Reliability of spin-to-charge conversion measurements in graphene-based lateral spin valves. *2D Materials* **9,** 015024 (2021).

163. *Nitto. Surface Protection Tape with unique deformation behaviour SPV 224PR-MJ* https://www.nitto.com/eu/en/products/surface/spv_metal017/. (accessed: 13.04.2023).

164. Yi, M. & Shen, Z. A review on mechanical exfoliation for the scalable production of graphene. *Journal of Materials Chemistry A* **3,** 11700–11715 (2015).

165. Novoselov, K. S. *et al.* Two-dimensional atomic crystals. *Proceedings of the National Academy of Sciences* **102,** 10451–10453 (2005).

166. *Instruments, K. Model 2182 and 2182A Nanovoltmeter. Users Manual. Keithley Instruments.* https://download.tek.com/manual/2182A-900-01_May_2017.pdf.. (accessed: 17.04.2023).

167. Daire, A., Goeke, W. & Tupta, M. A. *New instruments can lock out lock-ins, Keithley Instruments, Inc.* http://www.tek.com/sites/tek.com/files/media/document/resources/Lock-In%20WP.pdf. 2005.

B

168. Vernon-Parry, K. D. Scanning electron microscopy: an introduction. *III-Vs Review* **13,** 40–44 (2000).

169. Kohl, H. & Reimer, L. Transmission Electron Microscopy. *Springer Series in Optical Sciences* **36** (2008).

170. Nellist, P. D. in *Science of microscopy* 65–132 (Springer, 2007).

171. Bassim, N., Scott, K. & Giannuzzi, L. A. Recent advances in focused ion beam technology and applications. *MRS Bulletin* **39,** 317–325 (2014).

172. Melngailis, J. Focused ion beam technology and applications. *Journal of Vacuum Science & Technology B: Microelectronics Processing and Phenomena* **5,** 469–495 (1987).

173. Rugar, D. & Hansma, P. Atomic force microscopy. *Physics Today* **43,** 23–30 (1990).

174. Elton, L. & Jackson, D. F. X-ray diffraction and the Bragg law. *American Journal of Physics* **34,** 1036–1038 (1966).

175. Chason, E. & Mayer, T. Thin film and surface characterization by specular X-ray reflectivity. *Critical Reviews in Solid State and Material Sciences* **22,** 1–67 (1997).

176. Geuzaine, C. & Remacle, J.-F. Gmsh: A 3-D finite element mesh generator with built-in pre-and post-processing facilities. *International journal for numerical methods in engineering* **79,** 1309–1331 (2009).

177. Dular, P. & Geuzaine, C. *GetDP reference manual: the documentation for GetDP, a general environment for the treatment of discrete problems* `http://getdp.info`.

178. Dular, P., Geuzaine, C., Henrotte, F. & Legros, W. A general environment for the treatment of discrete problems and its application to the finite element method. *IEEE Transactions on Magnetics* **34,** 3395–3398 (1998).

179. Dular, P., Geuzaine, C., Genon, A. & Legros, W. An evolutive software environment for teaching finite element methods in electromagnetism. *IEEE Transactions on Magnetics* **35,** 1682–1685 (1999).

180. Geuzaine, C., Dular, P. & Legros, W. *A General Environment for the Treatment of Discrete Problems and its Application to Coupled Finite Element and Boundary Integral Methods* in *Proceedings of the 8th International IGTE Symposium on Numerical Field Calculation in Electrical Engineering* (Graz (Austria), 1998).

181. Geuzaine, C. *GetDP: a general finite-element solver for the de Rham complex* in *PAMM Volume 7 Issue 1. Special Issue: Sixth International Congress on Industrial Applied Mathematics (ICIAM07) and GAMM Annual Meeting, Zürich 2007* **7** (Wiley, 2008), 1010603–1010604.

182. Manchon, A. *et al.* Current-induced spin-orbit torques in ferromagnetic and antiferromagnetic systems. *Reviews of Modern Physics* **91,** 035004 (2019).

183. Shao, Q. *et al.* Roadmap of spin–orbit torques. *IEEE Transactions on Magnetics* **57,** 1–39 (2021).

184. Fanchiang, Y. *et al.* Strongly exchange-coupled and surface-state-modulated magnetization dynamics in Bi_2Se_3/yttrium iron garnet heterostructures. *Nature Communications* **9,** 223 (2018).

185. Zhang, J., Velev, J. P., Dang, X. & Tsymbal, E. Y. Band structure and spin texture of Bi_2Se_3 3 d ferromagnetic metal interface. *Physical Review B* **94,** 014435 (2016).

186. Mendes, J. *et al.* Unveiling the spin-to-charge current conversion signal in the topological insulator Bi_2Se_3 by means of spin pumping experiments. *Physical Review Materials* **5,** 024206 (2021).

187. Martin-Rio, S., Frontera, C., Pomar, A., Balcells, L. & Martinez, B. Suppression of spin rectification effects in spin pumping experiments. *Scientific Reports* **12,** 224 (2022).

188. Tserkovnyak, Y., Brataas, A. & Bauer, G. E. Enhanced Gilbert damping in thin ferromagnetic films. *Physical Review Letters* **88,** 117601 (2002).

189. Tserkovnyak, Y., Brataas, A., Bauer, G. E. & Halperin, B. I. Nonlocal magnetization dynamics in ferromagnetic heterostructures. *Reviews of Modern Physics* **77,** 1375 (2005).

190. Iguchi, R. & Saitoh, E. Measurement of spin pumping voltage separated from extrinsic microwave effects. *Journal of the Physical Society of Japan* **86,** 011003 (2017).

191. Kuhlmann, N., Vogel, A. & Meier, G. Magnetization dynamics and cone angle precession in permalloy rectangles. *Physical Review B* **85,** 014410 (2012).

192. Ounadjela, K., Lefakis, H., Speriosu, V., Hwang, C. & Alexopoulos, P. Thickness dependence of magnetization and magnetostriction of NiFe and NiFeRh films. *Le Journal de Physique Colloques* **49,** C8–1709 (1988).

193. He, H. *et al.* Enhancement of spin-to-charge conversion efficiency in topological insulators by interface engineering. *APL Materials* **9,** 071104 (2021).

194. Zhang, W., Han, W., Jiang, X., Yang, S.-H. & SP Parkin, S. Role of transparency of platinum–ferromagnet interfaces in determining the intrinsic magnitude of the spin Hall effect. *Nature Physics* **11,** 496–502 (2015).

195. Cosset-Chéneau, M. *et al.* Evidence of interfacial asymmetric spin scattering at ferromagnet-Pt interfaces. *Physical Review B* **103,** L201403 (2021).

196. Kittel, C., McEuen, P. & McEuen, P. *Introduction to solid state physics* (Wiley New York, 1996).

197. Shaw, J. M., Nembach, H. T., Silva, T. J. & Boone, C. T. Precise determination of the spectroscopic g-factor by use of broadband ferromagnetic resonance spectroscopy. *Journal of Applied Physics* **114,** 243906 (2013).

198. Ferfolja, K., Valant, M., Mikulska, I., Gardonio, S. & Fanetti, M. Chemical instability of an interface between silver and Bi_2Se_3 topological insulator at room temperature. *The Journal of Physical Chemistry C* **122,** 9980–9984 (2018).

199. Ferfolja, K. *et al.* A cryogenic solid-state reaction at the interface between Ti and the Bi_2Se_3 topological insulator. *Journal of Materials Chemistry C* **8,** 11492–11498 (2020).

200. Li, H., Lin, C.-C., Nikonov, D. E. & Young, I. A. Differential electrically insulated magnetoelectric spin-orbit logic circuits. *IEEE Journal on Exploratory Solid-State Computational Devices and Circuits* **7,** 18–25 (2021).

201. Du, C., Wang, H., Yang, F. & Hammel, P. C. Systematic variation of spin-orbit coupling with d-orbital filling: Large inverse spin Hall effect in 3 d transition metals. *Physical Review B* **90,** 140407 (2014).

202. Wang, H. *et al.* Scaling of spin Hall angle in 3d, 4d, and 5d metals from $Y_3Fe_5O_{12}$/metal spin pumping. *Physical Review Letters* **112,** 197201 (2014).

203. Pham, V. *et al.* Electrical detection of magnetic domain walls by inverse and direct spin Hall effect. *Applied Physics Letters* **109,** 192401 (2016).

204. Linder, J., Yokoyama, T. & Sudbø, A. Anomalous finite size effects on surface states in the topological insulator Bi_2Se_3. *Physical Review B* **80,** 205401 (2009).

205. Dankert, A., Geurs, J., Kamalakar, M. V., Charpentier, S. & Dash, S. P. Room temperature electrical detection of spin polarized currents in topological insulators. *Nano Letters* **15,** 7976–7981 (2015).

206. Dankert, A. *et al.* Origin and evolution of surface spin current in topological insulators. *Physical Review B* **97,** 125414 (2018).

207. Ramaswamy, R. *et al.* Spin orbit torque driven magnetization switching with sputtered Bi_2Se_3 spin current source. *Journal of Physics D: Applied Physics* **52,** 224001 (2019).

208. Zhang, X. *et al.* Topological Surface States-Induced Perpendicular Magnetization Switching in Pt/Co/Bi2Se3 Heterostructures. *Physica Status Solidi (RRL)–Rapid Research Letters* **14,** 2000033 (2020).

209. Villamor, E., Isasa, M., Hueso, L. E. & Casanova, F. Contribution of defects to the spin relaxation in copper nanowires. *Physical Review B* **87,** 094417 (2013).

210. Bakker, F., Slachter, A., Adam, J.-P. & Van Wees, B. Interplay of Peltier and Seebeck effects in nanoscale nonlocal spin valves. *Physical Review Letters* **105,** 136601 (2010).

211. Isshiki, H. *et al.* Determination of spin Hall angle in the Weyl ferromagnet Co_2MnGa by taking into account the thermoelectric contributions. *Physical Review Materials* **6,** 084411 (2022).

212. Jacquod, P., Whitney, R. S., Meair, J. & Büttiker, M. Onsager relations in coupled electric, thermoelectric, and spin transport: The tenfold way. *Physical Review B* **86,** 155118 (2012).

213. Spataru, C. D. & Léonard, F. Fermi-level pinning, charge transfer, and relaxation of spin-momentum locking at metal contacts to topological insulators. *Physical Review B* **90,** 085115 (2014).

214. Safeer, C. *et al.* Spin Hall effect in bilayer graphene combined with an insulator up to room temperature. *Nano Letters* **20,** 4573–4579 (2020).

215. Yang, H. *et al.* Gate-tunable spin Hall effect in an all-light-element heterostructure: graphene with copper oxide. *Nano Letters* **23,** 4406–4414 (2023).

216. Armitage, N., Mele, E. & Vishwanath, A. Weyl and Dirac semimetals in three-dimensional solids. *Reviews of Modern Physics* **90,** 015001 (2018).

217. Şahin, C. & Flatté, M. E. Tunable giant spin Hall conductivities in a strong spin-orbit semimetal: Bi 1- x Sb x. *Physical Review Letters* **114,** 107201 (2015).

218. Fukazawa, T., Kohno, H. & Fujimoto, J. Intrinsic and extrinsic spin Hall effects of Dirac electrons. *Journal of the Physical Society of Japan* **86,** 094704 (2017).

219. Fuseya, Y., Ogata, M. & Fukuyama, H. Spin-Hall effect and diamagnetism of Dirac electrons. *Journal of the Physical Society of Japan* **81,** 093704 (2012).

220. Chi, Z. *et al.* The spin Hall effect of Bi-Sb alloys driven by thermally excited Dirac-like electrons. *Science Advances* **6,** eaay2324 (2020).

B

221. Almasi, H. *et al.* Enhanced tunneling magnetoresistance and perpendicular magnetic anisotropy in Mo/CoFeB/MgO magnetic tunnel junctions. *Applied Physics Letters* **106,** 182406 (2015).

G

Glossary

1D	one-dimensional
2D	two-dimensional
2DEG	two-dimensional electron gas
3D	three-dimensional
AC	alternating current
AFM	Atomic force microscopy
AHE	anomalous Hall effect
ALU	arithmetic logic unit
AMR	anisotropic magnetoresistance
BiSe	Bi_xSe_{1-x}
CMOS	complementary metal-oxide-semiconductor
CPW	coplanar waveguide
CSC	charge-to-spin conversion
DC	direct current
DOS	density of states
eBL	electron-beam lithography
EDX	energy-dispersive X-ray
FEM	Finite element method
FM	ferromagnetic
FMR	ferromagnetic resonance
GMR	giant magnetoresistance
HOPG	highly-oriented pyrolytic graphite
IREE	inverse Rashba-Edelstein effect
ISHE	inverse spin Hall effect
LSV	lateral spin valve
ME	magneto-electric
MESO	magneto-electric spin-orbit
MRAM	magnetoresistive random access memory

MTJ	magnetic tunnel junction
NM	non-magnetic
OHE	ordinary Hall effect
PHE	planar Hall effect
PMMA	Polymethyl Methacrylate
PPMS	physical property measurement system
PVD	physical vapor deposition
REE	Rashba-Edelstein effect
RF	radio frequency
SCC	spin-to-charge conversion
SCI	spin-charge interconversion
SEM	Scanning electron microscopy
SHE	spin Hall effect
SO	spin-orbit
SOC	spin-orbit coupling
SOM	spin-orbit coupling material
SOT	spin-orbit torque
SP	spin-pumping
STEM	scanning transmission electron microscopy
STT	spin-transfer torque
TEM	Transmission electron microscopy
TI	topological insulator
TMD	transition metal dichalcogenides
TMR	tunneling magnetoresistance
UHV	ultra high vacuum
UREE	unconventional REE
VSM	vibrating sample magnetometry
ZEP	α-chloromethacrylate and α-methylstyrene

List of Publications

This thesis is based on the following publications:

Spin-to-charge conversion by spin pumping in sputtered polycrystalline Bi_xSe_{1-x}.
Isabel C Arango*, Alberto Anadón*, Silvestre Novoa, Van Tuong Pham, Won Young Choi, Junior Alegre, Laurent Badie, Andrey Chuvilin, Sébastien Petit-Watelot, Luis E Hueso, Fèlix Casanova, & Juan-Carlos Rojas-Sánchez.
Physical Review Materials, **7**(7), 075402 (2023). / Chapter 4.

All-electrical spin-to-charge conversion in sputtered Bi_xSe_{1-x}.
Won Young Choi*, **Isabel C Arango***, Van Tuong Pham, Diogo C. Vaz, Haozhe Yang, Inge Groen, Chia-Ching Lin, Emily S. Kabir, Kaan Oguz, Punyashloka Debashis, John J. Plombon, Hai Li, Dmitri E. Nikonov, Andrey Chuvilin, Luis E. Hueso, Ian A. Young, & Fèlix Casanova.
Nano Letters **22**(19), 7992-7999 (2022) / Chapter 5.

Quantification of spin-charge interconversion in highly resistive sputtered Bi_xSe_{1-x} with non-local spin valves.
Isabel C Arango*, Won Young Choi*, Van Tuong Pham, Inge Groen, Diogo C. Vaz, Punyashloka Debashis, Hai Li, Mahendra DC, Kaan Oguz, Andrey Chuvilin, Luis E. Hueso, Ian A. Young, & Fèlix Casanova.
Physical Review B, **108**, 104425 (2023) / Chapter 6.

* equal contribution

Other publications:

Voltage-based magnetization switching and reading in magnetoelectric spin-orbit nanodevices.
Diogo C. Vaz*, Chia-Ching Lin*, John Plombon, Won Young Choi, Inge Groen, **Isabel C Arango**, Andrey Chuvilin, Luis E. Hueso, Dmitri E. Nikonov, Hai Li, Punyashloka Debashis, Scott Clendenning, Tanay A. Gosavi, Yen-Lin Huang, Bhagwati Prasad, Ramamoorthy Ramesh, Aymeric Vecchiola, Manuel Bibes, Karim Bouzehouane, Stephane Fusil, Vincent Garcia, Ian A. Young, & Fèlix Casanova.
arXiv preprint arXiv:2302.12162 (2023).

Emergence of large spin-charge interconversion at an oxidized Cu/W interface.
Inge Groen, Van Tuong Pham, Stefan Ilic, Andrey Chuvilin, Won Young Choi, Edurne Sagasta, Diogo C. Vaz, **Isabel Arango**, Nerea Ontoso, F. Sebastian Bergeret, Luis E. Hueso, Ilya V. Tokatly, & Fèlix Casanova.
Physical Review B, **107**(18), 184438 (2023).

Demonstration of a magneto-electric spin-orbit device.
Diogo C. Vaz*, Chia-Ching Lin*, John Plombon, Won Young Choi, Inge Groen, **Isabel Arango**, Van Tuong Pham, Dmitri E. Nikonov, Hai Li, Punyashloka Debashis, Scott Clendenning, Tanay A. Gosavi, Vincent Garcia, Stephane Fusil, Manuel Bibes, Yen-Lin Huang, Bhagwati Prasad, Ramamoorthy Ramesh, Felix Casanova & Ian A. Young.
2021 IEEE International Electron Devices Meeting (IEDM), accepted (2021).

Acknowledgements

Finally, after all these years, I would first like to thank my supervisors Fèlix and Luis for giving me the opportunity to join the Nanodevices group. They put a lot of trust in me. In particular, I would like to thank Fèlix for all his patience, dedication, and time spent discussing the physics and challenges behind the "promising" BiSe, for always taking the time to discuss any problem, and for the attention he paid to every single detail in this study, which really makes the difference in a scientific research.

This thesis was done in collaboration with Intel and I would like to thank all the Intel team that worked with us under the FEINMAN project led by Ian Young for the development of the MESO device. Thanks for all the discussions to give us a different perspective and for the device fabrication advice.

Thanks to Juan-Carlos Rojas-Sánchez and Alberto Anadón from the Institut Jean Lamour, Université de Lorraine CNRS in France, for their collaboration and discussions on the spin pumping experiments. Also, many thanks to Andrey Chuvilin and Christopher Tollan for the transmission electron microscope images and EDX analysis, which showed us that the devices are not always as we expected, and making us understand what really happens in our devices and their interfaces.

I would especially want to thank Inge. Moving to Spain was a big step for me and she made my first months at nanoGUNE easier and taught me pretty much everything I know now about experimental techniques and measurements in the cleanroom and the labs. Also, many thanks to Tuong for the discussions that helped me understand the physics behind our devices and taught me how to run the simulations done in this thesis. Also thanks to Won Young and Diogo who were part of the "Intel group" (from nanoGUNE) together with Inge and Tuong, it was a great pleasure to work with you. Thank you very much for your help and the many discussions we had that pushed me to continue and keep trying.

Sincere thanks to Roger, Cesar, and Ralph for all the technical assistance, support, training, and knowledge sharing for the cleanroom and lab procedures and equipment operations. For all your patience every time I called asking for your help and the efforts you made to keep all the equipment and labs running.

I would like to thank Safeer, Nerea, Pep, Haozhe, and Zhendong for sharing their knowledge about graphene, for the nice discussions, and for teaching me how to exfoliate and fabricate graphene devices. To all the current and former members of the Nanodevices group. A mis parceros María and José, for listening to me, supporting me, and making me laugh. To Eoin, Witold, Eli, Jone, Manu, Bea, Julien... I wanted to list you all, but we are a big group now! Thank you all for the coffees, lunches, burgers, beers, the amazing exchange of cultures, for the moments we shared, and for the nice atmosphere in the group. And more in general, to all the nanopeople, the nice community of nanoGUNE.

When you move more than 8492 km away from your hometown and by chance you find more people from the same country, with whom you can share some tasty empanaditas, ajiaco, arepitas, bandeja paisa, laugh, dance salsa, or just listen to each other, it is really great, actually, I would rather say *chévere*, and for that I would like to thank my Colombian friends: Laura, Mario, Wilmer, and Meli. Also, many thanks to my ex-flatmate Cris, who shared dinners (*cereales*) with me at home after work, listened to me all the failed experiments and survived the quarantine together by baking cakes and cookies.

Xabi, gracias por ser mi gran apoyo, por las risas interminables, por todos los bonitos momentos a tu lado y por todos los que nos quedan por vivir!

Y por supuesto al motor de mi vida: Carlos, Esperanza, Eduardo y Vale, mi familia! Gracias por siempre creer en mí, por ser mi motivación, y hacerme sentir que sin importar la distancia que nos separe están conmigo siempre.

Thanks for all the support I have received over these years. To help me grow professionally and become a more open-minded and aware person.

Muchas gracias y Eskerrik asko!

Donostia, 2023,

Isa